STUDYING THE QUARK STRUCTURE OF THE PROTON IN HIGH ENERGY PROTON-PROTON COLLISIONS AT RHIC

BY

RUIZHE YANG

DISSERTATION

Submitted in partial fulfillment of the requirements
for the degree of Doctor of Philosophy in Physics
in the Graduate College of the
University of Illinois at Urbana-Champaign, 2010

Urbana, Illinois

Doctoral Committee:

Professor Jen-Chieh Peng, Chair
Associate Professor Matthias Grosse-Perdekamp, Director of Research
Professor John Stack
Professor Scott Willenbrock

Abstract

This thesis presents the first measurement of single spin asymmetries from inclusive di-hadron production in polarized proton-proton collisions at Relativistic Heavy Ion Collider. This measurement combines the transversity distribution function and a polarized di-hadron fragmentation function, therefore can be included in the global analysis as an independent measurement of quark transversity. Di-hadron single spin symmetries from currently available data sample are calculated for different ranges of invariant mass and transverse momentum of the pairs. Discussion of the results and projections of statistical uncertainties for future transverse running are presented.

Acknowledgments

First of all, I would like to thank my adviser Professor Matthias Grosse-Perdekamp. My research would not be possible without his guidance in the past five years. As a nuclear physicist, he demonstrated to me how to find physics topics, how to work on a data analysis, how to run a hardware project, etc, which becomes a valuable part of my graduate student experience. I am also grateful to Professor Jen-Chieh Peng, with whom I had enjoyable discussions on a variety of physics topics.

Working at the UIUC PHENIX group gave me great joy. I had a great time with everyone here: John Koster, Beau Meredith, David Layton, Mickey Chiu, Ralf Seidl, Young-Jin Kim, Anselm Vossen and IhnJea Choi.

During the past three years at Brookhaven National Laboratory, I received tremendous help from the entire PHENIX collaboration. There are too many names to mention, here is only an incomplete list: I would like to thank John Haggerty, Cheng-Yi Chi, Martin Purschke, Chris Pinkenburg, Carla Vale, Jeff Mitchell, Joseph Seele, Loren Linden-Levy, Satoshi Yokkaichi, Yasushi Wanatabe and Tomoaki Nakamura for help on computing, Christine Aidala, Kieran Boyle and Alexander Bazilevsky for help on data analysis, Frank Toldo and Carter Biggs for help on hardware work.

Recalling my last year on Long Island, I would like to express my gratitude to Jia-Jia, for her encouragement and patience during difficult times.

Moreover, I thank my parents for their love and support.

Lastly, I thank all deities for creating the universe for us to reflect on.

Contents

Chapter 1

Introduction

1.1 Structure of the Proton

The ultimate goal of physics is to understand the matter world. It remained a puzzle for many centuries whether matter is infinitely divisible. Atoms were thought to be fundamental building blocks of matter, however, Rutherford showed in 1911 that they have their own internal structure. Going to even smaller scales, protons, neutrons and electrons became candidates for the fundamental elements.

The internal structure of the proton was probed through scattering experiments. At sufficiently high momentum (e.g. above GeV level), de Broglie wavelength of beam particle becomes very small (below 1 fm) thus giving access to sub-nucleon structure. In Deep inelastic scattering (DIS), a high energy beam scatters off a nucleon target. The Bjorken scaling phenomenon observed in DIS inspired Feynman, Gell-Mann and Zweig to propose models of proton structure, in which the proton is made up of three point-like constituent quarks. Each quark carries fractional charge and spin 1/2.

The observation of gluons in three-jet events and the measurements of momentum sum rules for quarks have further led to the conclusion that a large fraction of the proton momentum must be carried by gluons. Gluons are charge-neutral and are the carriers of the strong nuclear force.

Deep in-elastic electron-proton scattering (DIS) has pioneered the study of proton structure in the 1960s. At SLAC, the cross section for electron scattering off hydrogen targets was measured. To interpret the results, the cross section was compared with the Mott cross section which describes the scattering of electrons at relativistic energies off a point-like particle [1]:

$$\frac{d^2\sigma}{d\Omega dE'} = \left(\frac{d\sigma}{d\Omega}\right)^*_{Mott}\left[W_2(Q^2,\nu) + 2W_1(Q^2,\nu)\tan^2\frac{\theta}{2}\right] \tag{1.1}$$

where $Q^2 = -q^2$, $\nu = Pq/M$ with q being the four-momentum transfer, P and M being the four-momentum and invariant mass of the proton. The structure functions W_1 and W_2 are usually reformulated as

$$\begin{aligned} F_1(x,Q^2) &= Mc^2 W_1(Q^2,\nu) \\ F_2(x,Q^2) &= \nu W_2(Q^2,\nu) \end{aligned} \tag{1.2}$$

where $x = Q^2/2Pq$ is the Bjorken scaling variable. F_1 and F_2 extracted from DIS data revealed the fact that they are almost constant across a range of Q^2 when x is fixed [2]. This phenomenon, the so-called Bjorken scaling, indicated the existence of point-like constituents inside the proton. In addition, the measurements of the ratio $2xF_1/F_2$ implied that the point-like constituents carry spin 1/2. To interpret the DIS data, Bjorken and Feynman proposed the parton model in which the constituents, or partons, interact incoherently with the virtual photon. The structure functions can then be decomposed into the unpolarized parton distribution functions (PDFs), $q_x(x)$:

$$F_2(x) = 2xF_1(x) = x\sum_a e_a^2[q_a(x) + \bar{q}_a(x)] \tag{1.3}$$

where a denotes the flavors of quarks.

For the case of deep in-elastic scattering, the cross section at fixed Q^2 can be written as the product of the partonic scattering cross section and a sum of PDFs evaluated at x. In a properly chosen reference frame, x is equal to the longitudinal momentum fraction ξ is defined as

$$\xi \equiv p/P \tag{1.4}$$

where p is the four-momentum of the parton, and P the four-momentum of the proton [3]. Therefore, the unpolarized parton distribution functions are also called the "momentum distribution functions". The distribution functions $q_a(x)$ or $\bar{q}_a(x)$ can be seen as the probabilities of finding a quark or anti-quark inside a proton with longitudinal momentum fraction x.

The momentum of the proton is shared by quarks and gluons and the following momentum sum rule applies:

$$\int_0^1 dx \sum_a x[q_a(x) + \bar{q}_a(x)] + \int_0^1 dx\ xg(x) = 1 \tag{1.5}$$

Note that the sum here includes the neutral constituents (gluons), which is different from the sum in Eq. (1.3) where only the charged constituents (quarks) are considered.

High statistics data accumulated by various high precision DIS experiments (e.g. NMC, CCFR, BCDMS, H1 and ZEUS) in the past decades have been used as the primary source of information used in global QCD analysis to extract the unpolarized parton distribution functions [4]. The structure function F_2 measured in electron-proton, electron-neutron and neutrino-nuclei scattering can be expressed through different combinations of the distribution function for u, $\bar{u}$, d, $\bar{d}$, s and $\bar{s}$ quarks. F_2 measured in DIS experiments, along with other variables such as the charge asymmetry in W-boson production, the Drell-Yan cross section and the direct photon cross section, are fitted with specific parameterizations for the different distribution functions. The result from the fit in combination with perturbative QCD were then used to check the consistency of the fitting results with experimental observables [5, 6]. As an example, Fig. 1.1 shows the latest unpolarized parton distribution function obtained by the CTEQ collaboration. While the quark distribution functions are well constrained, there remains large uncertainties concerning the anti-quark distribution functions. In particular, the ratio of $\bar{d}$ and $\bar{u}$ at high x. Chapter 5 proposes measurements to constrain this ratio through observables in W boson production $p + p$ collisions.

On the theoretical side, perturbative QCD provides quantitative predic-

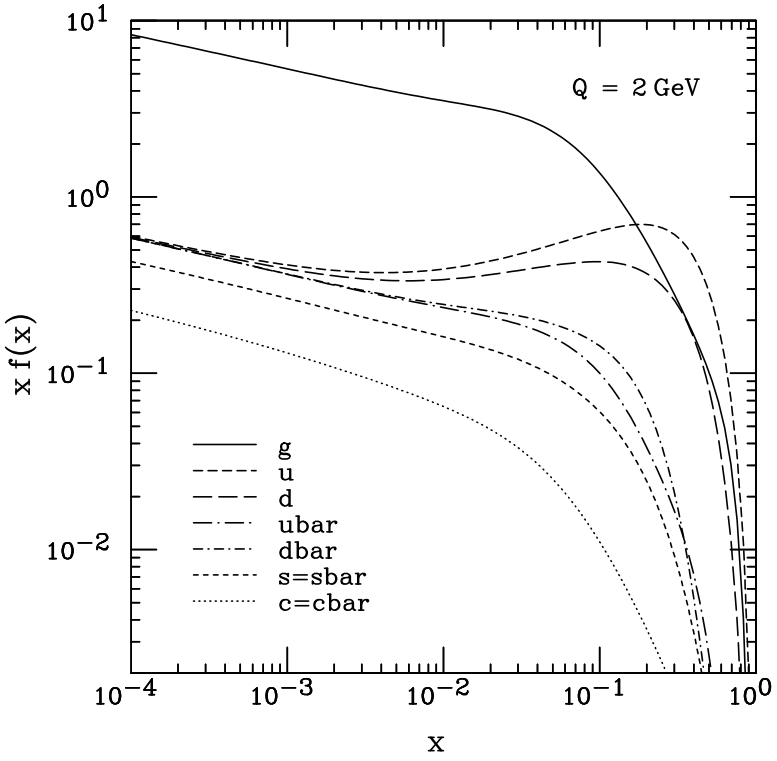

Figure 1.1: The unpolarized parton distribution function from a global QCD analysis by the CTEQ collaboration [6]. The distribution functions are shown for gluons and different flavors of quarks and anti-quarks.

tions only for hard scattering processes which involve quarks and gluons. In order to compare theoretical calculations with experimental measurements where quarks and gluons can only manifest themselves as constituents of hadrons due to color confinement, knowledge of proton structure and hadron fragmentation is required.

In the following, the example of deep inelastic lepton nucleon scattering will be used to formally define parton momentum distribution functions and also helicity and transversity distribution functions. According to the optical theorem, the inelastic scattering cross section equals to the imaginary part of elastic forward scattering amplitude. This gives rise to the so-called handbag diagram as shown in Fig. 1.2. The cross section can be written as [7]

$$\frac{d^2\sigma}{d\Omega dE'} = \frac{\alpha_{em}^2}{2MQ^4}\frac{E'}{E}L_{\mu\nu}W^{\mu\nu}. \tag{1.6}$$

Here $L_{\mu\nu}$ is the leptonic tensor that describes the emission of the virtual photon from the incident lepton and therefore can be calculated by perturbative QED [8].

The hadronic tensor $W^{\mu\nu}$ describes the interaction between the virtual photon and the hadron and can be parametrized into structure functions. The lower part of the handbag diagram is the quark-quark correlation matrix $\Phi_{ij}(k, P, S)$. By summing the undetected final state X, $\Phi_{ij}(k, P, S)$ becomes

$$\Phi_{ij}(k, P, S) = \int d^4\xi e^{\imath k\cdot\xi}\langle PS|\overline{\psi}_j(0)\psi_i(\xi)|PS\rangle. \tag{1.7}$$

It carries information on the distribution of quarks inside the hadron. Φ_{ij} cannot be calculated by perturbative QCD, therefore can only be parametrized and measured by experiments.

A natural parametrization is to decompose the matrix $\Phi(k, P, S)$ using Dirac matrices. At leading twist (order M/Q), only the vector, axial and tensor components survive

$$\Phi(x) = \frac{1}{2}\Big\{q(x)\,\not{P} + \lambda_N\,\Delta q(x)\,\gamma_5\,\not{P} + \delta q(x)\,\not{P}\,\gamma_5\,\not{S}_\perp\Big\}. \tag{1.8}$$

$q(x)$, $\Delta q(x)$ and $\delta q(x)$ are, respectively, the momentum distribution function, the helicity distribution function and the transversity distribution function.

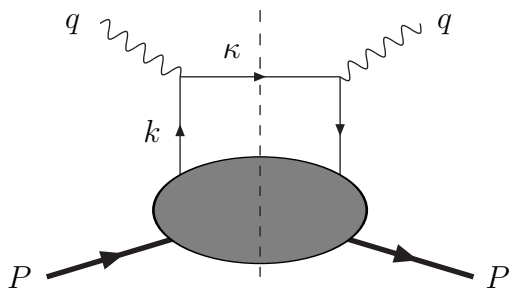

Figure 1.2: The "handbag" diagram describes the virtual photon interacting with a quark inside the hadron at leading order. q is the momentum of the virtual photon. P is the momentum of the hadron. k and κ are the momentum of the quark before and after interaction with the virtual photon.

Similar to the momentum distribution function, the helicity distribution function and the transversity distribution function also have probabilistic interpretations. Using the Pauli-Lubanski projectors $\mathcal{P}_\pm = \frac{1}{2}(1 \pm \gamma^5)$ and $\mathcal{P}_{\uparrow\downarrow} = \frac{1}{2}(1 \pm \gamma^1\gamma^5)$, $\Delta q(x)$ and $\delta q(x)$ can be written as [7]

$$\begin{aligned}\Delta q(x) &= \frac{1}{\sqrt{2}}\sum_n \delta((1-x)P^+ - P_n^+) \\ &\quad \times \left\{ \left|\langle PS|\mathcal{P}_+\psi_{(+)}(0)|n\rangle\right|^2 - \left|\langle PS|\mathcal{P}_-\psi_{(+)}(0)|n\rangle\right|^2 \right\}, \quad (1.9)\end{aligned}$$

$$\begin{aligned}\delta q(x) &= \frac{1}{\sqrt{2}}\sum_n \delta((1-x)P^+ - P_n^+) \\ &\quad \times \left\{ \left|\langle PS|\mathcal{P}_\uparrow\psi_{(+)}(0)|n\rangle\right|^2 - \left|\langle PS|\mathcal{P}_\downarrow\psi_{(+)}(0)|n\rangle\right|^2 \right\}. \quad (1.10)\end{aligned}$$

Therefore, $\Delta q(x)$ can be understood as the difference between probability densities of quarks that have positive or negative helicities inside a longitudinally polarized proton. For $\delta q(x)$, it is the difference of probability densities between quarks that have aligned or anti-aligned transverse spin orientation with respect to the proton spin when the proton is transversely polarized. A discussion of $\Delta q(x)$ and $\delta q(x)$ will follow in the next two sections.

1.2 Proton Spin Structure

1.2.1 Longitudinal Polarization

Spin adds another layer of complexity to understanding structure of the proton. The early parton model assumed that the sum of quarks' spin is responsible for the proton spin. However, DIS experiments have revealed that only a fraction of the proton spin arises from the quarks. Therefore, contributions from gluon spin and orbital angular momentum of both quarks and gluons should also be taken into consideration.

In analogy to the momentum sum rule as given in Eq. (1.5), a sum rule also exists for the proton spin

$$\frac{1}{2} = \frac{1}{2}\Delta\Sigma + \Delta g + \langle L_q \rangle + \langle L_g \rangle \tag{1.11}$$

where $\Delta\Sigma$ denotes quark spin contribution, ΔG denotes gluon spin contribution, L_q and L_g are orbital angular momentum from quarks and gluons.

To date, measurements on the quark spin content $\Delta\Sigma$ are available from polarized DIS experiments. A recent global QCD analysis using SLAC, EMC, SMC and HERMES results has shown that the quarks only contribute approximately 24% of the proton spin [9].

The recent global QCD analysis from DeFlorian, Sassot, Stratman and Vogelsang includes all available data from inclusive and semi-inclusive polarized DIS and polarized $p+p$ collisions to extract parton helicity distribution functions [10]. The results for sea quarks and gluon are shown in Fig. 1.3. DIS data point to positive $\Delta\bar{u}$ and negative $\Delta\bar{d}$, however large uncertainties still remain. The parity violating single spin asymmetries of W boson production in polarized $p+p$ collisions will be measured at RHIC and will contribute significantly to the determination of the anti-quark polarizations.

1.2.2 Transverse Polarization

It is also possible to study proton spin structure in high energy collisions with the proton spin oriented transverse to the momentum of the colliding particle

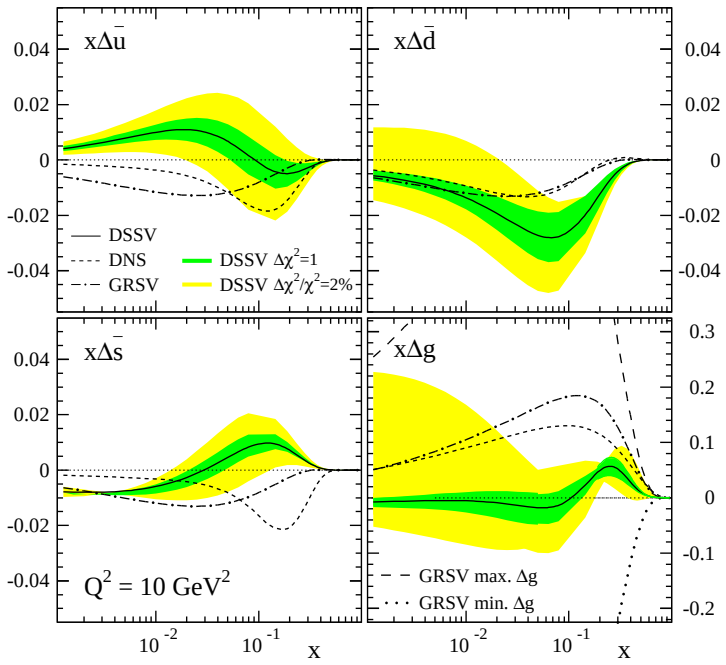

Figure 1.3: Polarized sea quark and gluon distribution functions as a function of x. The shaded bands correspond to uncertainties from fits with $\Delta\chi^2 = 1$ and $\Delta\chi^2/\chi^2 = 2\%$ [10].

momentum. Boosts and rotations do not commute for relativistic motion and therefore the difference between transverse and longitudinal quark spin distributions carries information about the relativistic motion of quarks inside protons.

The transverse polarization inside the proton is described by the so-called "transversity" distribution function. Given the chiral-odd property of transversity quark distributions [11], it cannot be probed directly in inclusive DIS. However, significant transverse spin asymmetries arise in processes where transversity is coupled with a second chiral-odd object.

A natural choice would be to study the double spin asymmetries A_{TT} in Drell-Yan production of lepton pairs. These spin asymmetries are proportional to the product of two quark transversity distributions. However, the spin asymmetries in $p+p$ is expected to be small as transversity distributions for anti-quarks in the proton are thought to be small. A similar measurement in $p + \bar{p}$ would yield higher asymmetries but would require polarized anti-proton beams.

In semi-inclusive DIS, where an additional hadron in the final state is observed in addition to the scattered electron, transversity couples with chiral-odd, spin-dependent fragmentation functions. Large single spin asymmetries have been observed first by the HERMES experiment at DESY.

The transversity distribution function was first introduced in 1979 by Ralston and Soper when considering the spin-dependent cross section of the Drell-Yan process [12]. The QCD evolution of transversity has been studied by Artru and Mekhfi and was found to decrease as Q^2 increases [13]. Many of the theoretical studies have focused on phenomenology, and have suggested various possible channels to measure transversity. There also exist several model calculations for the transversity distribution function, including calculations in the bag models, chiral models, light-cone models, spectator models, etc [7].

In addition to the model calculations, some basic relations exist to constrain transversity with the momentum and helicity distribution functions.

The probabilistic interpretations of the distribution functions leads to the following positivity bounds

$$|\Delta q(x)| \leq q(x), |\delta q(x)| \leq q(x). \tag{1.12}$$

The second constraint, first derived by Soffer [14] reads

$$q(x) + \Delta q(x) \geq 2|\delta q(x)|. \tag{1.13}$$

The first moment of the transversity distribution function is the tensor charge

$$g_T = \int_0^1 dx \sum_a [\delta q_a(x) - \delta \bar{q}_a(x)], \tag{1.14}$$

for which predictions from lattice QCD are available [15].

Finally, Bakker, Leader and Trueman [16] proposed the following sum rule:

$$\frac{1}{2} = \frac{1}{2} \int_0^1 dx \sum_a [\delta q(x) + \delta \bar{q}_a] + \sum_{q,\bar{q},g} \langle L_{S_T} \rangle \tag{1.15}$$

where L_{S_T} is the angular momentum L projected on transverse spin vector S_T.

The study of transversity is of particular interest: First, for non-relativistic quark motion the relation $\Delta q(x) = \delta q(x)$ holds as boosts and rotations commute for $v/c \ll 1$. As a consequence, the difference between the helicity distribution function and the transversity distribution function is a measure of the relativistic nature of the quarks inside the proton [17]. Secondly, since the gluon transversity distribution is 0 at leading order QCD and sea quark transversity distributions are expected to be small, quark transversity distributions provide a unique window to study the dynamics of valence quarks inside the proton.

Different from the momentum and helicity distribution functions, experimental knowledge of the transversity distribution functions is still very limited. The main reason for this is that the transversity distributions are not accessible in inclusive measurements as transversity distributions are chiral

odd quantities and parametrize the helicity flip amplitude of the hard scattering cross section. To explain the chiral-odd nature of the transversity distribution, consider the probabilistic interpretation in terms of the helicity flip amplitudes

$$\delta q(x) = q_{\uparrow}(x) - q_{\downarrow}(x) \sim Im(\mathcal{A}_{+-,-+}) \tag{1.16}$$

where the helicity amplitude is labeled with the quark and proton helicities in the initial state $(+-)$ and the final state $(-+)$. Both the quark and the proton helicities flip, as also illustrated in Fig. 1.4(a). Inclusive DIS conserves helicities of relativistic quarks [18], resulting in vanishing helicity flip amplitudes and small transverse spin asymmetries below the experimental sensitivities.

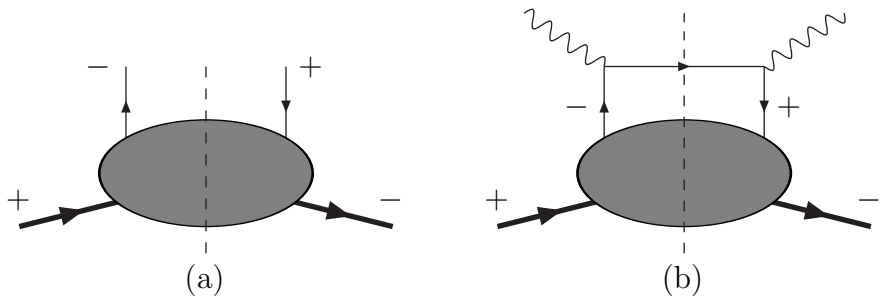

Figure 1.4: (a) The helicity amplitude for the transversity distribution function. Helicities of the quark and the hadron are denoted by "+" and "-" on the figure. (b) The diagram for inclusive DIS which is suppressed by helicity conservation.

The helicity flip in the amplitude also explains that there is no gluon transversity distribution at leading order QCD, since helicity flip for gluons requires the exchange of 2 units of angular momentum.

In order to measure transversity, observables with a second chiral-odd function are needed so that the overall chirality is even. A natural choice would be the Drell Yan process with transverse double spin asymmetries re-

lated to the product of two transversity distributions. A second possibility are measurements in semi-inclusive processes in which transversity distributions appear in connection with a chiral-odd fragmentation function. These measurements can be carried out in both semi inclusive DIS and proton-proton collisions. An overview of different possible measurements and their present status will be briefly discussed in the following paragraphs.

Drell Yan measurements require two polarized beams of protons or protons and anti-protons. Transversity distributions can be obtained from the measurement of the double spin asymmetry A_{TT} for the Drell Yan process

$$A_{TT} = \frac{\sigma_{\uparrow\uparrow} - \sigma_{\uparrow\downarrow}}{\sigma_{\uparrow\uparrow} + \sigma_{\uparrow\downarrow}} \propto \delta q(x_a) \otimes \delta q(x_b). \tag{1.17}$$

The advantage of Drell-Yan measurement is that transversity is the only unknown quantity in the measured asymmetry, and no fragmentation function is involved.

The measurement of Drell-Yan A_{TT} can be carried out at the Relativistic Heavy Ion Collider (RHIC) in the future [19]. However, by saturating the bounds of Soffer's inequality as given in Eq. 1.13, a model calculation in Ref. [20] has shown that the asymmetry will be only $1\% \sim 2\%$. The small cross section of the Drell-Yan process in general and the limited acceptance of muon detectors of PHENIX experiment at RHIC will make this measurement quite demanding in terms of luminosity. The Drell-Yan asymmetry itself is small at RHIC since transversity distributions for anti-quarks are expected to be small.

The other option for double spin asymmetry measurements in the Drell-Yan process is to collide polarized protons with polarized anti-protons. In this case, the asymmetry is much larger according to model calculation [21], up to $20\% \sim 50\%$. However, the very challenging technical problem of achieving high enough polarization for anti-proton beams will need to be solved first.

In semi-inclusive DIS or hadron-hadron collision where at least one hadron in the final state is detected, transversity can be coupled with a chiral-odd fragmentation function. The most familiar example is the Collins fragmen-

tation function $H_1^\perp$. It is the spin-dependent component of the quark fragmentation function [22]

$$D_h^{q\uparrow}(z, \mathbf{P}_{h\perp}) = D_1^{q,h}(z, \mathbf{P}_{h\perp}) + H_1^{\perp q,h}(z, \mathbf{P}_{h\perp}^2) \cdot \frac{(\hat{\mathbf{k}} \times \mathbf{P}_{\mathbf{h}\perp}) \cdot \mathbf{S}_q}{zM_h}. \tag{1.18}$$

Its probabilistic interpretation is the probability for a quark with momentum $\mathbf{k}$ and transverse spin $\mathbf{S}_q$ to fragment into a hadron with fractional energy $z = E_h/E_q$ relative to the quark energy and transverse momentum $\mathbf{P}_{h\perp}$ relative to the quark momentum $\mathbf{k}$.

As an example of the inclusive single hadron measurement, the E704 experiment, a fixed target experiment with $\sqrt{s} = 19.4$ GeV at FNAL, has observed very large single spin asymmetries for inclusive pion production in the early 1990s. The analyzing power of the single spin asymmetry in this experiment is

$$A_N = -\frac{1}{P_B \cos\phi} \frac{N_\uparrow(\phi) - N_\downarrow(\phi)}{N_\uparrow(\phi) + N_\downarrow(\phi)} \tag{1.19}$$

where ϕ is the angle between the polarization direction and the normal vector of the pion production plane. The largest A_N observed is as high as 40% [23]. This result has triggered significant theoretical interests in the field of transverse spin physics. However, both theoretical work and later measurement have shown that the convolution of transversity and the Collins fragmentation function are not the only mechanism that contributes to the large observed single spin asymmetry. In fact, A_N arises from the combination of two leading twist effects: the Collins effect and the Sivers effect:

$$A_N \propto \delta q \otimes H_1^\perp + q \otimes f_{1T}^\perp. \tag{1.20}$$

First proposed in [24], the Sivers effect is related to intrinsic motion of quarks inside the proton and therefore explains the observed single spin asymmetries as an initial state effect. For comparison, in the Collins effect the asymmetry rises from the spin dependence of the quark fragmentation process in the final state.

Semi-inclusive measurements in DIS experiments are able to disentangle these effects based on the different angular dependences of the asymmetries

for the different effects. Schematically, the single spin asymmetry for semi-inclusive DIS at leading twist can be written as

$$A_{UT} \propto \sin(\phi_h + \phi_S)\delta q \otimes H_1^{\perp} + \sin(\phi_h - \phi_S) q \otimes f_{1T}^{\perp} \tag{1.21}$$

where ϕ_h is the angle between the transverse momentum of the hadron and the scattering plane (a plane constructed by the momenta of the virtual photon and the lepton) and ϕ_S is the angle between polarization direction of the target and the scattering plane as shown in Fig. 1.5.

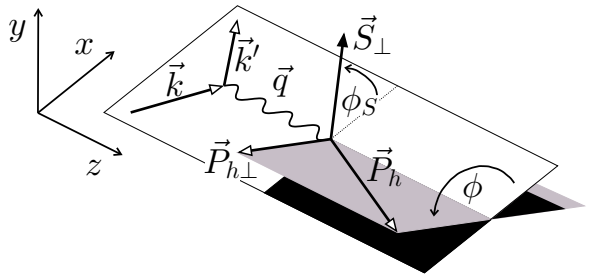

Figure 1.5: The azimuthal angles used in the measurement of single spin asymmetry of single hadron measurement by the HERMES experiment [25]. (The angle ϕ in the figure is actually the angle ϕ_h used in Eq. (1.22).)

Therefore, by measuring the moment $A_{UT}^{\sin(\phi_h \pm \phi_S)}$ of the single spin asymmetry which is defined as

$$A_{UT}^{\sin(\phi_h \pm \phi_S)} \equiv 2\langle \sin(\phi_h \pm \phi_S) \rangle = \frac{\int d\phi_h d\phi_S \sin(\phi_h \pm \phi_S)[d\sigma(\phi_S) - d\sigma(\phi_S + \pi)]}{\int d\phi_h d\phi_S [d\sigma(\phi_S) + d\sigma(\phi_S + \pi)]}, \tag{1.22}$$

the transversity effect can be separated from the Sivers effect. First experimental results come from the HERMES experiment where the $\sin(\phi_h + \phi_S)$ moment has been measured to be nonzero for π^+ and π^-, the $\sin(\phi_h - \phi_S)$ moment has been measured to be nonzero for π^+ and consistent with zero for π^- [25]. From this HERMES data it is evident that both the Collins effect and the Sivers effect exist. In addition to the HERMES results, experimental results on the $\sin(\phi_h \pm \phi_S)$ moments are also available from the COMPASS experiment where a deuteron target was used and both moments are found

to be compatible with zero [26], consistent with theoretical expectation for a deuteron target.

A phenomenological analysis has been carried out to extract the transversity distribution function. The moment $A_{UT}^{\sin(\phi_h+\phi_S)}$ is a convolution of transversity and the Collins fragmentation function. Therefore, knowledge of the Collins fragmentation function is required to extract transversity from HERMES results. In 2006, the BELLE collaboration published the first independent measurement of the Collins fragmentation function by observing azimuthal asymmetries in hadron-hadron correlations for inclusive di-hadron production $e^+e^- \to hhX$ [22]. As a "proof of principle"-analysis, Anselmino et al. [27] have used $A_{UT}^{\sin(\phi_h+\phi_S)}$ measured by the HERMES and COMPASS collaborations combined with the di-hadron azimuthal asymmetries measured at BELLE to perform a global fit to extract the transversity distributions for up and down quarks and the Collins fragmentation function simultaneously. The fitting results for transversity are shown on Fig. 1.6. Although the uncertainties are still large for these results, it is worth noticing that the sign for u and d quarks are opposite to each other, the size of δu is larger than δd and both are much smaller than the Soffer bounds. The principal uncertainties in the global Collins QCD analysis arise from the unknown k_T or p_T dependence of the Collins fragmentation function and the transversity distribution function and the reliance on factorization for transverse momentum dependent distributions and fragmentation functions.

The measurement proposed in this article follows the general strategy of the global analysis as mentioned above. However, instead of requiring one hadron to be detected as in the asymmetry related to the Collins fragmentation function, this measurement will require two hadrons in the final state. Therefore, the corresponding spin-dependent fragmentation function will describe a transversely polarized quark fragmenting into two hadrons. This fragmentation function is usually referred to as "interference fragmentation function" (IFF) in the literature, and $H_1^{\sphericalangle}$ for notation.

In 1994, Collins, Heppelmann and Ladinsky suggested the measurement

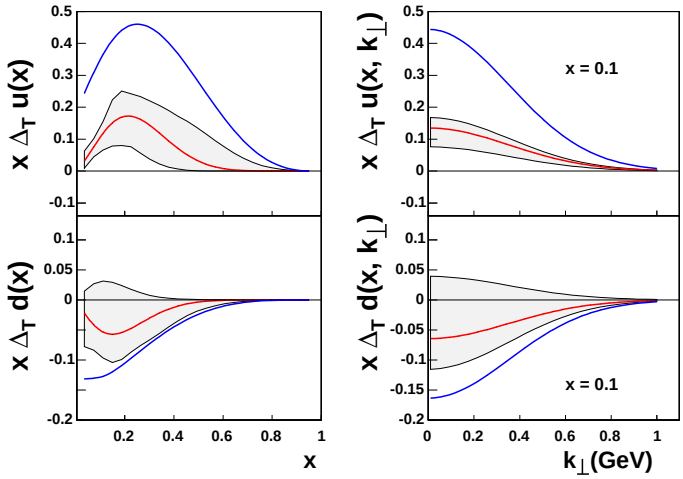

Figure 1.6: The transversity distribution obtained by Anselmino and collaborators [27] from a global QCD analysis of single spin asymmetry measured by HERMES and COMPASS and Collins asymmetries measured at BELLE. The transversity distribution functions are shown for u and d quarks with their dependence on the momentum fraction x and transverse momentum $k_\perp$.

of single spin asymmetries of two hadrons inside the same jet [11]. For the measurement in DIS, Jaffe, Jin and Tang [28] predicted a sign change of the interference fragmentation function while model calculation by Radici, Jakob and Bianconi [29] came to different conclusions. For the measurement in hadron-hadron collisions, Tang [30] gives quantitative predictions at RHIC energies while a more comprehensive calculation of the asymmetry has been done by Bacchetta and collaborators [31, 32].

On the experimental side, first non-zero results for IFF single spin asymmetries in DIS were shown by HERMES [33]. It is worth noticing that the HERMES result doesn't show a sign change of the asymmetry as predicted by Ref. [28], but shows asymmetries similar to what has been predicted by Ref. [29]. The result from COMPASS [34], where a deuteron target was used, shows zero asymmetry within the statistical uncertainty. The experimental measurement of this proposal will be the first one in hadron-hadron collision. In the following sections, the interference fragmentation function and the sin-

gle spin asymmetry of di-hadron production in hadron-hadron collision will be discussed with more details.

1.3 Interference Fragmentation Function and Transversity

The quark transversity distribution function describes the transverse polarization of the quarks inside the proton [12]. Due to the chiral-odd nature of transversity, it can only be measured when coupled with another chiral-odd function. One possible candidate is to couple transversity with a spin-dependent di-hadron fragmentation function (usually referred to as "interference fragmentation function" or "IFF" in the literature [11] [28]).

In proton-proton collisions where one proton is transversely polarized, the difference of cross sections of hadron pair produced in two different spin states, or the polarized cross section, is a convolution of the following terms [11]:

$$d\sigma_{UT} \sim q(x_1) \otimes \delta q(x_2) \otimes \Delta\hat{\sigma} \otimes H_1^{\sphericalangle}(z, M). \tag{1.23}$$

Here $q(x)$ and $\delta q(x)$ are the unpolarized parton distribution and the transversity distribution function respectively. z and M are the fractional energy and the invariant mass of the hadron pair, respectively. $\hat{\sigma}$ is the partonic cross section, and $H_1^{\sphericalangle}$ is the interference fragmentation function. A single spin asymmetry can then be defined as the ratio of the polarized cross section to the unpolarized cross section:

$$A_{UT} = \frac{\sigma_{\uparrow} - \sigma_{\downarrow}}{\sigma_{\uparrow} + \sigma_{\downarrow}}, \tag{1.24}$$

where the arrows indicate the polarization orientation. This asymmetry contains information from the transversity distribution function and the interference fragmentation function. A theoretical framework [31] has been setup for the interpretation of this single spin asymmetry at leading order in $1/|p_T|$ where p_T is the transverse momentum of the hadron pair, i.e. at leading twist.

In the experiments, the asymmetry is defined as

$$A_{UT}(\phi) = \frac{1}{P}\frac{N_\uparrow(\phi)/L_\uparrow - N_\downarrow(\phi)/L_\downarrow}{N_\uparrow(\phi)/L_\uparrow + N_\downarrow(\phi)/L_\downarrow} \tag{1.25}$$

where $N_\uparrow$ and $N_\downarrow$ are the counts of di-hadron pairs, $L_\uparrow$ and $L_\downarrow$ are the luminosities of the beam with the arrows indicating polarization directions of the proton beam, and P is the beam polarization. Note that this asymmetry depends on an azimuthal angle ϕ which is the angle between the polarization direction and the two-hadron plane. A $\sin\phi$ modulation is expected for the single spin asymmetry A_{UT} [31], therefore the measured asymmetry needs to be fit with a sine function

$$A_{UT}(\phi) = A_{UT}^{\sin\phi}\sin\phi \tag{1.26}$$

to extract the analyzing power $A_{UT}^{\sin\phi}$ which contains the convolution of the transversity distribution function and the interference fragmentation function.

In the following discussions, definitions of angles, vectors and planes follows the scheme developed by Bacchetta and Radici in Ref. [31].

As shown in Fig. 1.7(a), two protons with momenta P_A and P_B and spin vectors S_A and S_B collide. Two vectors related to final state are defined as $P_C = P_{C1}+P_{C2}$ and $R_C = (P_{C1}-P_{C2})/2$ where P_{C1} and P_{C2} are the momenta of the two hadrons produced inclusively. $P_{C\perp}$ is the transverse component of P_C with respect to P_A and is used as the hard scale of the process. It is assumed that $P_{C\perp}$ is much larger than the mass of the colliding hadrons and

the produced hadrons [31]. In addition, three azimuthal angles are defined:

$$\cos\phi_{S_A} = \frac{(\hat{\mathbf{P}}_A \times \mathbf{P}_C)}{|\hat{\mathbf{P}}_A \times \mathbf{P}_C|} \cdot \frac{(\hat{\mathbf{P}}_A \times \mathbf{S}_A)}{|\hat{\mathbf{P}}_A \times \mathbf{S}_A|}, \quad \sin\phi_{S_A} = \frac{(\mathbf{P}_C \times \mathbf{S}_A) \cdot \hat{\mathbf{P}}_A}{|\hat{\mathbf{P}}_A \times \mathbf{P}_C|\,|\hat{\mathbf{P}}_A \times \mathbf{S}_A|}, \tag{1.27}$$

$$\cos\phi_{S_B} = \frac{(\hat{\mathbf{P}}_B \times \mathbf{P}_C)}{|\hat{\mathbf{P}}_B \times \mathbf{P}_C|} \cdot \frac{(\hat{\mathbf{P}}_B \times \mathbf{S}_B)}{|\hat{\mathbf{P}}_B \times \mathbf{S}_B|}, \quad \sin\phi_{S_B} = \frac{(\mathbf{P}_C \times \mathbf{S}_B) \cdot \hat{\mathbf{P}}_B}{|\hat{\mathbf{P}}_B \times \mathbf{P}_C|\,|\hat{\mathbf{P}}_B \times \mathbf{S}_B|}, \tag{1.28}$$

$$\cos\phi_{R_C} = \frac{(\hat{\mathbf{P}}_C \times \mathbf{P}_A)}{|\hat{\mathbf{P}}_C \times \mathbf{P}_A|} \cdot \frac{(\hat{\mathbf{P}}_C \times \mathbf{R}_C)}{|\hat{\mathbf{P}}_C \times \mathbf{R}_C|}, \quad \sin\phi_{R_C} = \frac{(\mathbf{P}_A \times \mathbf{R}_C) \cdot \hat{\mathbf{P}}_C}{|\hat{\mathbf{P}}_C \times \mathbf{P}_A|\,|\hat{\mathbf{P}}_C \times \mathbf{R}_C|}. \tag{1.29}$$

Another angle θ_C is defined as the angle between one final state hadron's momentum in the center of mass frame of the hadron pair and P_C in the laboratory frame as shown in figure 1.7(b).

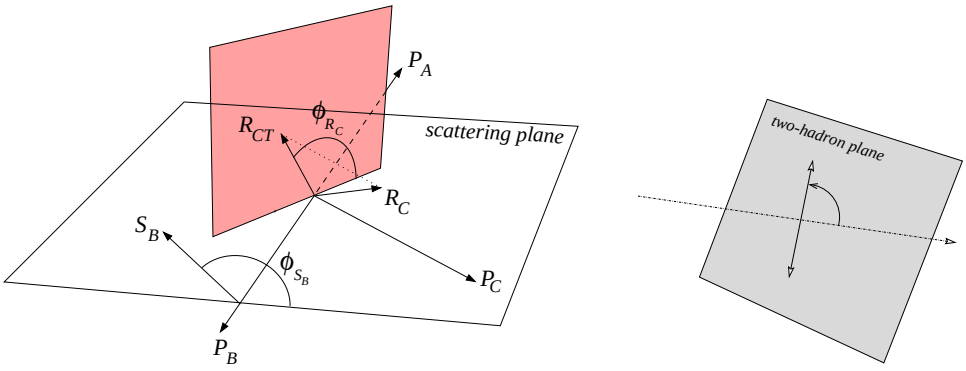

Figure 1.7: (a) An illustration of angles ϕ_{R_C} and ϕ_{R_C} as defined by Eq. (1.28)(1.29). (b) An illustration of the angle θ_C.

The differential cross section $d\sigma$ of di-hadron production in hadron-hadron collisions depends on seven variables, one choice is η_C, $|P_{C\perp}|$, θ_C, M_C, ϕ_{R_C}, ϕ_{S_A}, ϕ_{S_B} where M_C is the invariant mass of the di-hadron pair, η_C is the pseudorapidity of the hadron pair or $\eta_C = -\ln[\tan(\theta/2)]$ in which θ is the

angle between P_C and P_A. The differential cross section can be written as [31]

$$\begin{aligned}
&\frac{d\sigma}{d\eta_C\, d|\mathbf{P}_{C\perp}|\, d\cos\theta_C\, dM_C^2\, d\phi_{R_C} d\phi_{S_A} d\phi_{S_B}} \\
= \;& 2\,|\mathbf{P}_{C\perp}| \sum_{a,b,c,d} \frac{1}{4} \sum_{(\text{all } \chi'\text{s})} \int \frac{dx_a dx_b dz_c}{4\pi^2 z_c^2} \\
& \Phi'_a(x_a, S_A)_{\chi'_a\chi_a}\, \Phi'_b(x_b, S_B)_{\chi'_b\chi_b} \\
& \times \frac{1}{16\pi\hat{s}^2}\, \hat{M}_{\chi_c,\chi_d;\chi_a,\chi_b}\, \hat{M}^*_{\chi'_a,\chi'_b;\chi'_c\chi'_d}\, \Delta'_c(z_c, \cos\theta_C, M_C^2, \phi_{R_C})_{\chi'_c\chi_c} \\
& \times \delta_{\chi'_d\chi_d}\, \hat{s}\, \delta(\hat{s}+\hat{t}+\hat{u}).
\end{aligned} \tag{1.30}$$

x_a and x_b are the fractional momenta of the two partons in the hard scattering process. Φ'_a and Φ'_b are the quark-quark correlation matrices, and contain the transversity distribution function as off-diagonal matrix elements when the partons are quarks. Δ'_c denotes the quark-quark correlation matrix for di-hadron production which contains the interference fragmentation function $H_1^{\sphericalangle}$ as the off-diagonal matrix elements. The corresponding diagram is illustrated in Fig. 1.8.

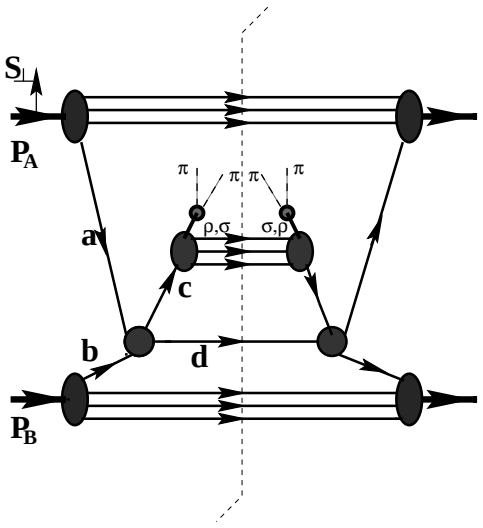

Figure 1.8: The diagram for the process $pp^{\uparrow} \to \pi\pi X$. This figure is taken from Ref. [30], the labels "A" and "B" need to be switched to comply with the notion used in this article.

Now consider hadron-hadron collisions where only one beam is polarized,

ϕ_{S_A} can be integrated out and the single spin asymmetry of di-hadron production is defined as

$$A_N(\eta_C, |P_{C\perp}|, \theta_C, M_C, \phi_{R_C}, \phi_{S_B}) = \frac{d\sigma^{\uparrow} - d\sigma^{\downarrow}}{d\sigma^{\uparrow} + d\sigma^{\downarrow}} \tag{1.31}$$

where the denominator is the unpolarized differential cross section $d\sigma_{UU}$ and the numerator is the polarized differential cross section $d\sigma_{UT}$. Starting with Eq. (1.30), Ref. [31] derived the following results:

$$d\sigma_{UU} = 2\,|\mathbf{P}_{C\perp}| \sum_{a,b,c,d} \int \frac{dx_a dx_b}{4\pi^2 z_c}\, q_1^a(x_a)\, q_1^b(x_b)\, \frac{d\hat{\sigma}_{ab\to cd}}{d\hat{t}}\, D_{1,oo}(\bar{z}_c, M_C^2), \tag{1.32}$$

$$\begin{aligned} d\sigma_{UT} = {} & 2\,|\mathbf{P}_{C\perp}| \sum_{a,b,c,d} \frac{|\mathbf{R}_C|}{M_C}\, |\mathbf{S}_{BT}|\, \sin\left(\phi_{S_B} - \phi_{R_C}\right) \\ & \times \int \frac{dx_a dx_b}{16\pi z_c}\, q_1^a(x_a)\, \delta q^b(x_b)\, \frac{d\Delta\hat{\sigma}_{ab^{\uparrow}\to c^{\uparrow}d}}{d\hat{t}} H_{1,ot}^{\sphericalangle c}(\bar{z}_c, M_C^2)\ . \end{aligned} \tag{1.33}$$

The sine function modulation $\sin\left(\phi_{S_B} - \phi_{R_C}\right)$ in Eq. (1.33), which is important for experimental measurements, comes from the $e^{\pm i\phi_{S_B}}$ dependence of ϕ_{S_B} in the off-diagonal term in quark-quark correlation matrix Φ and the $e^{\pm i\phi_{R_C}}$ dependence of ϕ_{R_C} in the off-diagonal term in quark-quark correlation matrix Δ.

The partonic cross section is defined as

$$\frac{d\Delta\hat{\sigma}_{ab^{\uparrow}\to c^{\uparrow}d}}{d\hat{t}} \equiv \frac{1}{16\pi\hat{s}^2}\,\frac{1}{4} \sum_{(\text{all } \chi\text{'s})} \hat{M}_{\chi_c,\chi_d;\chi_a,\chi_b}\, \hat{M}^*_{\chi_a,-\chi_b;-\chi_c,\chi_d}. \tag{1.34}$$

Here the arrows indicate that the partons b and c are transversely polarized. This cross section can be calculated by perturbative QCD.

The unpolarized parton distribution function $q(x)$ is already measured with good accuracy as introduced in the first section. The transversity distribution function $\delta q(x)$ is the goal of this measurement.

Although the interference fragmentation function $H_1^{\sphericalangle}$ is also unknown and can only be determined by experimental measurements, a partial wave analysis of the correlation matrix Δ was carried out by Ref. [31, 32] to model the θ_C dependence of D_1 and $H_1^{\sphericalangle}$. These two fragmentation functions are

expanded in the basis of Legendre polynomials of $\cos\theta_C$ and truncated at $L = 1$:

$$\begin{aligned} D_1(z_c, \cos\theta_C, M_C^2) &\rightarrow D_{1,oo}(z_c, M_C^2) + D_{1,ol}(z_c, M_C^2)\,\cos\theta_C \\ &+ D_{1,ll}(z_c, M_C^2)\,\frac{1}{4}\,(3\cos^2\theta_C - 1)\,, \qquad (1.35) \\ H_1^{\sphericalangle}(z_c, \cos\theta_C, M_C^2) &\rightarrow H_{1,ot}^{\sphericalangle}(z_c, M_C^2) + H_{1,lt}^{\sphericalangle}(z_c, M_C^2)\,\cos\theta_C\,. \qquad (1.36) \end{aligned}$$

Here o, l, t in the subscripts indicate polarization state of the pair in the center of mass frame, which correspond to two hadrons in a relative $L = 0$ wave and in a relative $L = 1$ wave with longitudinal and transverse polarization with respect to P_C. Due to this θ_C dependence, only $H_{1,ot}^{\sphericalangle}$ shows up in the polarized cross section as seen in Eq. 1.33. And $H_{1,ot}^{\sphericalangle}$ is the interference between the amplitudes of a pair with relative $L = 0$ and a pair with $L = 1$ and transversely polarized relative to P_C.

It is evident that the behavior of $H_{1,ot}^{\sphericalangle}$ in the current fragmentation region is crucial for the single spin asymmetry measurements. For the interference between $L = 0$ and $L = 1$, or the s-p wave interference, Jaffe and collaborators argued in Ref. [28] that a sign change of the interference term $H_{1,ot}^{\sphericalangle}$ should be expected based on a partial wave analysis of $\pi\pi$ scattering data [35], however, early work by Collins and Ladinsky had assumed the interference of a s-wave with a narrow resonance and a continuum p-wave [36]. For the pure p-wave fragmentation function $H_{1,lt}^{\sphericalangle}$, Bacchetta and collaborators [31] pointed out that it should have a structure similar to a Breit-Wigner distribution around the ρ mass.

The possibility to measure the interference fragmentation function through the correlation of two di-hadron pairs in e^+e^- annihilation was studied by Artru and Collins [37]. Later Boer, Jakob and Radici [38] studied the same asymmetry using modern notation.

On the experimental side, the measurement of the interference fragmentation function is an ongoing effort at the BELLE experiment [39]. This measurement is analogous to the measurement of the Collins fragmentation function in $e^+e^- \rightarrow hhX$ [22]. One difference is that the measurement

of the interference fragmentation function requires detecting two di-hadron pairs coming from back-to-back jets in the electron-position annihilation: $e^+e^- \rightarrow (\pi\pi)_{jet}(\pi\pi)_{jet}$. The full differential cross section can be found in Ref. [38] as well as definitions of the azimuthal angles. The azimuthal angle used for this measurement is the sum of the azimuthal angles of each hadron plane relative to the lepton plane. The hadron plane is defined by the momenta of each di-hadron pair. The lepton plane is defined by the beam axis and the thrust axis. The asymmetry is selected by a specific angular modulation and is a convolution of two interference fragmentation functions $H_1^{\sphericalangle}$ of different parameters[1].

[1]The measurements of Collins fragmentation function and IFF at the BELLE experiment have been carried out by the Illinois group in collaboration with RIKEN-BNL Research Center (RBRC)

Chapter 2

Experimental Setup

2.1 Relativistic Heavy Ion Collider and Polarized p+p Collisions

The Relativistic Heavy Ion Collider (RHIC) located at Brookhaven National Laboratory has the ability to collide protons and heavy ions such as gold, lead and copper at high energy. In case of polarized protons, single beam energy goes up to 250 GeV and each beam contains 120 bunches of 2×10^{11} protons spaced by 106 ns in time. Polarization of the proton at RHIC starts with an intense polarized H^- source. The protons are then fed to smaller accelerators including Alternating Gradient Synchrotron (AGS). Protons with 70% polarization at 22 GeV are transferred to RHIC[19]. Polarization direction of each bunch can be controlled so that all different combination of spin patterns are tested in the experiment in order to minimize bias. Furthermore, the proton spin orientation at the interaction points can be manipulated by spin rotator magnets and sets of helical dipole magnets, so called Siberian snakes, are used to preserve the proton polarization during acceleration [1]

Since all measurement in spin physics depends on knowledge of polarization, it is measured at RHIC with physics processes with known analyzing

[1]Each set of Siberian snake helical dipole magnets flips the proton spin on each pass thereby canceling the spin precession from possible de-polarizing resonances.

power, such as elastic proton-proton scattering and elastic proton-carbon scattering in the Coulomb nuclear interference region[40]. In addition, at the PHENIX experiment, magnitude and direction of polarization can be monitored in real time from single spin asymmetry in forward neutron production.

2.2 The PHENIX Experiment

PHENIX, one of the experiments at RHIC, is a detector which consists of two muon spectrometer arms at forward rapidity and two central spectrometer arms at central rapidity. The central arms have a pseudo-rapidity coverage of $|\eta| < 0.35$, and cover two azimuthal intervals of 90°, each offset 33.75° from the vertical direction [41]. The central arms are referred to as the "east arm" and the "west arm". The layout of the PHENIX detector is illustrated in Fig. 2.1.

For the analysis presented in this thesis the two central arms plus the Beam-beam Counters have been used to measure pairs of charged hadrons and pairs of a neutral pion and a charged hadron.

The Beam-Beam Counters (BBC) [42] is used at PHENIX to trigger collisions. Each BBC, consisting of 64 photomultiplier tubes, is located 1.44 meters downstream or up stream of the interaction point and covers pseudorapidity range of 3.0 to 3.9 and 2π in azimuth. By comparing the times measured in two BBCs, location and time of the collision can be determined. The location, usually called the vertex, is then used as the origin for all particles in tracking detectors and calorimeters. The time, usually called t_0, is used as the start time in TOF (Time of Flight) detector.

The Electromagnetic Calorimeters (EMCal) [43] are used to measure electromagnetic showers (mainly from photons, electrons) in the central arm. Two sectors of the detector in the east were built from Lead Glass (PbGl) towers with size of 5.5 cm × 5.5 cm while the other six sectors were built from Lead Scintillator (PbSc) towers with of size 4.0 cm × 4.0 cm. The eight sectors combined together provide coverage that is identical to the two

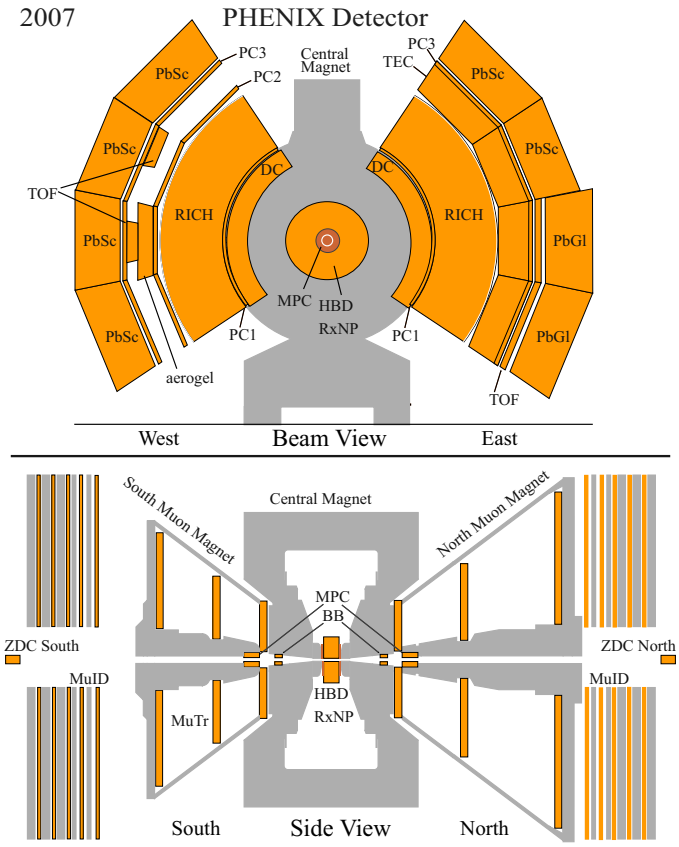

Figure 2.1: The configuration of the PHENIX detector for run 2007. A full description of the PHENIX detector can be found in Ref. [41].

PHENIX central arms.

The detectors for charged tracking used in the analysis include two sets of wire chambers, the Drift Chamber (DC) and the Pad Chambers (there are three layers: PC1, PC2 and PC3). DC is mainly used for measurement of transverse momentum p_T of charged tracks, PC1 is responsible for measurement of longitudinal momentum p_z of charged tracks. A detailed description of the tracking chambers can be found in Ref. [44].

2.3 Offline Data Reconstruction at PHENIX

Offline data reconstruction[2], or data production, refers to the procedure in PHENIX to process raw data where detector hits are converted to particle tracks via pattern recognition before physics analysis can be carried out. It requires intensive computing resources including CPU time, disk/tape storage space, and network traffic.

Before data production starts, related software needs to be ready and verified by various subsystem experts. In addition, initial calibration for EMCal tower-by-tower energy scale, RICH mirror alignment, Drift Chamber alignment and all online calibrations are required to have a satisfactory status. For remote sites such as CCJ (Computing Center in Japan), the calibration database must be updated following changes in the database at RCF (RHIC Computing Facility) in a timely manner.

Data production can be divided into three phases: reconstruction from raw data to nano-DST's (nDSTs), aggregation of nDSTs into larger files and transfer of those files to their final destination.

Reconstruction starts from the raw data files. Data from a physics run (usually corresponds to 1 hour or shorter running time) are organized into 5 GB (in case of run8 data) or 10 GB (in case of run9 data) files, often called

[2]The author carried out data production projects for PHENIX Run6 and Run8 p+p datasets at Brookhaven National Laboratory and at the Japanese Institute of Physical and Chemical Studies (RIKEN).

"segments". To process a segment, each event is examined by a collection of software made by different subsystem groups. Hits are reconstructed into particle tracks via pattern recognition, information from different detectors are then combined to provide refined tracking results (e.g. charged particle tracking in the PHENIX central arm and muon arms). The resulting data stream is divided further by types of particles (such as photons in the central arm, charged tracks in the central arm, charged tracks in the muon arms, etc) and different triggers (such as MinBias triggers, photon triggers, muon triggers, etc). Figure 2.2 shows an example of the sizes for all nDSTs for the PHENIX run8 p+p 200 GeV data.

Once all the segments in a physics run were processed, they were combined into larger files (1.6 GB for run8 data and 4 GB for run9 data) for efficient storage on tape/disk. The produced files were transferred to their final destination at RCF.

The following sections give brief overviews of RCF and CCJ, and some more details about data reconstruction and data transfer.

2.3.1 RHIC Computing Facility

The RHIC Computing Facility (RCF) was established in the 1990s to support computing needs of the four experiments at RHIC [45]. Later it was expanded to support computing tasks for the ATLAS experiment, and became the RHIC/ATLAS Computing Facility (RACF). The core of RCF is a computing farm of 1700 hosts with 5200 cores where 3300 cores are dedicated to RHIC experiments. Experimental data are served by an HPSS (High Performance Storage System) mass storage system, a dCache distributed storage system and an NFS (Network File System) central storage. The HPSS system is backed by tape robotics libraries (3 Sun StorageTek SL500 silos) with total storage capability of 8 PB and average transfer rate 350-400 MB/s over 5 movers [46]. For distributed storage, the dCache system [47] manages 400 TB storage mostly on disks of the computing nodes. The NFS system used for PHENIX was based on SUN x4500 servers which were capable of

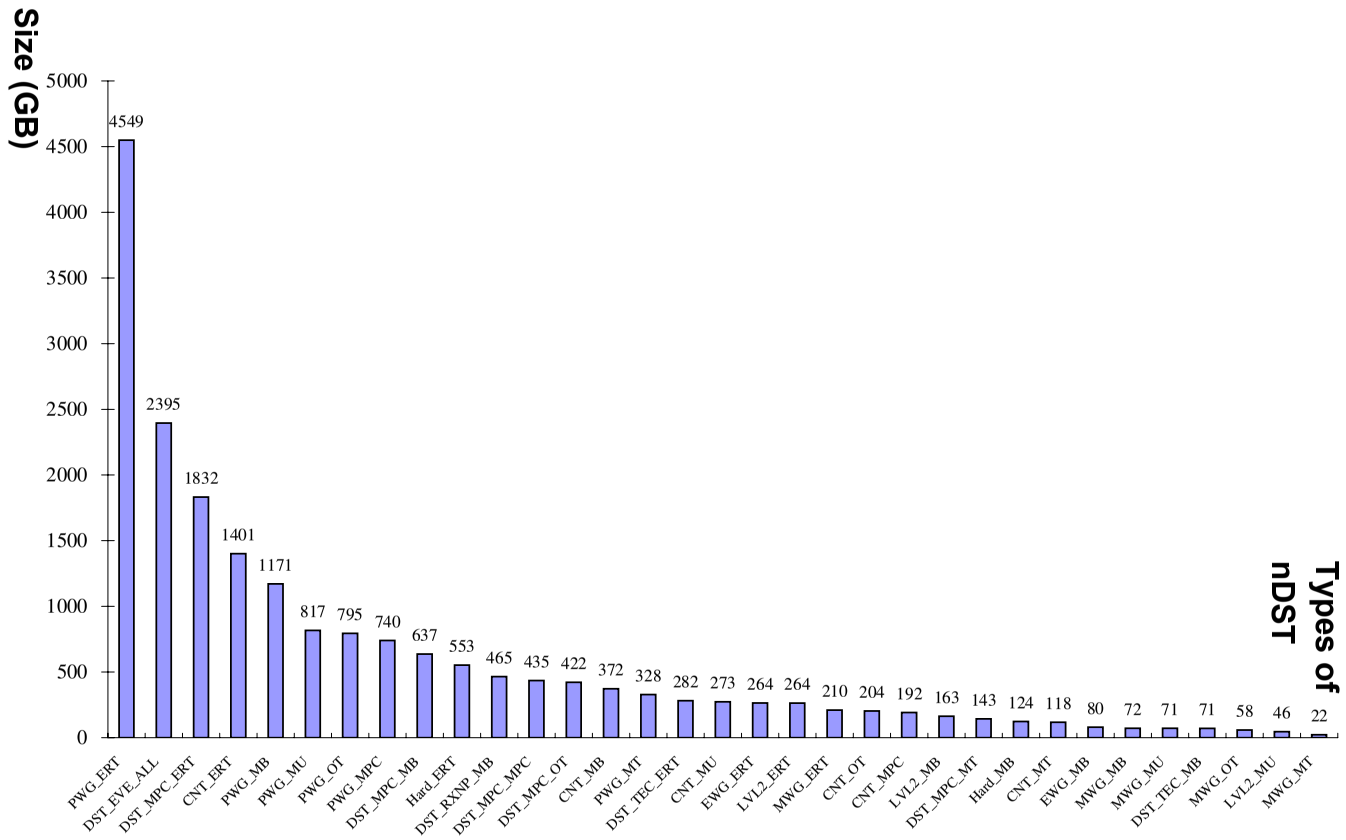

Figure 2.2: Flavors of nDSTs and their respective sizes in GB for run8 p+p data.

250 MB/s throughput. A new high performance network storage system ("BlueArc") is currently being introduced to the experiment for extended storage and higher reliability. All above-mentioned systems are connected through high performance switches which are also being upgraded to achieve better performance and high scalability. The entire RACF facility is managed by 37 staff members, from whom the PHENIX experiment received strong technical support year-round.

2.3.2 Computing Center in Japan

The Computing Center in Japan (CCJ) was planned in 1998 and under construction from 1999 to 2002 at RIKEN [48]. It serves as a regional computing center in Asia for the PHENIX experiment, and plays an important role in spin physics analysis. The Linux computing farm at CCJ consists of 188 CPUs that can run jobs via the LSF (Load Sharing Facility) batch queue software. 256 more CPUs with higher speed from RIKEN Super Combined Cluster System (RSCC, consisted of 2048 CPUs [49]) were added later on. After RSCC's decommission in 2009, it was replaced by 256 CPUs from RIKEN Integrated Cluster of Clusters (RICC, consists of 8192 CPUs [50]). An HPSS was also deployed as mass storage system at CCJ, capable of 400 TB storage and 300 MB/s transfer speed. In addition, a number of SUN data servers host the NFS file system, accounting for approximately 100 TB disk space. And all systems were connected via 1 Gbps LAN, but upgraded later on to 10 Gbps LAN.

Four GridFTP servers ("ccjboxes"), each with 9 TB storage, act as temporary buffers for data transfer between RCF and CCJ. Some firewall bypass are allowed for the ccjboxes to optimize transfer rate from/to remote sites.

The overall layout of CCJ is shown in Fig. 2.3.

As a remote site, the computing environment at CCJ needs to be replicated from RCF. CCJ job nodes run identical operating system as the ones at RCF. The database content and latest software at the PHENIX experiment are packaged and restored at CCJ on a daily basis. Those activities

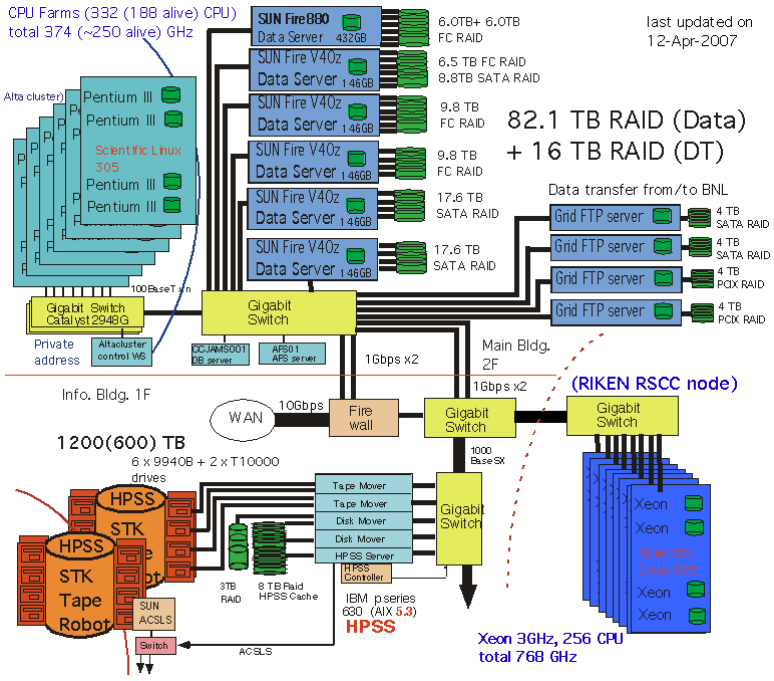

Figure 2.3: A schematic overview of hardware configuration at CCJ.

guarantee identical results for physics analysis carried out at both sites.

2.3.3 Data Production at CCJ and RCF

PHENIX run5, run6, and run8 p+p 200 GeV data were processed at CCJ while run9 data were processed at RCF. Such arrangement was mainly driven by the hardware upgrade schedules for the two sites.

Table 2.1 shows a summary of run8 and run9 p+p data production. The difference in raw data files sizes listed here and the ones listed in the next section comes from files that were lost due to broken tapes, disk malfunctioning and sometimes operator errors during data taking at the experiment.

As raw data files arrived at the disks of grid servers at CCJ (data transfer are discussed in the next section), they were copied to CCJ's HPSS system. A typical production job starts by staging the data file to local disk of the job node. Then the MD5 checksum is calculated for each file in order to avoid file corruption caused by transmission errors or a broken tape. Processing of the

Dataset	run8 200 GeV	run9 500 GeV	run9 200 GeV
Location	CCJ	RCF	RCF
Events (billion)	3.50	3.44	9.73
File size (TB)	131	173	415
Number of runs	313	306	907
Time	100 days	14 days	25 days
Events produced (billion)	2.56	3.39	9.56
Runs produced	295	278	871

Table 2.1: Summary of data production for run8 and run9.

raw data files then follows, 2 raw data files (5 GB each) usually take 10 hours to process on RSCC job nodes. Aggregation starts once all segments in a run are reconstructed. Although aggregation is not a CPU-intensive task, the number of aggregation jobs is limited by disk I/O because the produced files are distributed to only four disks. The aggregated files are then transferred to RCF with tools described in the previous section. Once the files are in dCache, they become available for physics analysis.

As an example, Fig. 2.4 shows the progress of the PHENIX run8 p+p data production at CCJ from September to December in 2008. From top to bottom, the four plots are:

1. Total size of raw data files that had been processed in GB. More than 90% of the raw data were processed in three months' time.

2. The solid line shows the number of production jobs running and the green shade shows the number of all jobs (including those waiting) in the queue. There were typically 100 jobs running in the RSCC queue.

3. Reconstruction speed in Bytes/s, this was calculated by summing raw data file sizes processed in the past 24 hours. A speed at 15 to 30 MB/s was kept.

4. Number of files transferred to RCF. The transfer to RCF were carried

out almost in real time.

For the PHENIX run9 p+p data production at RCF from July to September in 2009, Figures 2.5 and 2.6 show the progress of data production of the 500 GeV dataset and the 200 GeV dataset respectively.

Compared to production at CCJ, the one at RCF has a much larger resource of CPUs (1000 vs. 100 at CCJ). For example, as many as 800 jobs could run at the same time, this therefore reduced the processing time at RCF significantly. However, increasing the speed even further was not possible since the number of reconstruction jobs are limited by the throughput of the HPSS system.

Since the produced files are stored on a single disk at RCF, Aggregation jobs at RCF are limited by disk I/O as were at CCJ. Typically the number of aggregation jobs that could run at the same time has been throttled to 70.

The aggregated nDSTs are then transferred to dCache thus became ready for physics analysis. A small fraction of the files are also staged to disk, enabling quick check of code or calibrations on real data.

2.3.4 Data Transfer

Since 2005, the PHENIX experiment started to transfer raw data from the experimental hall (1008) to CCJ at RIKEN in real time during data taking for p+p collisions. Therefore data production could follow at CCJ without exhaustion of computing resources at RCF and allow quick physics analysis for polarized p+p datasets.

The data transfers took advantage of BNL's high speed connection to ESNET which has a transpacific line to Japan's SINET [51]. Except for a couple of network outages at ESNET, the transfer itself was not interrupted. The typical transfer rate was at 70 MB/s consistently. The lower average rates shown in Table 2.2 simply reflect pauses in data taking at the PHENIX experiment. As an example, Fig. 2.7 and 2.8 show daily progress of the data transfer in 2008.

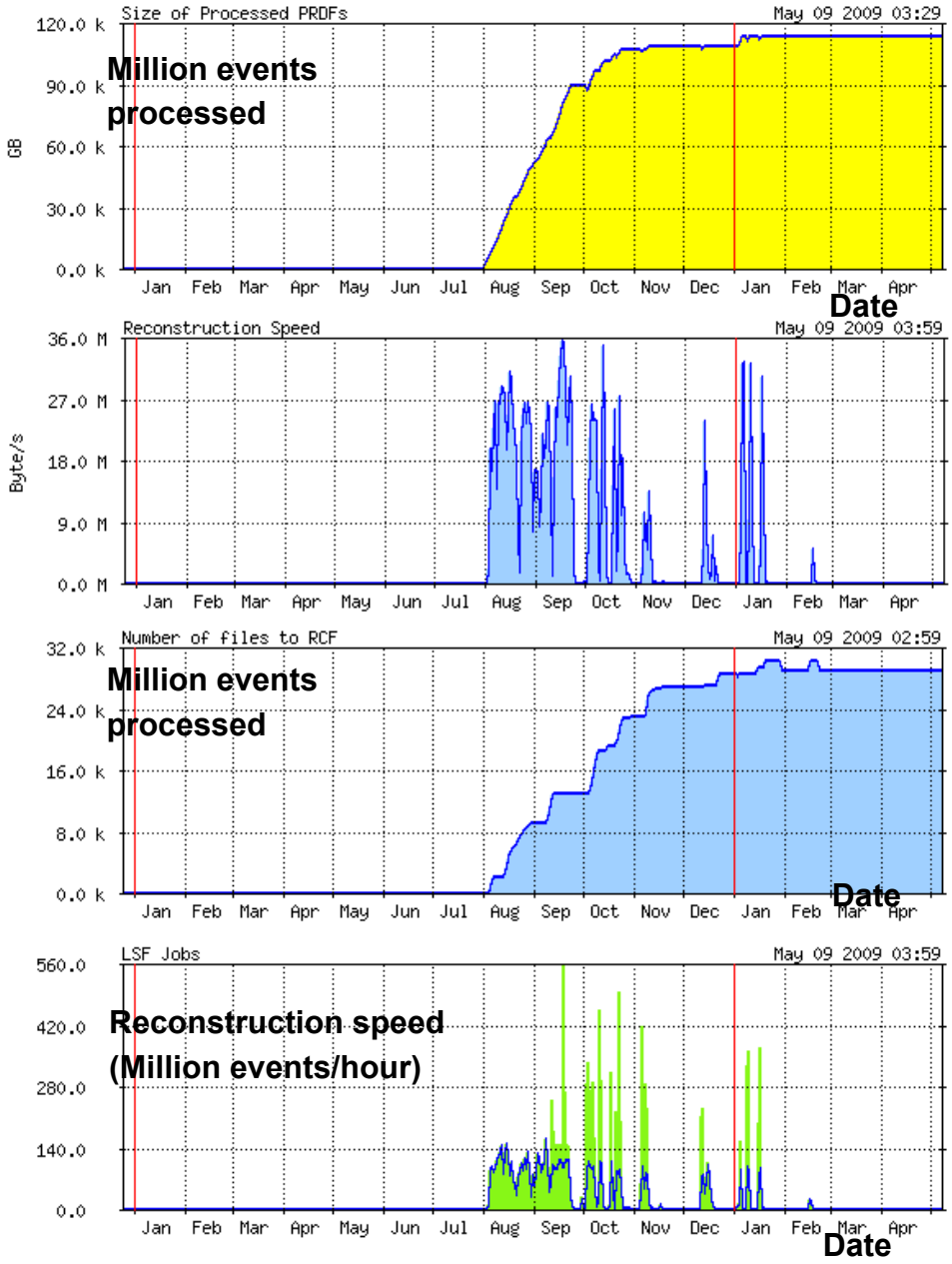

Figure 2.4: Run8 data production progress at CCJ. The four plots correspond to the following quantities vs time(from top to bottom): 1) produced file size, 2) number of production jobs, 3) production speed 4) number of files transferred to RCF.

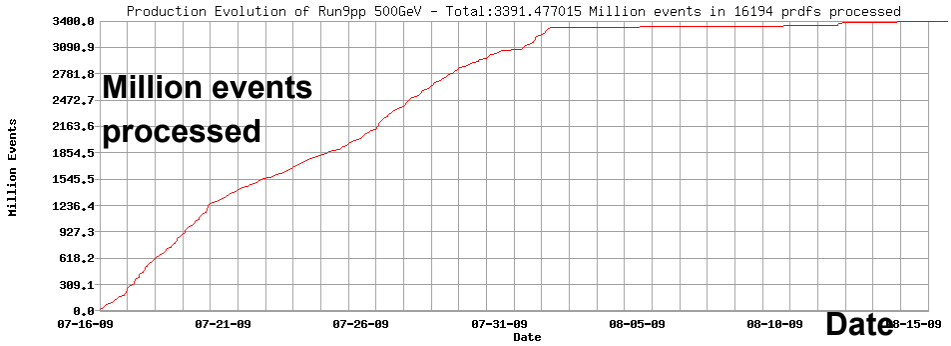

Figure 2.5: Progress of run9 data production for the 500 GeV dataset at RCF. It shows the number of one million events processed as a function of time.

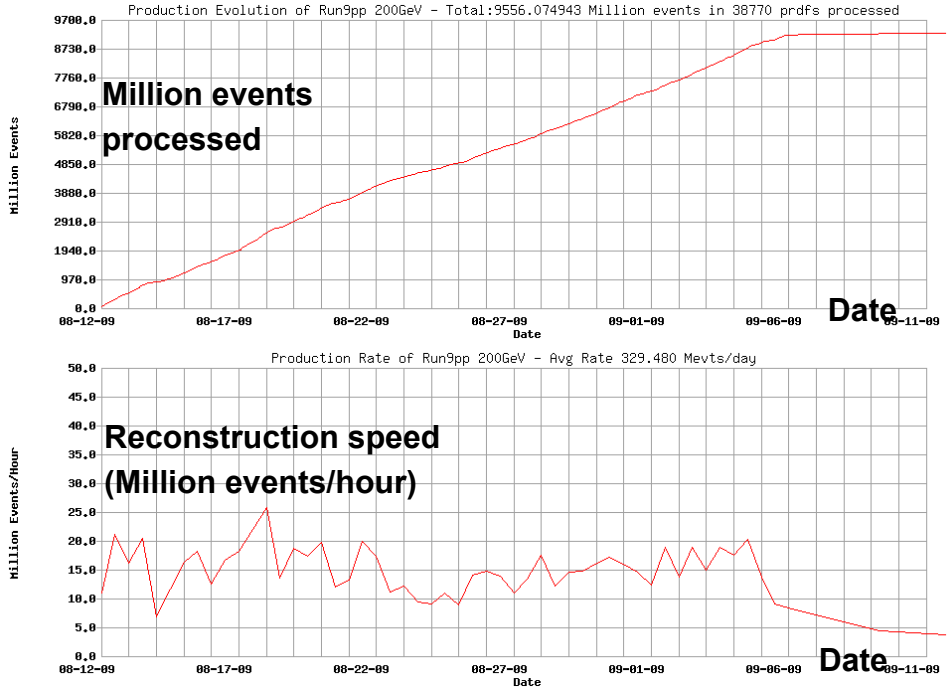

Figure 2.6: Progress for run9 data production for the 200 GeV dataset at RCF. Top plot shows the number of one million events processed as a function of time. Bottom plot shows the production speed in millions events per hours as a function of time.

Compared to previous years, the transfer rate in 2008 has been improved mainly because a LAN (Local Area Network) upgrade at CCJ to 10 Gbps and the fact that transferred data could bypass the firewall. A peak rate at 340 MB/s was achieved during the initial test, limited by the firewall at BNL.

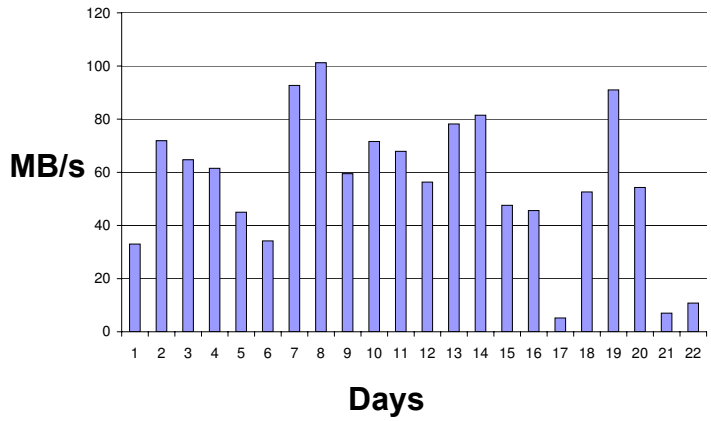

Figure 2.7: Daily average of transfer speed during run8 p+p data taking from the PHENIX experiment (1008) to CCJ. The horizontal axis is the number of days since February 19th, 2008.

In addition to the transfer of raw data files, the produced nDSTs were transferred between CCJ and RCF in real time as they were produced in 2008 and 2009. A transfer speed of 100 MB/s was achieved and approximately 100 TB of nDSTs from run9 data were sent from RCF to CCJ. For run8 nDSTs, 20 TB files traveled the reverse route from CCJ to RCF.

All transfers mentioned above were carried out with GridFTP rather than the older bbFTP [52]. The GridFTP utility is part of the globus toolkit software package [53].

To prepare for the transfer, a proper TCP buffer size needs to be chosen in order to optimize the speed. The following can be used to calculate the

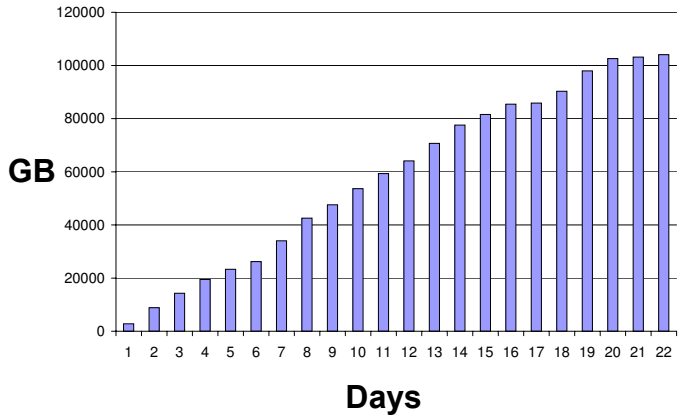

Figure 2.8: Vertical axis: the total amount of transferred run8 p+p data in GB from the PHENIX experiment (1008) to CCJ. Horizontal axis: number of days since February 19th, 2008.

buffer size s:

$$s = b \times t \tag{2.1}$$

where b is the bandwidth and t is the round-trip time between two sites. The transfer of raw data from the PHENIX experiment hall (1008) to CCJ uses a buffer size of 4 MB.

In case of the transfer of nDSTs between RCF at BNL and CCJ at RIKEN, $b = 100$ Mbps (upper limit of NFS file system on the sFTP servers at RCF), $t = 50$ ms and 10 files being transferred at the same time, therefore the buffer size was set to 2.5 MB. Additionally, certain level of parallelism also boost the transfer speed, however studies have shown that the speed is stable once the number of parallel streams reaches 5 and decreases slightly at above 15 [53].

On the CCJ side, files were sent/received on the four grid servers mentioned in the previous section. On the RCF side, incoming files went through the three dCache servers (the "doors") while the outgoing files were sent from the two sFTP servers that have access to networks outside BNL.

In summary, Table 2.2 shows file transfer rate achieved 2005, 2006 and 2008.

Dataset	run5	run6	run8
File size (TB)	263	308	104
Time (days)	80	110	22
Average rate (MB/s)	40	34	54
Peak rate (MB/s)	74	70	100

Table 2.2: Summary of data transfers in run5, run6 and run8.

Chapter 3

Data Analysis

This chapter describes the procedure of data analysis. It starts with calibrations, then proceeds with data selection, and finally the calculation of single spin asymmetries of particle pair produced in polarized proton-proton collisions.

3.1 Calibrations

3.1.1 A Warnmap for EMCal

"Hot" or "dead" towers in EMCal have exceptionally high or low hit rates compared to average values, they are usually caused by hardware malfunctioning and should not be used for physics data analysis. A warnmap is used to mask "hot" or "dead" towers. It's produced with the following procedure:

The hits in each EMCal tower are summed up for all runs. For a given tower and certain energy range (1 GeV bins from 1 to 10 GeV, plus a low energy bin from 0.1 GeV to 1 GeV in PbSc and 0.2 GeV to 1 GeV in PbGl), the tower is declared hot if the number of hits exceeds the mean of the hit distribution by 10 times the RMS of the distribution. A tower is declared dead if number of hits are lower than the mean by 5 times the RMS. Those towers are removed and the mean and RMS is calculated again to check if there is any new dead/hot towers. The iteration continues until no more

hot/dead towers are found.

Neighboring tower of hot/dead towers are included in the warnmap since an electromagnetic shower centered on that tower might include a hot/dead tower.

In addition to hot and dead towers, the warnmap also includes towers that failed the initial energy calibration. A list of such towers can be found in Ref. [54].

The warnmap used in this analysis is shown in Fig. 3.1. Table 3.1 and Table 3.2 lists the number of towers that have been masked.

Sector	Masked towers	Total
W0	523 (20%)	2592
W1	469 (18%)	2592
W2	517 (20%)	2592
W3	703 (27%)	2592
E0	1338 (29%)	4608
E1	1195 (25%)	4608
E2	703 (27%)	2592
E3	651 (25%)	2592

Table 3.1: Numbers of towers that have been masked in each sector of EMCal from Run6 data.

3.1.2 Energy Scale for EMCal

The run-by-run energy scale is not included in the Master Recalibrator for Run8 data. To obtain the correction, the π^0 mass is plotted for each run. The mass spectra are then used to scale π^0 mass to 137 MeV/c^2, which is the center value of the mass window to select π^0 from di-photon invariant mass spectra.

Sector	Masked towers	Total
W0	512 (20%)	2592
W1	498 (19%)	2592
W2	672 (26%)	2592
W3	789 (30%)	2592
E0	1236 (27%)	4608
E1	923 (20%)	4608
E2	626 (24%)	2592
E3	502 (19%)	2592

Table 3.2: Numbers of towers that have been masked out in each sector of EMCal from Run8 data.

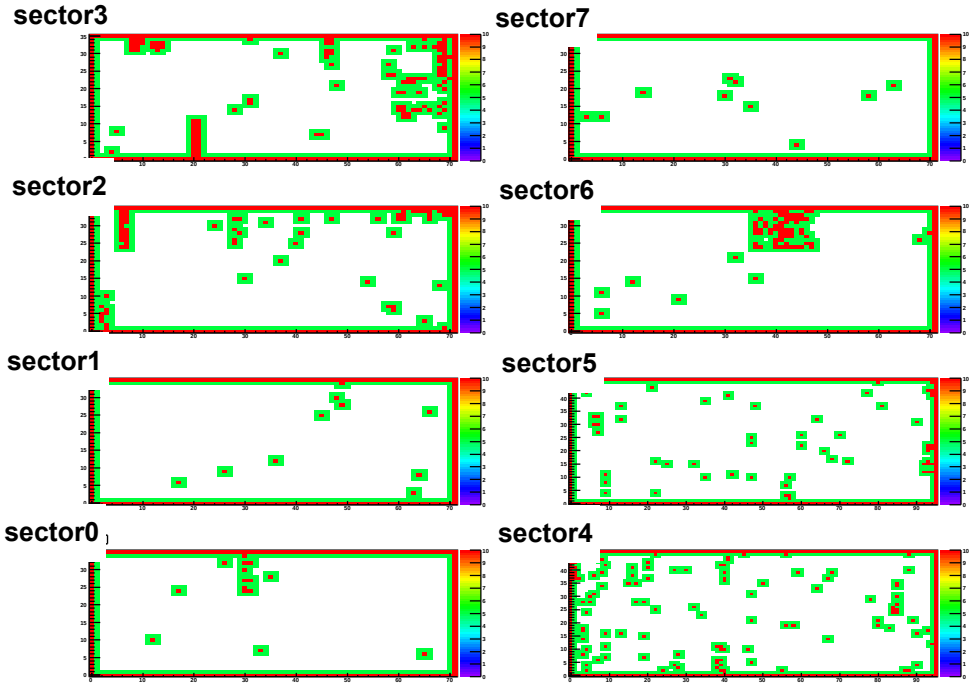

Figure 3.1: EMCal warnmap used for π^0 in Run8 analysis. Red indicates towers that are hot/dead or failed tower-by-tower calibration.

The run-by-run dependence of the π^0 mass, width and signal to background ratio are shown in Figs. 3.2-3.7. Time dependent calibration factors are found to correct for the run dependence of the energy calibration. The EMCal calibration factors are store in a database and applied the data analysis to correct measured π^0 mass to the actual physical level.

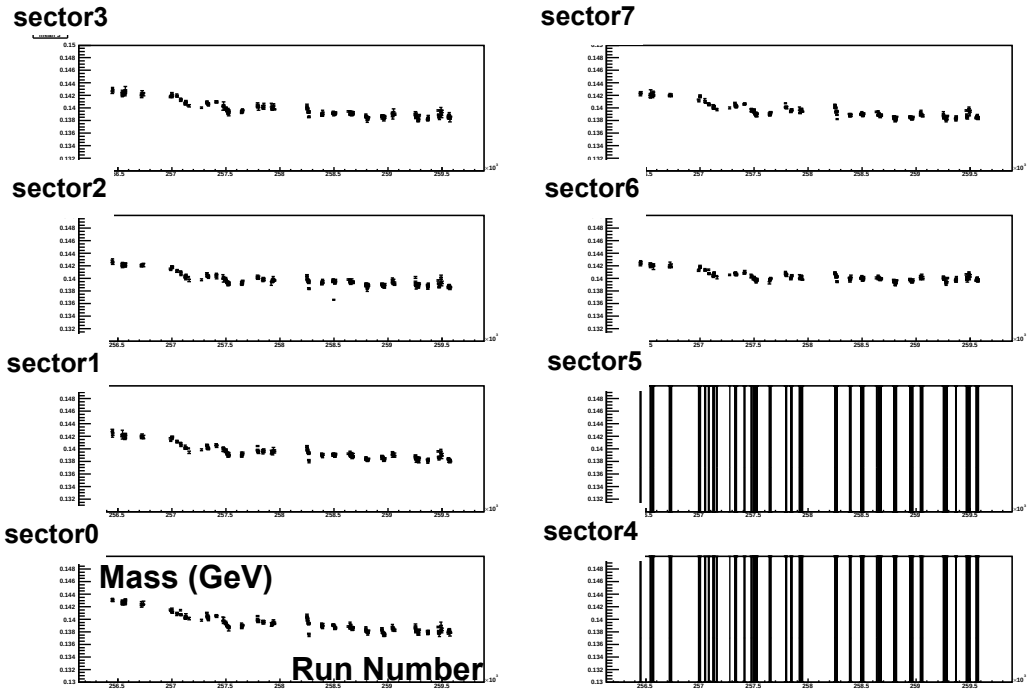

Figure 3.2: Run dependence of π^0 mass from Run8 data. (4x4c triggers, note that PbGl was masked off during run8)

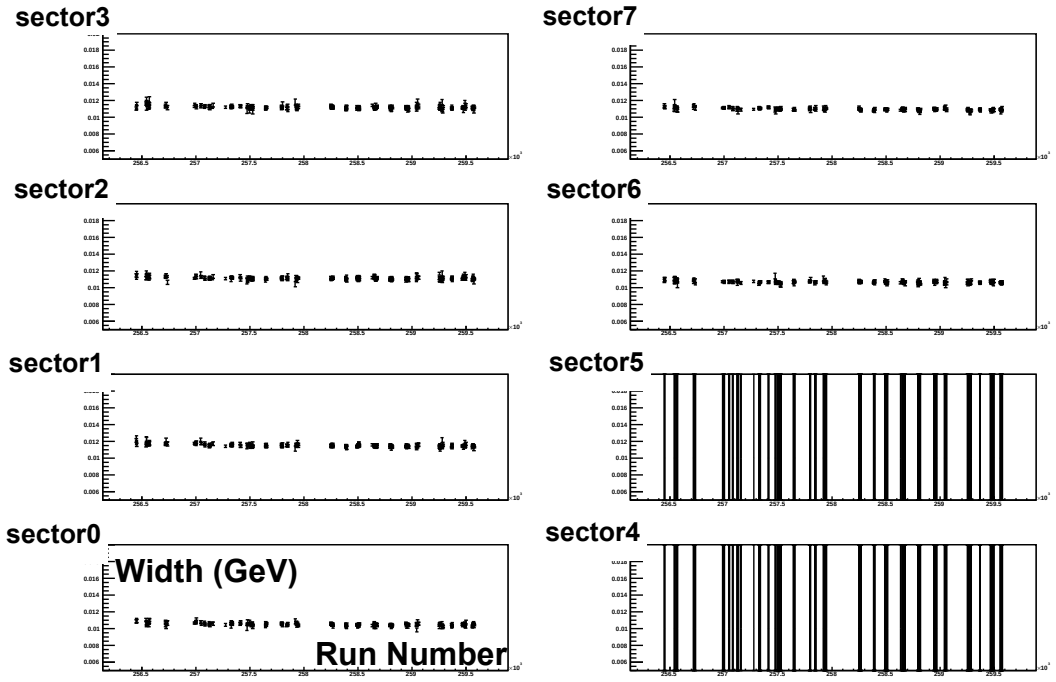

Figure 3.3: Run dependence of π^0 width from Run8 data. (4x4c triggers, note that PbGl was masked off during run8)

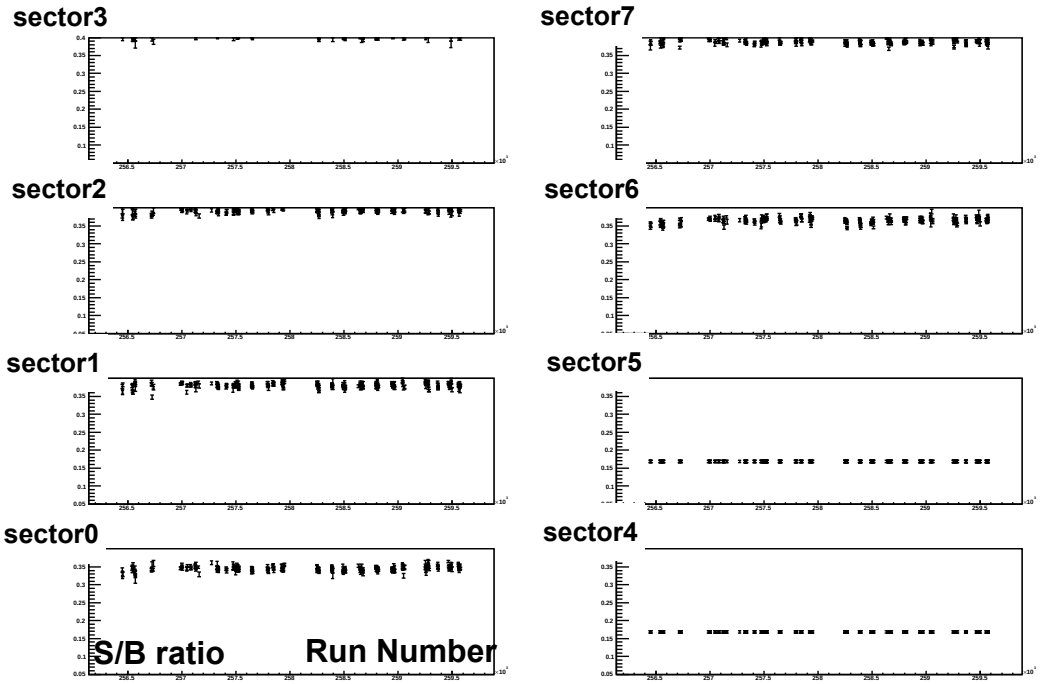

Figure 3.4: Run dependence of π^0 signal to background ratio from Run8 data. (4x4c triggers, note that PbGl was masked off during run8)

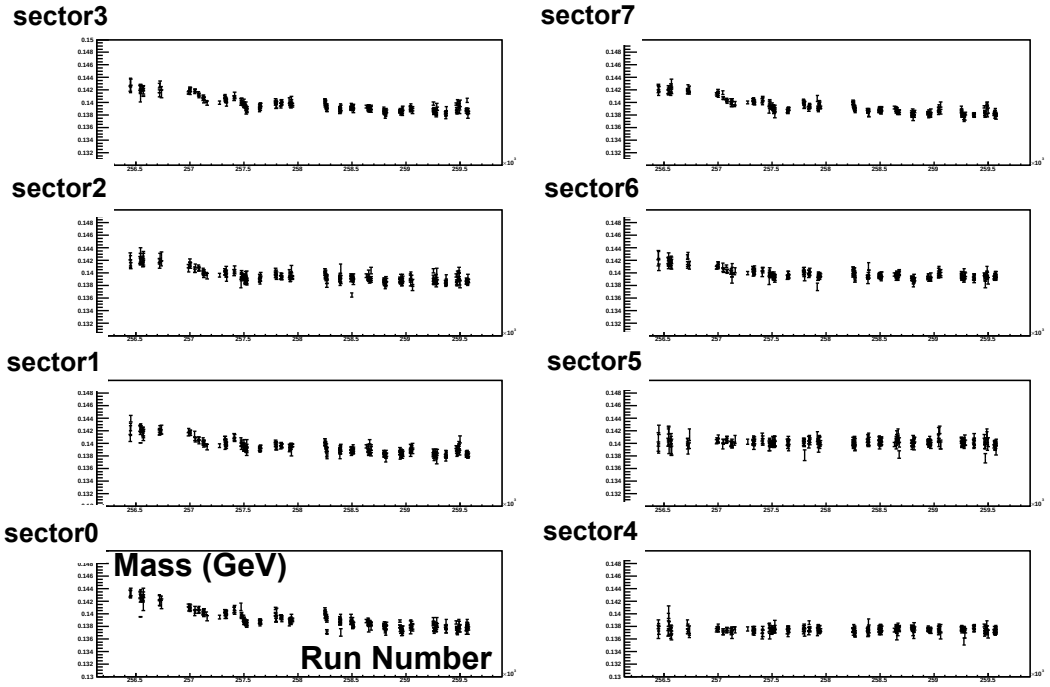

Figure 3.5: Run dependence of π^0 mass from Run8 data. (4x4a triggers)

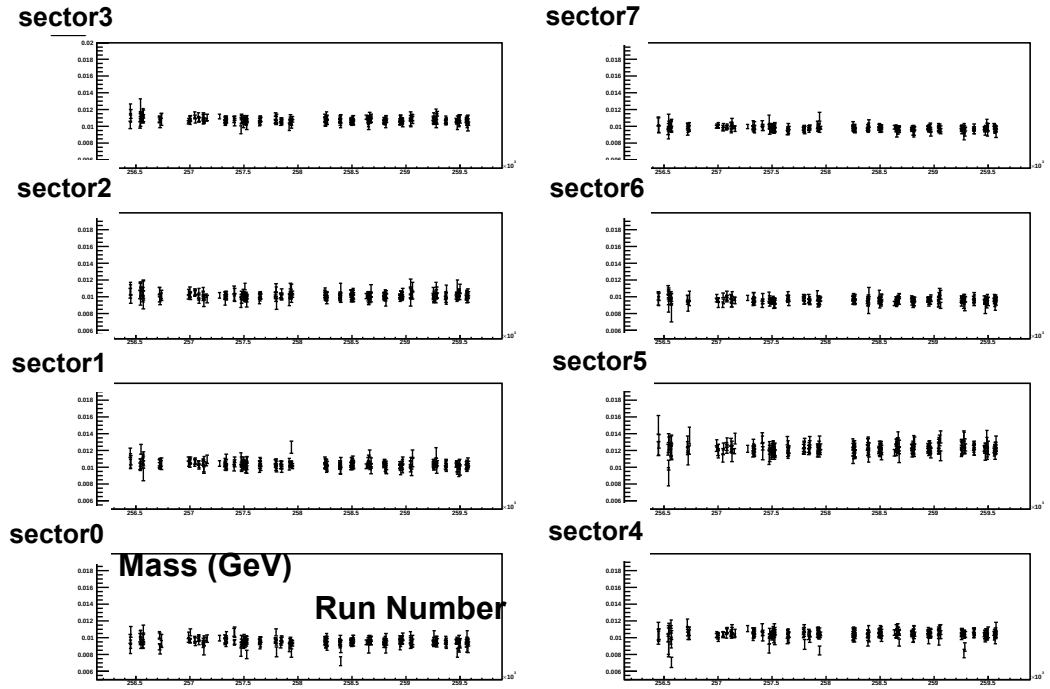

Figure 3.6: Run dependence of π^0 width from Run8 data. (4x4a triggers)

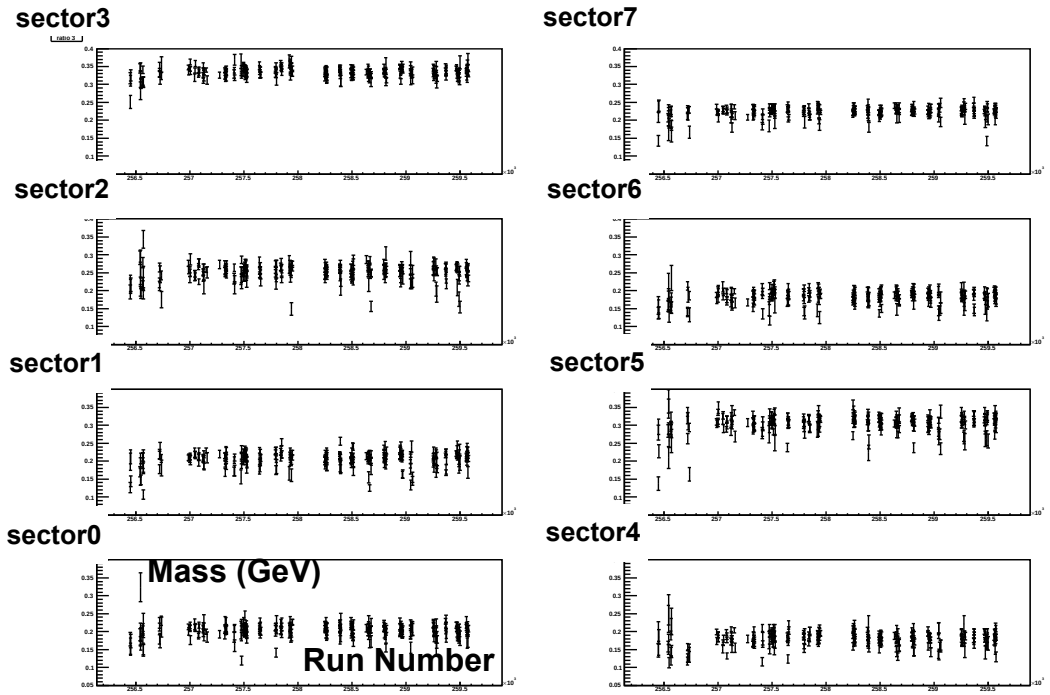

Figure 3.7: Run dependence of π^0 signal to background ratio from Run8 data. (4x4a triggers)

3.1.3 Beam Offset and Momentum Scale for Charged Tracks

Momentum of charged particles are measured with Drift Chambers (DC) at PHENIX. Ref. [55] describes various calibrations for the DC.

Due to detector alignment and accelerator running condition, the center of the collisions are not at $x = y = 0$ in the plain perpendicular to the beam. A beam offset (Δx, Δy) can lead to a correction to α:

$$\Delta\alpha = \frac{\Delta x \sin\phi}{R} + \frac{\Delta y \cos\phi}{R} \tag{3.1}$$

where the average DC radius was taken as R=220 cm. The exact definition of α, ϕ can be found in Refs. [56] [57]. The angle α is basically the inclination of the track at the point where a reference plane at radius of R intersects with the track. Fig. 3.8 illustrates the definitions of those two angles, they are used to calculate momenta of charged tracks.

To apply the beam offset to real data, the α value is retrieved for a given track, then it's corrected to $\alpha' = \alpha + \Delta\alpha$ using Eq. 3.1. The new p_T is calculated as $p'_T = p_T|\frac{\alpha}{\alpha'}|$. Since this correction is only applied in the $r - \phi$ plane, p_Z remains unchanged.

The method to extract beam offsets from zero field runs is described in Ref. [58]. It starts with plotting the correlation of ϕ and $\Delta\alpha$. The ϕ range of the tracks are divided into 80 slices for East and West arms respectively. For each slice, $\Delta\alpha$ is found by fitting the α distribution with a double gaussian function and taken as the mean from the narrower peak. Then the $\Delta\alpha - \phi$ relation curve is fitted with the function in Eq. 3.1 to obtain Δx and Δy.

During the 2008 p+p running, 6 zero field runs were taken: 257054, 257803, 258257, 258257, 258268, 258269. Only charged tracks with good DC hits are used for this analysis. $\Delta\alpha$ vs ϕ distributions from 4 runs are plotted in Figs. 3.9, 3.10, 3.11, 3.12, 3.13 and 3.14. The summary of all runs is shown in Fig. 3.15.

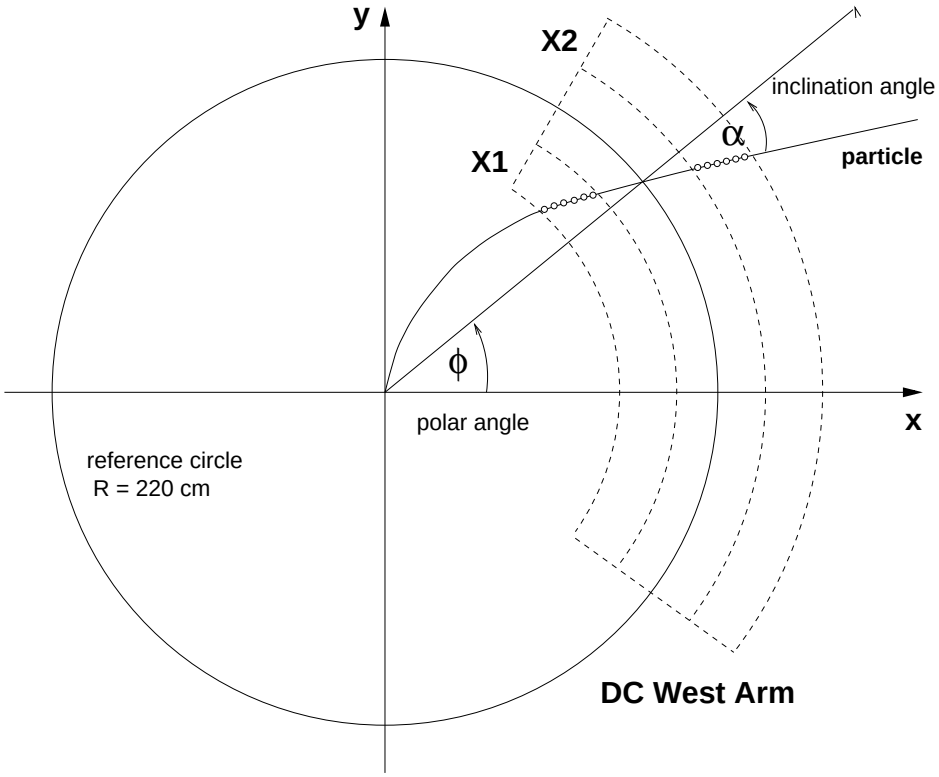

Figure 3.8: ϕ and α are shown for a sample track in the central arm in $x-y$ plane cut-away [57].

According to Ref. [59], the west carriage was moved on Feb 27, 2008. The last run before the move is 257954. The offset dx changed after this run for the west arm, but not for the east arm.

The $\Delta\alpha$ vs ϕ is plotted after the beam offset correction is applied as a cross check, as shown in Figs. 3.16, 3.17, 3.18, 3.19, 3.20.

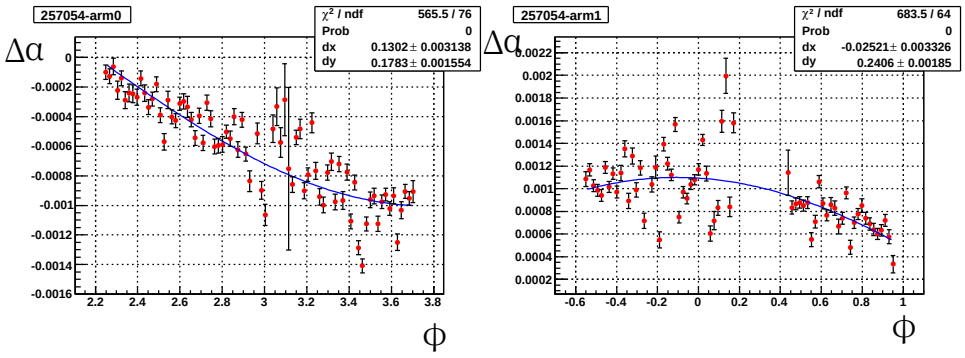

Figure 3.9: $\Delta\alpha$ vs ϕ distribution for run 257054. Left is for East arm, right is for West arm.

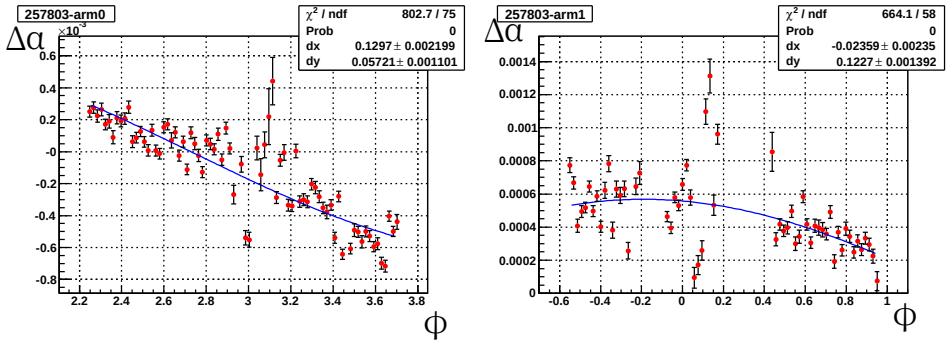

Figure 3.10: $\Delta\alpha$ vs ϕ distribution for run 257803. Left is for East arm, right is for West arm.

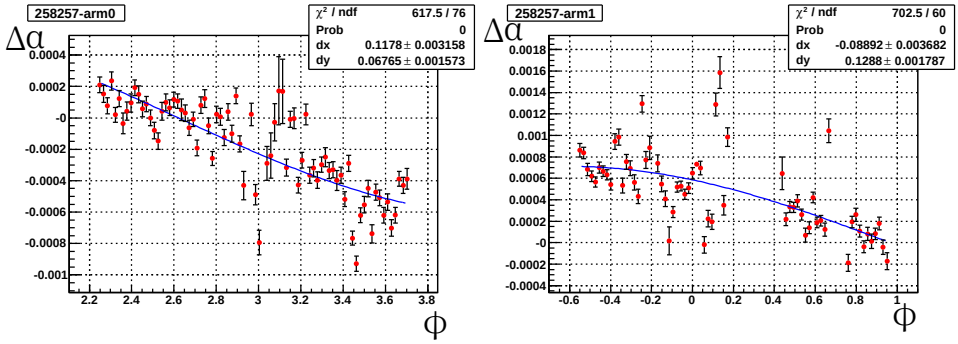

Figure 3.11: $\Delta\alpha$ vs ϕ distribution for run 258257. Left is for East arm, right is for West arm.

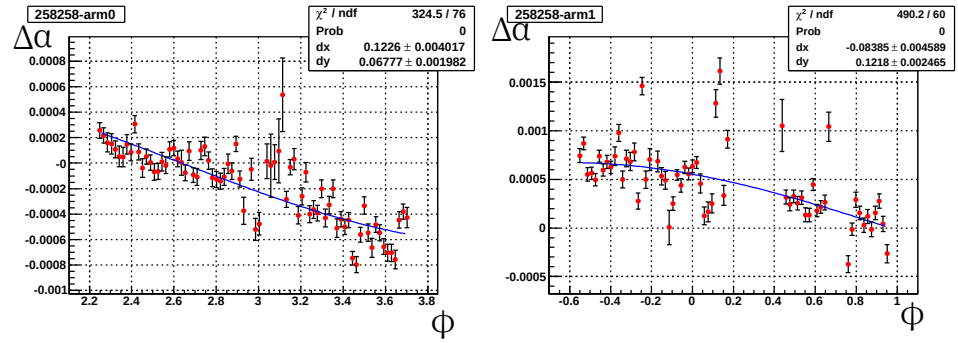

Figure 3.12: $\Delta\alpha$ vs ϕ distribution for run 258258. Left is for East arm, right is for West arm.

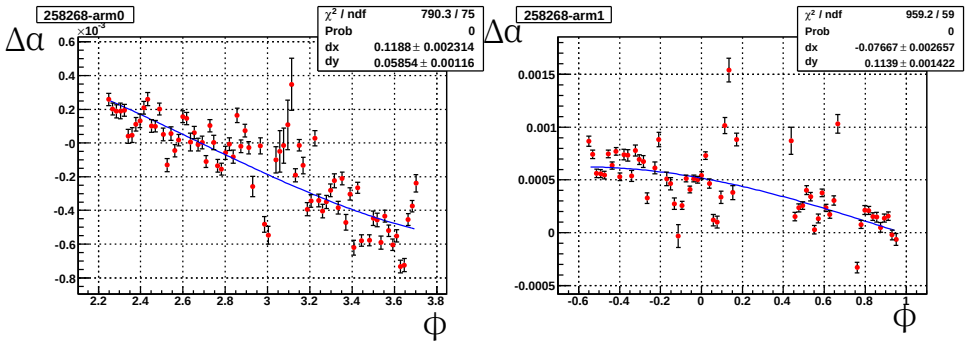

Figure 3.13: $\Delta\alpha$ vs ϕ distribution for run 258268. Left is for East arm, right is for West arm.

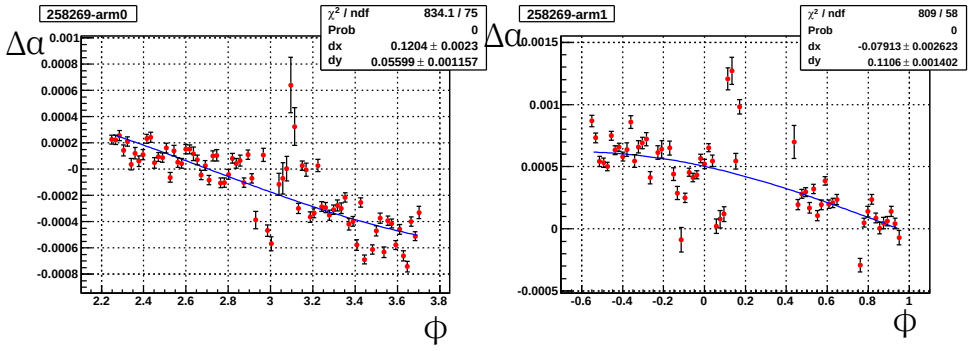

Figure 3.14: $\Delta\alpha$ vs ϕ distribution for run 258269. Left is for East arm, right is for West arm.

Run	Δx (East)	Δy (East)	Δx (West)	Δy (West)
257054	0.1302 ± 0.0031	0.1783 ± 0.0016	-0.0252 ± 0.0033	0.2406 ± 0.0019
257803	0.1297 ± 0.0022	0.0572 ± 0.0011	-0.0236 ± 0.0023	0.1227 ± 0.0014
258257	0.1178 ± 0.0032	0.0676 ± 0.0016	-0.0889 ± 0.0037	0.1288 ± 0.0018
258258	0.1226 ± 0.0040	0.0678 ± 0.0020	-0.0838 ± 0.0046	0.1218 ± 0.0025
258268	0.1188 ± 0.0023	0.0585 ± 0.0012	-0.0767 ± 0.0027	0.1139 ± 0.0014
258269	0.1204 ± 0.0023	0.0560 ± 0.0012	-0.0791 ± 0.0026	0.1106 ± 0.0014

Table 3.3: Beam offset for all 4 zero field runs (in centimeters).

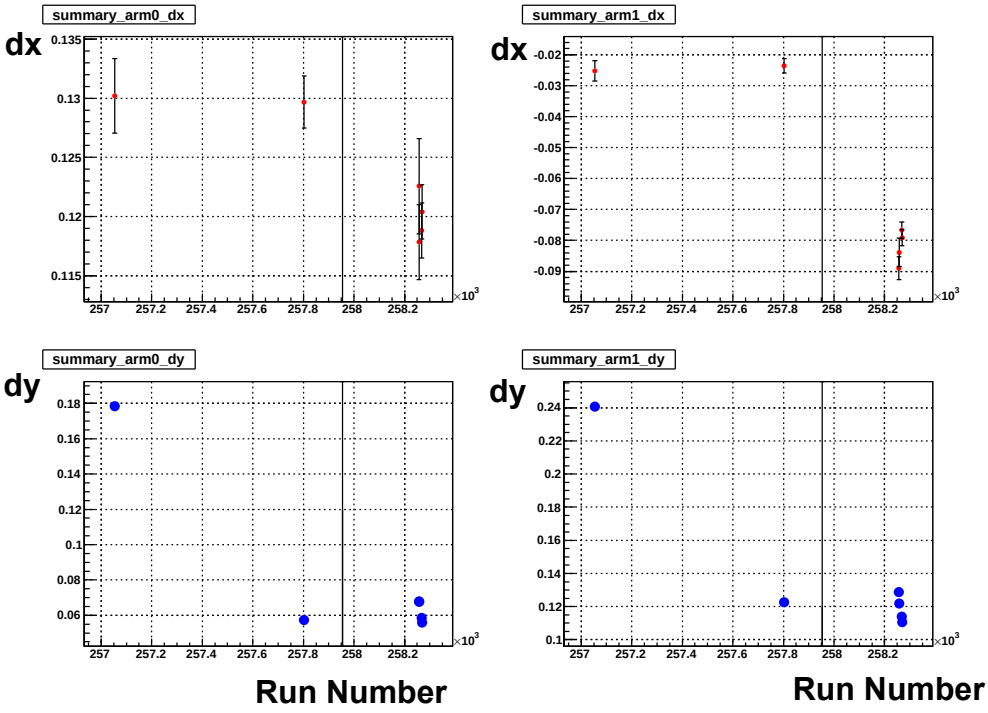

Figure 3.15: Δx and Δy for all 6 runs. Left is for East arm, right is for West arm. The solid line is at 257954 when West carriage was moved.

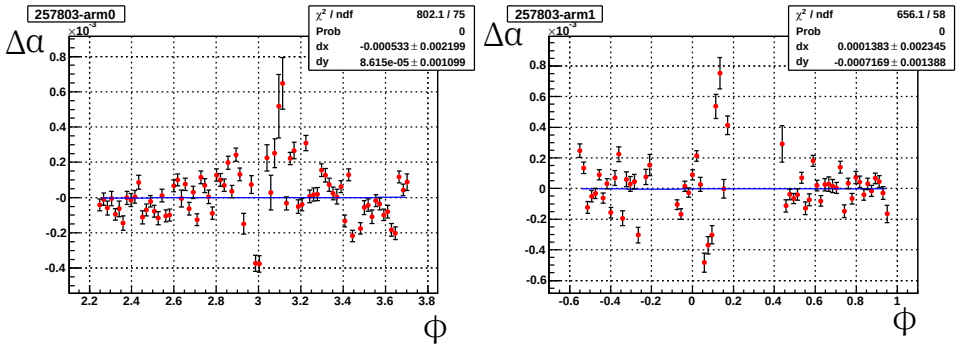

Figure 3.16: $\Delta\alpha$ vs ϕ distribution for run 257803. Left is for East arm, right is for West arm. (after correction)

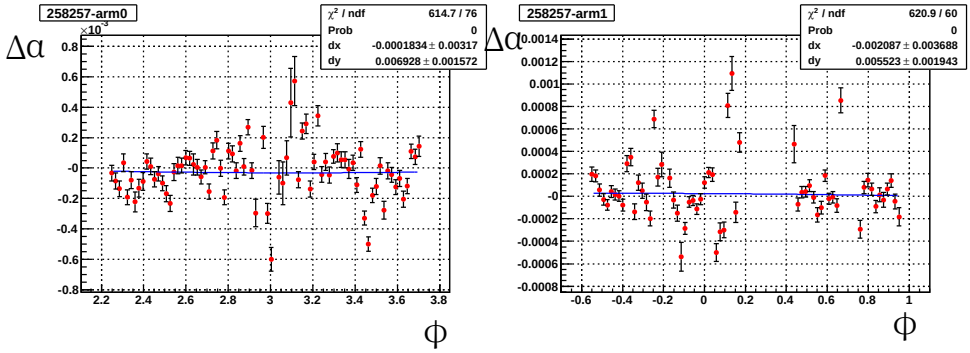

Figure 3.17: $\Delta\alpha$ vs ϕ distribution for run 258257. Left is for East arm, right is for West arm. (after correction)

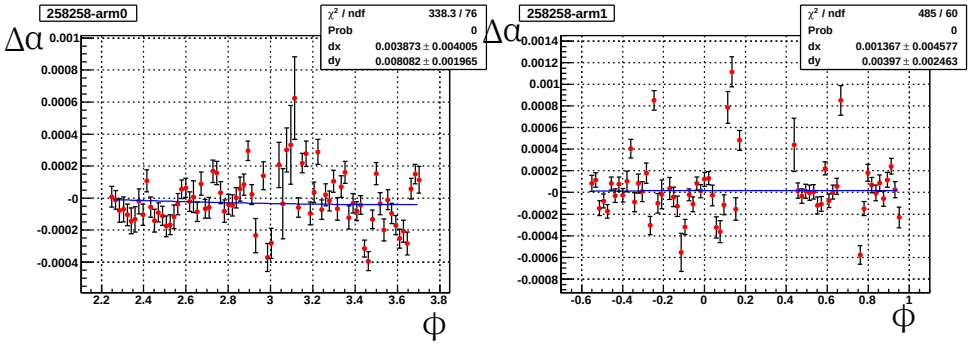

Figure 3.18: $\Delta\alpha$ vs ϕ distribution for run 258258. Left is for East arm, right is for West arm. (after correction)

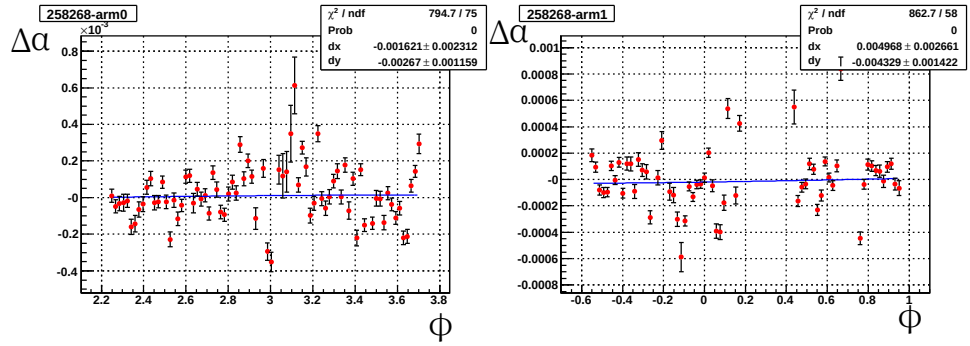

Figure 3.19: $\Delta\alpha$ vs ϕ distribution for run 258268. Left is for East arm, right is for West arm. (after correction)

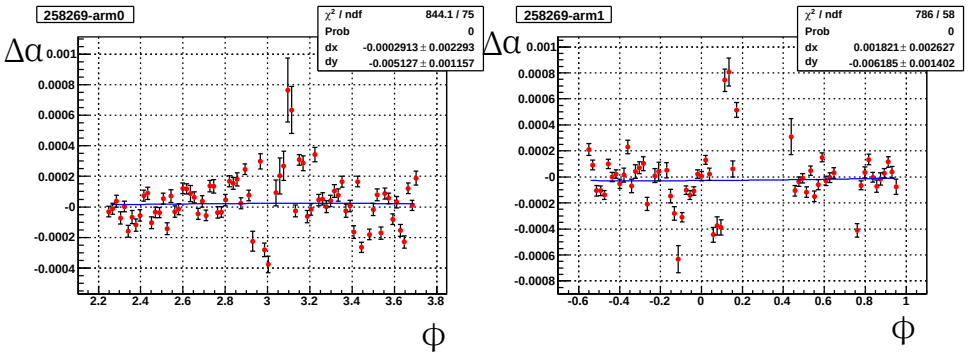

Figure 3.20: $\Delta\alpha$ vs ϕ distribution for run 258269. Left is for East arm, right is for West arm. (after correction)

With the help of the Time of Flight (TOF) detector, the proton mass can be used to obtain the momentum scale for charged tracks. Start from the time t measured in the TOF detector, the mass of a charged particle can be calculated as

$$m^2 = p^2[(ct/L)^2 - 1] \tag{3.2}$$

where c is speed of light, L is the path length to the TOF detector. Correlating time of flight and inverse momentum leads to clear identification of pions, kaons and protons as shown in Fig. 3.21, pions, kaons, and protons are clearly visible. The time t used here has been calibrated, general procedures for the TOF calibration can be found in Ref. [60].

Fig. 3.22 shows the mass squared distribution for protons and anti-protons, here only protons/anti-protons with momentum between 1 and 1.8 GeV/c are used. This can only be done after TOF calibration has been completed.

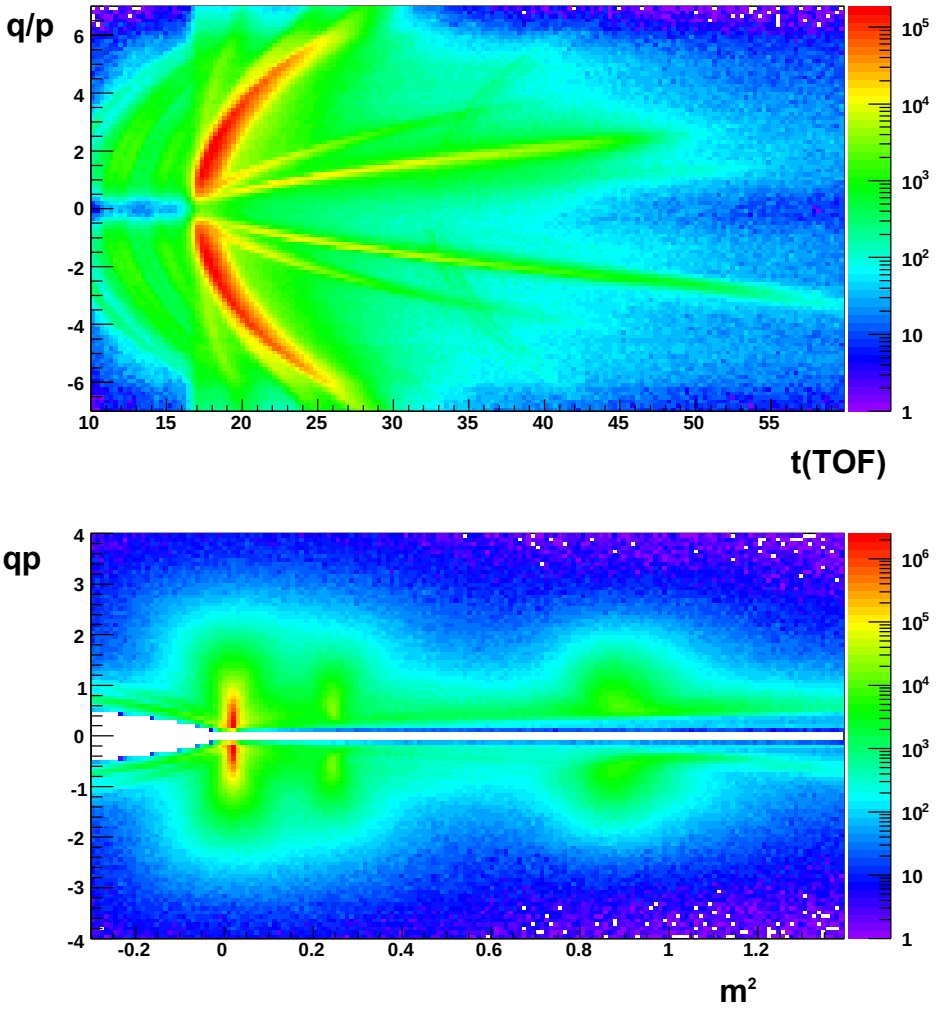

Figure 3.21: In the top plot, the horizontal axis is time measured in TOF East, the vertical axis is momentum divided by charge. In the bottom plot, the horizontal axis is the mass squared, the vertical axis is momentum times charge. Charged tracks with good DC hits and momentum between 1 GeV/c and 1.8 GeV/c are used.

The mass squared for proton and anti-proton mass are 0.946 and 0.940 GeV^2 from a gaussian. By comparing with PDG value, the momentum scale is

$$\sqrt{\frac{m_p^2}{m_p^2(PDG)}} = \sqrt{\frac{(0.946+0.940)/2}{0.880}} = 0.966 \tag{3.3}$$

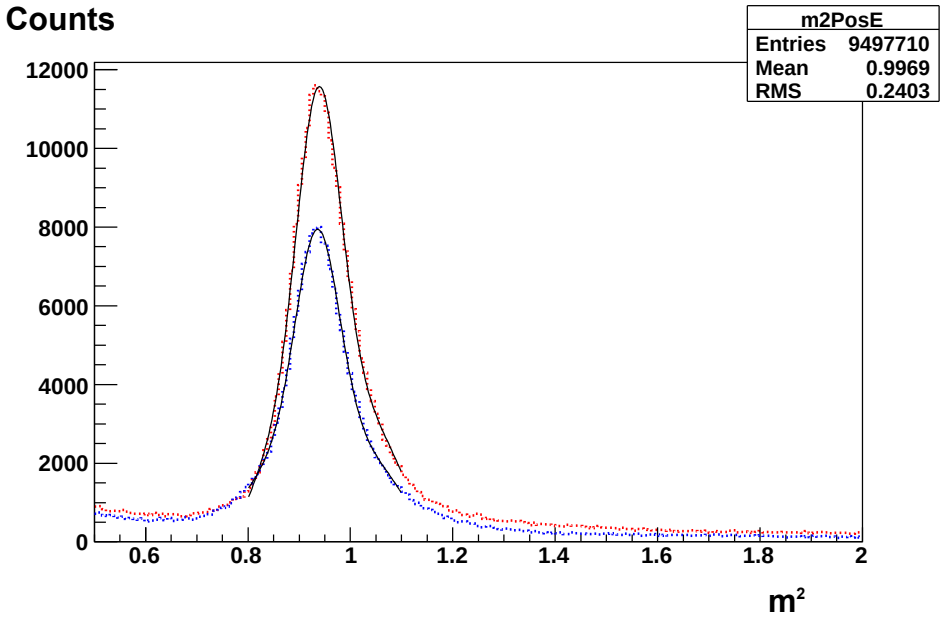

Figure 3.22: Mass squared distribution calculated using timing information from TOF for proton and anti-proton.

3.2 Data Selection, Polarization and Relative Luminosity

3.2.1 Data Selection

The analysis for run6 data uses ERT4x4c&BBCLL1 triggered proton-proton collision data taken in 2006 at $\sqrt{s} = 200$ GeV. The data was produced with pro.74 libraries at CCJ. Only the transverse runs are used, they are from run 189575 to run 197795.

Runs 190276, 190277, 190280, 190281, 190282, 190283, 190284 (fill 7621), 191299 are not used since those are zero field runs.

Runs 191922, 191923, 191924, 191925, 191927 are not used because the spin information (polarization, fill number) is not available from either the spin database or the spin monitor.

Runs before 190281 are not used due to the reset problem of the global level-1 trigger board (GL1) board.

The single spin asymmetry was calculated fill by fill. Fills 7646, 7699, 7710, 7711, 7777 are not used because of very low statistics. 40 fills in total are used for this analysis.

The integrated luminosity for the runs that have been selected for run6 analysis is 1.89 pb^{-1}.

The analysis for run8 data uses ERT4x4c&BBCLL1 ERT4x4a&BBCLL1 triggered proton-proton collision data taken in 2008 at $\sqrt{s} = 200$ GeV. The data was produced with pro.82 libraries at CCJ.

Physics runs are used (256450-259576) for this analysis.

Zero field runs 257054, 257803, 258257, 258258, 258268, 258268, 258269 are not used.

Runs 256724, 257413 257502, 257517, 257644, 257649, 258663, 258808, 258950, 259050, 259572 are not used because spin information (GL1p counts used for relative luminosity) cannot be found.

Runs 257411, 257412, 257414, which have no fill numbers, are not used.

The integrated luminosity for the runs that have been selected for run8 analysis is 4.4 pb^{-1}.

3.2.2 Beam Polarization

The polarization direction in the 2008 transverse running is vertical. CDEV feed accelerator parameters from RHIC to PHENIX, this information was used to determine the polarization orientation. When CDEV says "++", the polarization direction at PHENIX points downward with respect to the accelerator ring.

The polarization for each beam has been assumed to be constant for one fill. In this analysis the final polarization values from the RHIC polarimetry group for Run8 were used. The final polarization results are available at `http://www4.rcf.bnl.gov/~cnipol/pubdocs/Run08Offline/`. Beam polarization for each fill are shown in Fig. 3.23. The average polarizations for the transverse running in 2008 are 50% and 43% for blue and yellow beams.

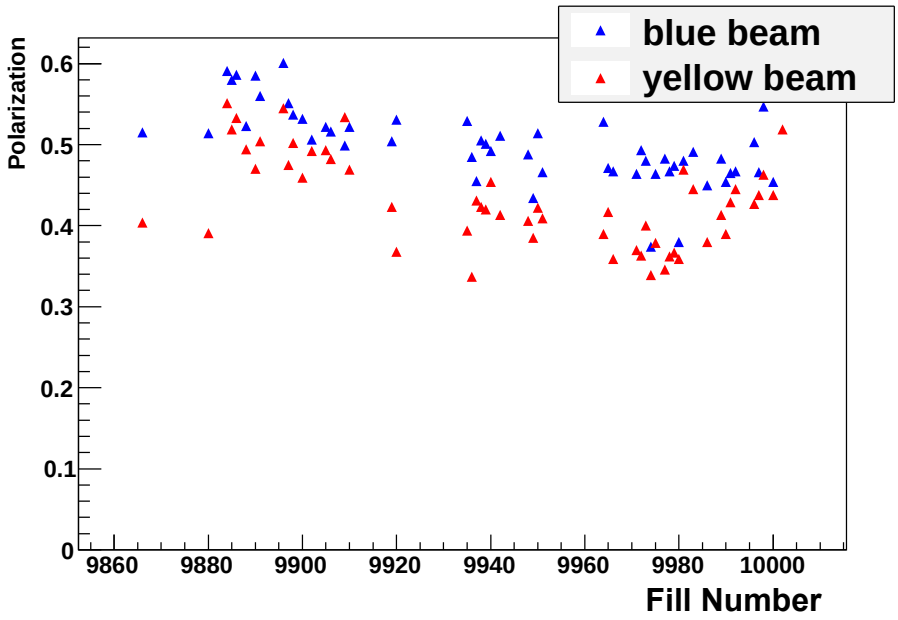

Figure 3.23: Final polarization values for 2008 transverse running.

3.2.3 Relative Luminosity

The relative luminosity is calculated for each fill by taking the ratio of the BBCLL1 triggered events for two different polarization states. The luminosity monitors in PHENIX are implemented by custom made scaler boards, the so called GL1p boards. The GL1p board can count up to 4 luminosity counters independently for each of the 120 bunch crossings. The GL1p luminosity scaler information is used to determine the relative luminosity between different groups of bunch crossings (eg. spin orientations). The results from

the relative luminosity analysis are stored in the PHENIX spin data base.

Since this is a single spin asymmetry analysis, the relative luminosity is calculated for both beams. Figure 3.24 shows the relative luminosities for blue and yellow beams calculated for each fill.

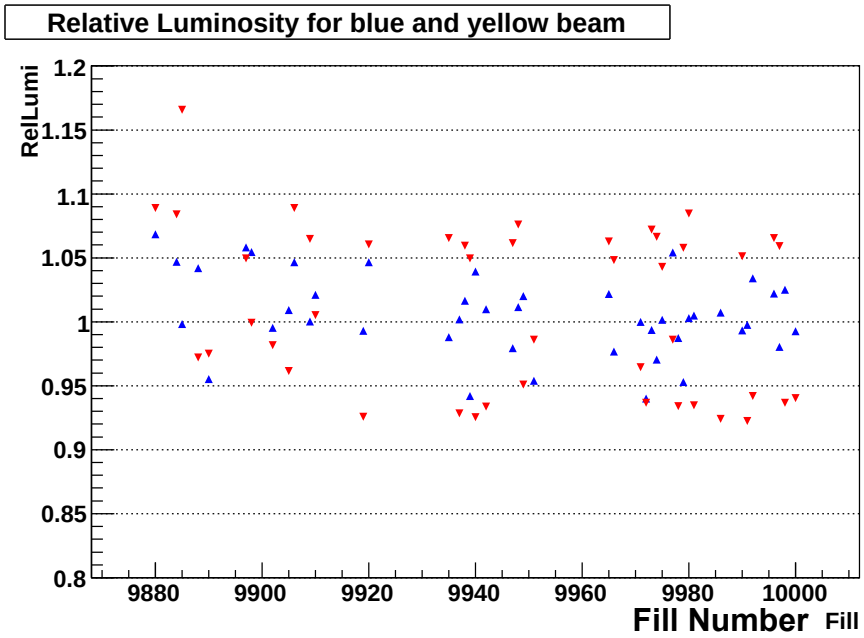

Figure 3.24: Relative luminosities for blue and yellow beams.

We choose three different combinations of hadron pairs for this analysis: $\pi^0 h^+$, $\pi^0 h^-$ and $h^+ h^-$.

When selecting events, a cut on the offline value of the z vertex has been made: $|z_{BBC}| < 30$ cm.

3.2.4 Reconstruction of π^0

π^0 are reconstructed from photon clusters found in the EMCal. The following cuts are used to select the photons:

- each photon passes the warnmap cut
- each photon passes minimum energy cut, 0.1 (0.2) GeV for PbSc (PbGl)

- each photon has a shower profile that has greater than 0.02 probability to be from electromagnetic shower
- two photon energy asymmetry $|e_1 - e_2|/(e_1 + e_2) < 0.8$
- the photon with higher energy fires the corresponding ERT trigger tile
- di-photon pair's $p_T > 1$ GeV/c

The tower-by-tower energy calibration was applied automatically from the Master Recalibrator as discussed in the previous section "Energy scale for EMCal" in Chapter 2. In addition to those calibrations, a non-linear function is applied to the calibrated cluster energy, for the PbSc sections of the EMCal

$$E_{final} = \frac{E_{calib}}{1.003 - 0.01/E_{calib}}, \tag{3.4}$$

for the PbGl sections of the EMCal

$$E_{final} = \frac{E_{calib}}{1.021 - 0.02/E_{calib}}. \tag{3.5}$$

The invariant mass of the di-photon pair from Run8 data is shown for different transverse momenta of the π^0 in Fig. 3.25. When forming $\pi^0 h^{+/-}$ pairs in this analysis, the π^0 mass is required to be in a window from 112 to 162 MeV/c^2.

3.2.5 Selection of Charged Tracks

The following cuts have been used to select charged tracks:

- track quality is 63 or 31
- $|z_{DC}| < 70$ cm
- RICH veto, $n_0 < 0$

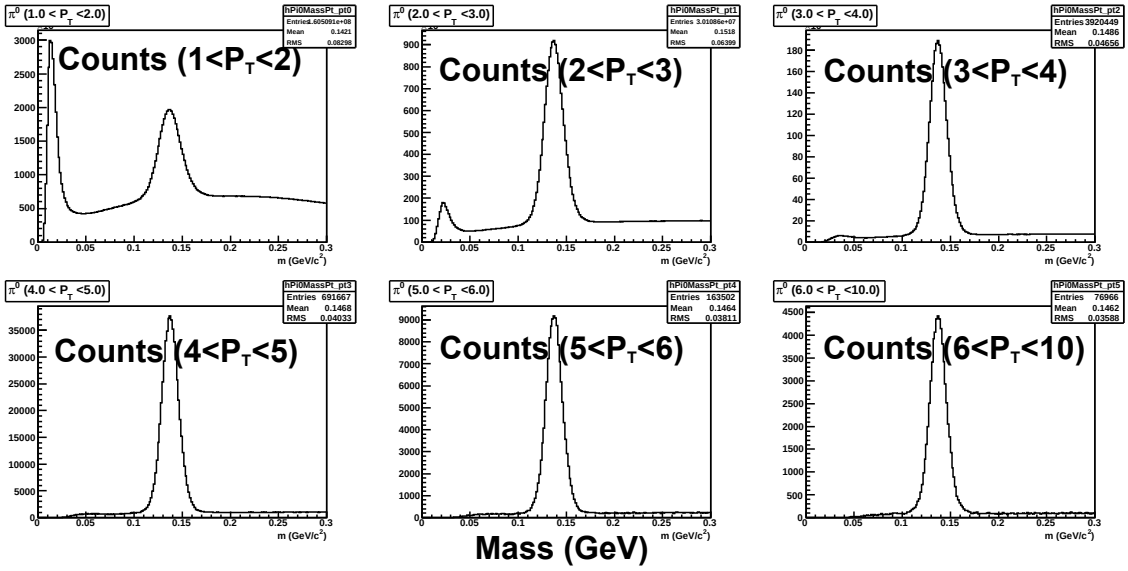

Figure 3.25: Di-photon invariant mass distribution for different π^0 p_T ranges.

- PC3 matching ($pc3sdphi$ and $pc3sdz$) within 3σ
- 1 GeV/c $< p_T <$ 4.7 GeV/c

The Beam offset correction is obtained from 6 zero field runs taken in run8 as described in Chapter 2. The momentum scale correction was done by matching proton mass from TOF information with its PDF value, details was also described in Chapter 2.

When calculating the asymmetries for the h^+h^- pairs, the ERT trigger bit check was used to make sure that one hadron fired the ERT trigger. It is possible that a minimum ionizing particle does not fire the trigger but still passes the trigger bit matching check. To study how to exclude such pairs, the distribution of the energy deposited in EMCal from a charged track that passed ERT trigger bit matching cut is shown in Figs. 3.29, 3.30. The p_T dependence of energy deposited in EMCal is shown in Figs. 3.27, 3.28.

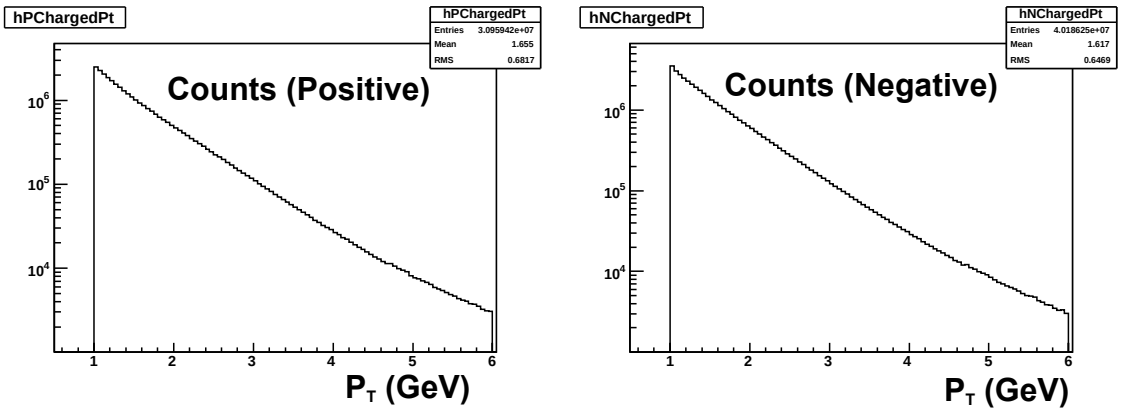

Figure 3.26: p_T (in GeV/c) distribution for charged tracks. Left and right plots are for tracks that are positively and negatively charged.

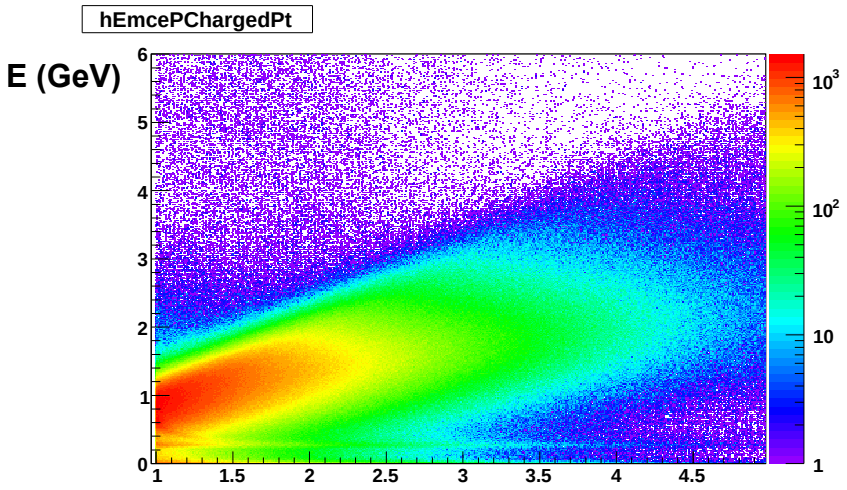

Figure 3.27: Energy deposited in EMCal for positive charged tracks. X-axis is p_T (GeV/c) of the charged track, Y-axis is energy (GeV) deposited in EMCal.

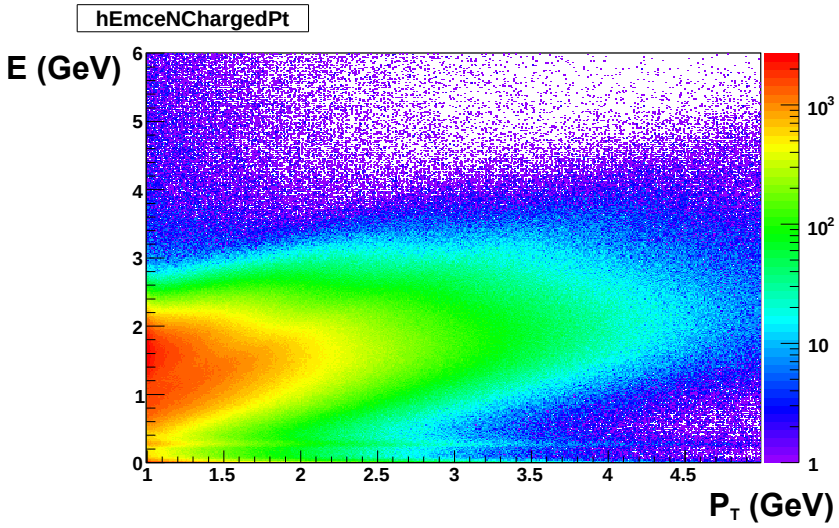

Figure 3.28: Energy deposited in EMCal for negative charged tracks. X-axis is p_T (GeV/c) of the charged track, Y-axis is energy (GeV) deposited in EMCal (emce).

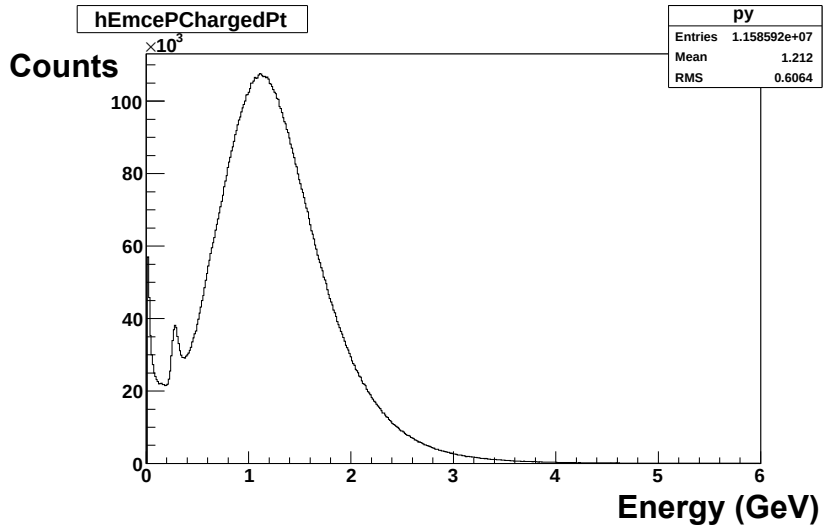

Figure 3.29: Energy deposited in EMCal for positive charged tracks. X-axis is energy (GeV) deposited in EMCal (emce).

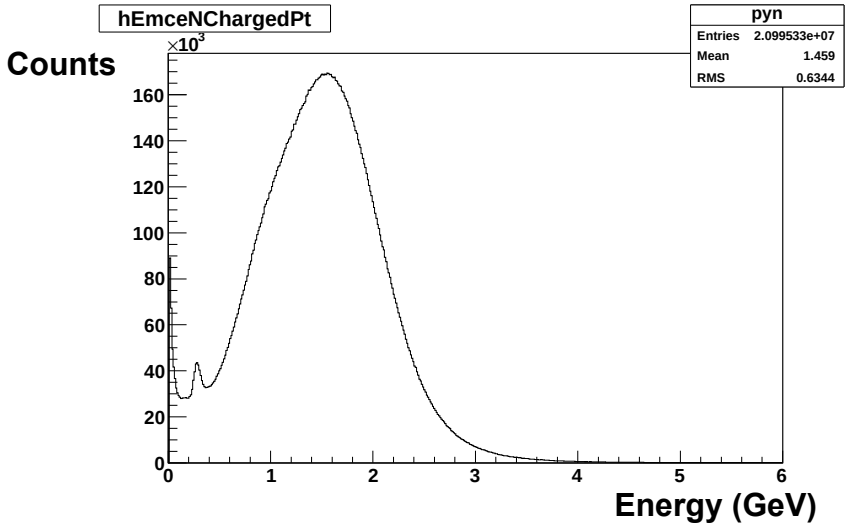

Figure 3.30: Energy deposited in EMCal for negative charged tracks. X-axis is energy (GeV) deposited in EMCal (emce).

From Figures 3.29 and 3.30 it is evident that the energy loss peak for minimum ionizing particles (MIPs) is located between 0.2 and 0.4 GeV. Therefore putting an additional cut on energy deposited in EMCal (emce) for charged tracks should eliminate the MIPs that pass the ERT trigger bit matching by coincidence. This cut reduces the statistics in h^+h^- pairs by 5%.

3.2.6 Hadron Pairs

In forming hadron pairs it is required that the two hadrons ($\pi^0 h^+$, $\pi^0 h^-$ or h^+h^-) must come from the same arm of the PHENIX central detectors. This requirement is an approximation to select hadron pairs from the same jet given the fact that the typical size of a jet coincides roughly with the azimuthal angle and rapidity coverage of the PHENIX central arm.

The invariant mass is calculated for each pair. In absence of particle identification, the pion mass is assigned to the un-identified hadrons, since charged pions are more abundant than kaons or protons in proton-proton collision. The invariant mass distributions for three types of the pairs are shown in Fig. 3.31, 3.32 and 3.33.

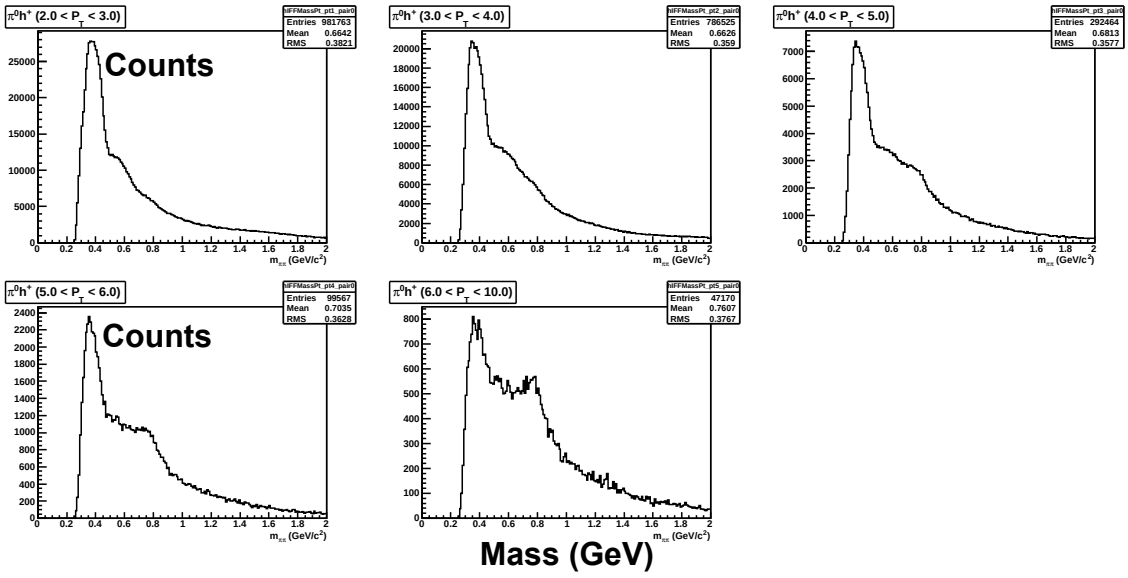

Figure 3.31: Invariant mass distribution for $\pi^0 h^+$ pairs in different p_T ranges.

3.3 Analysis Procedure

3.3.1 Analyzing Power vs. Mass of the Pair

As discussed in Section 1.3, there is a sine modulation of the single spin asymmetry in the angle of $\phi = \phi_{S_B} - \phi_{R_C}$. ϕ_{S_b} and ϕ_{R_C} are the angles between the event plane and the transverse proton spin and the di-hadron plane as

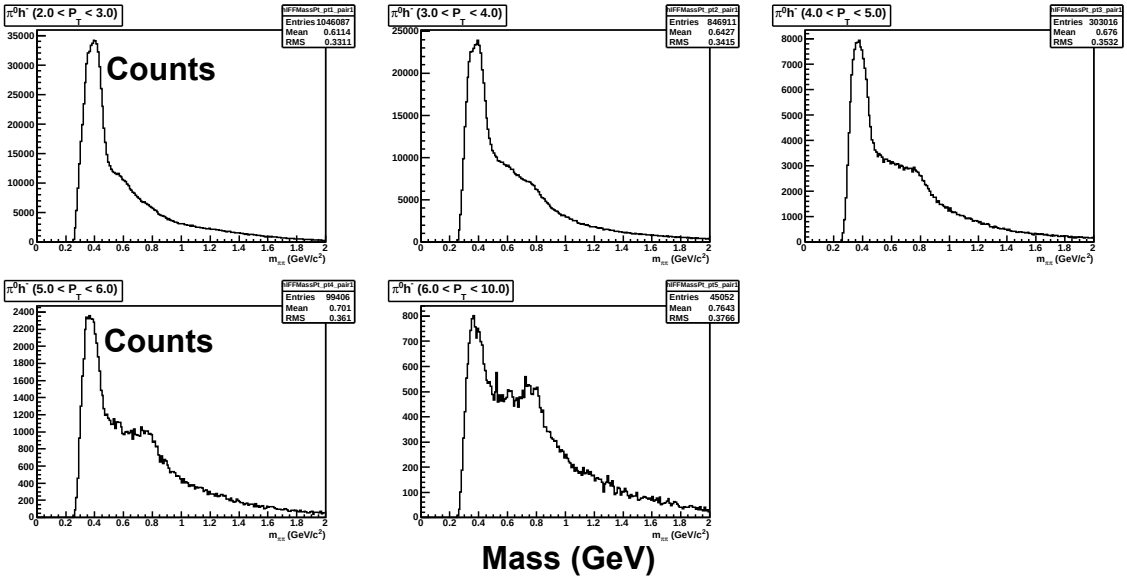

Figure 3.32: Invariant mass distribution for $\pi^0 h^-$ pairs in different p_T ranges.

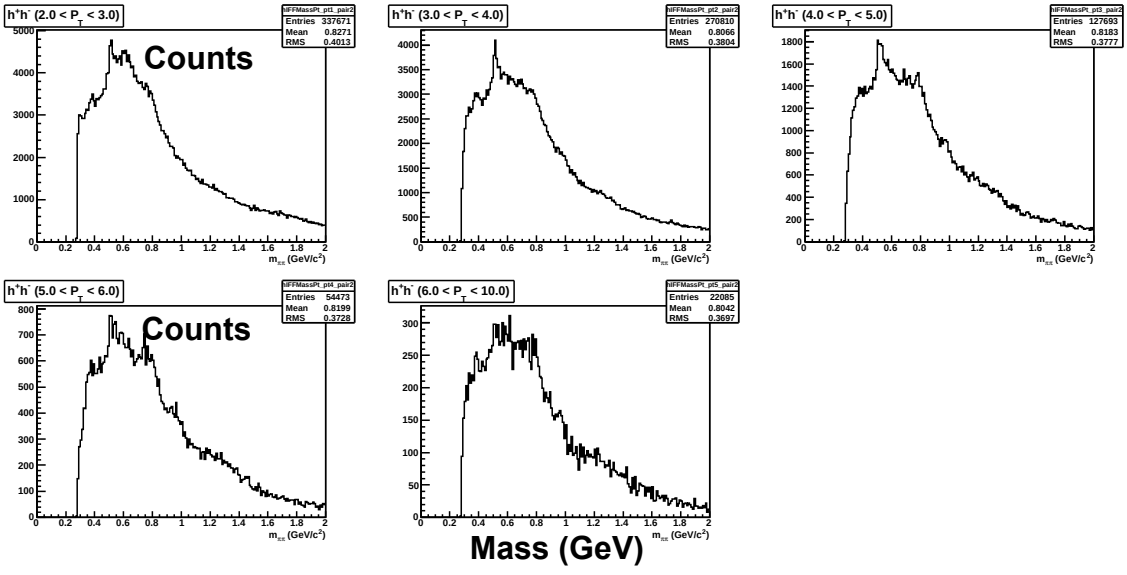

Figure 3.33: Invariant mass distribution for $h^+ h^-$ pairs in different p_T ranges.

shown in Fig. 3.34. Two protons with momenta $\vec{P}_A$ and $\vec{P}_B$, and polarization directions $\vec{S}_A$ and $\vec{S}_B$ collide. $\vec{P}_{C1}$ and $\vec{P}_{C2}$ are the momenta of the two hadrons produced inclusively, $\vec{P}_C = \vec{P}_{C1} + \vec{P}_{C2}$ and $\vec{R}_C = (\vec{P}_{C1} - \vec{P}_{C2})/2$. The hadron plane is defined by the momenta of the two hadrons ($\vec{P}_{C1}$ and $\vec{P}_{C2}$), and the scattering plane is defined by $\vec{P}_B$ and $\vec{P}_C$. Two azimuthal angles ϕ_{S_B} and ϕ_{R_C} can be written as

$$\cos\phi_{S_B} = \frac{(\hat{P}_B \times \vec{P}_C)}{|\hat{P}_B \times \vec{P}_C|} \cdot \frac{(\hat{P}_B \times \vec{S}_B)}{|\hat{P}_B \times \vec{S}_B|}, \quad \sin\phi_{S_B} = \frac{(\vec{P}_C \times \vec{S}_B) \cdot \hat{P}_B}{|\hat{P}_B \times \vec{P}_C|\,|\hat{P}_B \times \vec{S}_B|}, \quad (3.6)$$

$$\cos\phi_{R_C} = \frac{(\hat{P}_C \times \vec{P}_A)}{|\hat{P}_C \times \vec{P}_A|} \cdot \frac{(\hat{P}_C \times \vec{R}_C)}{|\hat{P}_C \times \vec{R}_C|}, \quad \sin\phi_{R_C} = \frac{(\vec{P}_A \times \vec{R}_C) \cdot \hat{P}_C}{|\hat{P}_C \times \vec{P}_A|\,|\hat{P}_C \times \vec{R}_C|}. \quad (3.7)$$

The angles defined above have an intuitive interpretation. The angle ϕ_{S_B} is the angle from the polarization vector $\vec{S}_B$ to the scattering plane. And the angle $\phi_{R_C} = \phi_{S_B} - phi_{R_C}$ is the angle from the scattering plane to the hadron plane. The definition of the angle ϕ in proton-proton collision was proposed in Ref. [31] and is equivalent to the one that has been used in a similar measurement from SIDIS at the HERMES experiment [25].

As mentioned above, $\vec{R}_C = (\vec{P}_{C1} - \vec{P}_{C2})/2$. Therefore, c_1 and c_2 need to be explicitly defined: in this analysis the ordering chosen is for (c_1, c_2) to be (π^0, h^+), (π^0, h^-) and (h^+, h^-) for three different types of hadron pairs.

The asymmetry is then calculated as a function of $\phi = \phi_{S_B} - \phi_{R_C}$

$$A_{UT}(\phi) = \frac{1}{P} \frac{N_\uparrow(\phi) - RN_\downarrow(\phi)}{N_\uparrow(\phi) + RN_\downarrow(\phi)} \quad (3.8)$$

where $N_\uparrow$ and $N_\downarrow$ are the counts of di-hadron pairs with the arrows indicating polarization directions of the proton beam, $R = L_\uparrow/L_\downarrow$ is the relative luminosity, and P is the beam polarization. The statistical error for $A_{UT}(\phi)$ is

$$\Delta A_{UT}(\phi) = \frac{1}{P} \frac{2R}{(N_\uparrow + RN_\downarrow)^2} \sqrt{(N_\uparrow + N_\downarrow) N_\uparrow N_\downarrow}. \quad (3.9)$$

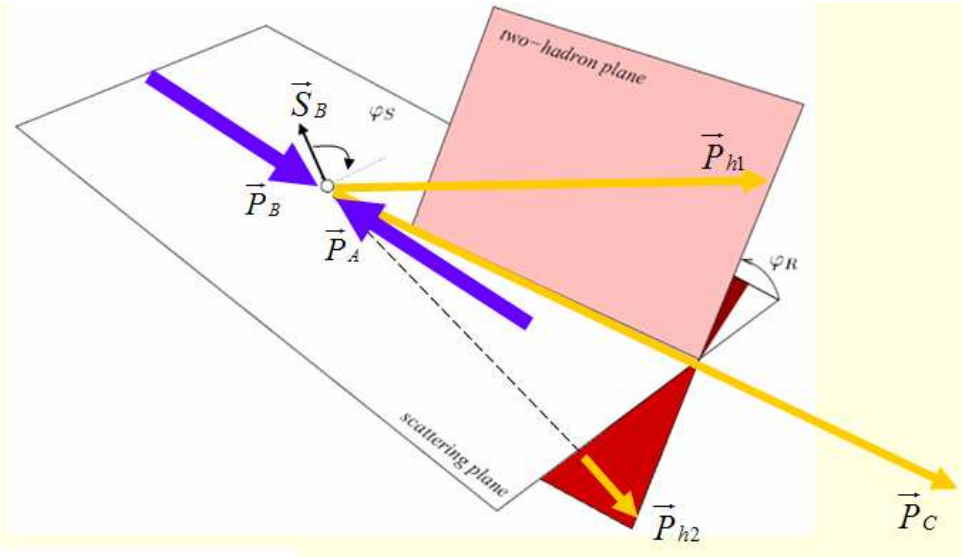

Figure 3.34: Definition of vectors and angles that have been used in this analysis.

Here the uncertainty for $N_\uparrow$ and $N_\downarrow$ has been taken as $\sqrt{N}$. As discussed in PHENIX Analysis Note 277, there is an enhancement to the uncertainty due to the fact that there can be multiple pairs in the same event. The enhancement factor is calculated as

$$k_{enhance} = \sqrt{\frac{\bar{k^2}}{\bar{k}}} \tag{3.10}$$

where k is the number of pairs per event. Eq. 3.10 can be derived with the following relations:

$$\bar{N} = \bar{k}\bar{n},\ \Delta n^2 = \bar{n},\ \Delta N^2 = \bar{n}\Delta_k^2 + \bar{k}^2\Delta_n^2 \tag{3.11}$$

where N stands for total number of pairs in n events and Δn, Δk and ΔN refer to the uncertainties of n, k and N. The enhancement factor $k_{enhance}$ used in this analysis are listed in Tables 3.4 and 3.5.

Since a $\sin\phi$ modulation is expected, the measured asymmetry must be fit with a sine function

$$A(\phi) = A_{UT}^{\sin\phi}\sin\phi \tag{3.12}$$

Mass (GeV/c^2)	$\pi^0 h^+$	$\pi^0 h^-$	$h^+ h^-$
0-0.5	1.229	1.216	1.012
0.5-0.78	1.211	1.205	1.013
0.78-1.0	1.098	1.099	1.005
1.0-1.3	1.095	1.096	1.004
1.3-2.0	1.105	1.093	1.005

Table 3.4: $k_{enhance}$ calculated for $\pi^0 h^+$, $\pi^0 h^-$ and $h^+ h^-$ pairs in different invariant mass ranges.

p_T (GeV/c)	$\pi^0 h^+$	$\pi^0 h^-$	$h^+ h^-$
2.0-3.0	1.1802	1.18222	1.00811
3.0-4.0	1.14665	1.13809	1.00764
4.0-5.0	1.11921	1.11292	1.00923
5.0-6.0	1.11338	1.10967	1.00898
6.0-10.0	1.12057	1.1249	1.01381

Table 3.5: $k_{enhance}$ calculated for $\pi^0 h^+$, $\pi^0 h^-$ and $h^+ h^-$ pairs in different p_T ranges.

to obtain the analyzing power $A_{UT}^{\sin\phi}$. Figs. 3.35 and 3.36 are examples of the count rates ($N_\uparrow$ and $N_\downarrow$) and the calculated $A_{UT}(\phi)$ for the blue beam in fill 7627, the invariant mass of the pair in the range 0.78 to 1.0 GeV/c^2.

In the analysis the ϕ dependence of the yields and the asymmetry is observed in all bins of pair invariant mass and pair transverse momentum and fitted with a $sin\phi$ in order to obtain the coefficients $A_{UT}^{\sin\phi}$. Fig. 3.37 shows the distribution of χ^2 from all the $\sin\phi$ fits that have been carried out in extracting $A_{UT}^{\sin\phi}$.

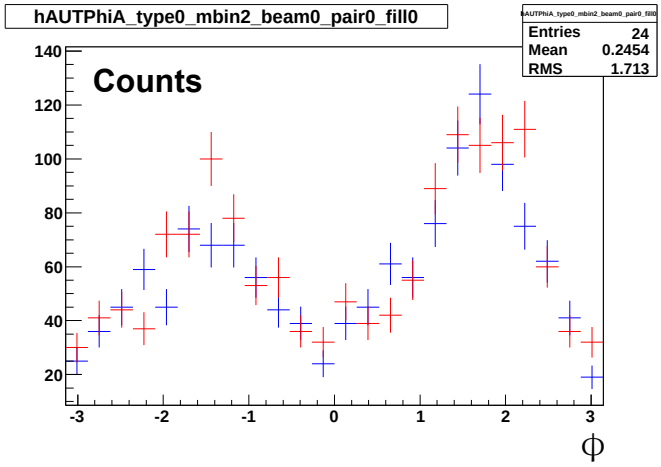

Figure 3.35: $N_\uparrow$ and $N_\downarrow$ as functions of ϕ for the blue beam in fill 7627 and the invariant mass of the pair in the range 0.78 to 1.0 GeV/c^2. Blue and red markers correspond to spin states $\uparrow$ and $\downarrow$. The counts are not normalized with relative luminosity.

The distribution of the angle ϕ shown in Fig. 3.35 results from the limited acceptance of the PHENIX central arm. This will be further discussed in the section 3.4.3 "systematic checks".

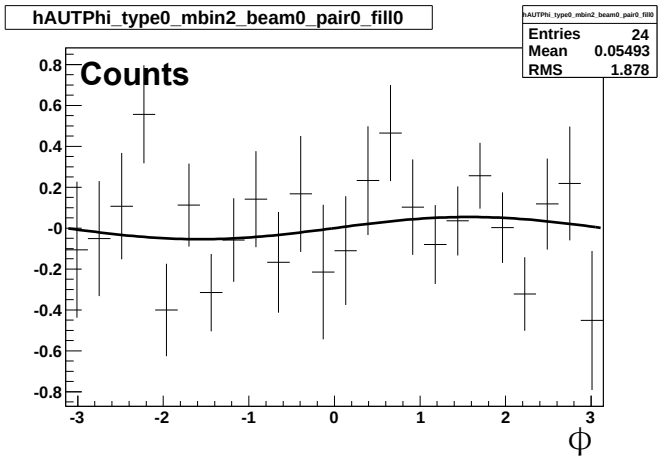

Figure 3.36: $A_{UT}(\phi)$ calculated with Eq. 3.8 for the blue beam in fill 7627 and the invariant mass of the pair in the range 0.78 to 1.0 GeV/c^2. To obtain the asymmetry, the counts are normalized with relative luminosity.

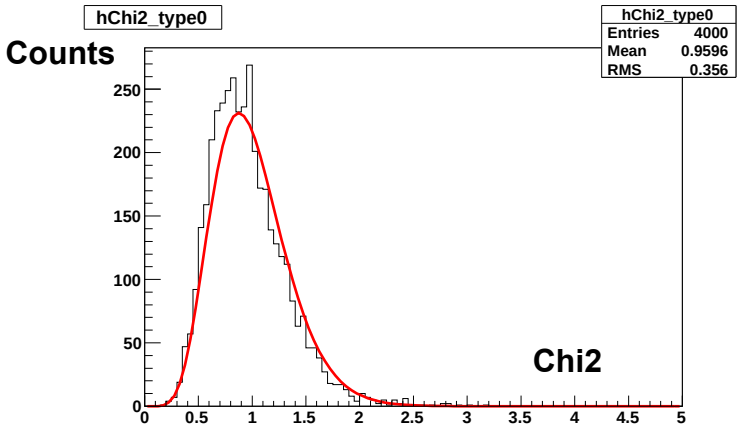

Figure 3.37: The distribution of reduced χ^2 (normalized by degree of freedom) from sine function fitting.

For all kinematic bins the analyzing power $A_{UT}^{\sin\phi}$ is calculated for each fill. To combine all fills, the analyzing powers for all fills are fit with a constant, which is equivalent to taking the weighted average with the statistical uncertainties used as weights

$$A_{UT(allfills)}^{\sin\phi} = \frac{\sum_{i=fills} A_{UT,i}^{\sin\phi}/\sigma_i^2}{\sum_{i=fills} 1/\sigma_i^2} \tag{3.13}$$

As indicated in model calculations [28], the asymmetry can depend on the invariant mass of the hadron pair. Therefore the asymmetries are calculated in 5 different bins of the pair's invariant mass. The boundaries of the mass bins are at 0, 0.5, 0.78, 1.0, 1.3, 2.0 GeV/c^2.

Additionally, since the ERT trigger uses different circuits for even and odd bunch crossings, the asymmetry are calculated separately for even/odd bunches to avoid possible bias from the different trigger performance for odd and even bunch crossings.

The resulting analyzing powers are shown in Figs. 3.38, 3.39 and 3.40 as functions of fill number. The analyzing powers for all fills combined are shown in Figs. 3.41, 3.42 and 3.43 for blue/yellow beams and even/odd bunch crossings. The analyzing powers for all fills combined are shown in Figs. 3.44, 3.45 and 3.46, corresponding data are listed in Tables 3.6, 3.7 and 3.8. As a summary, the analyzing powers for the different pairs are shown in Figure 3.47.

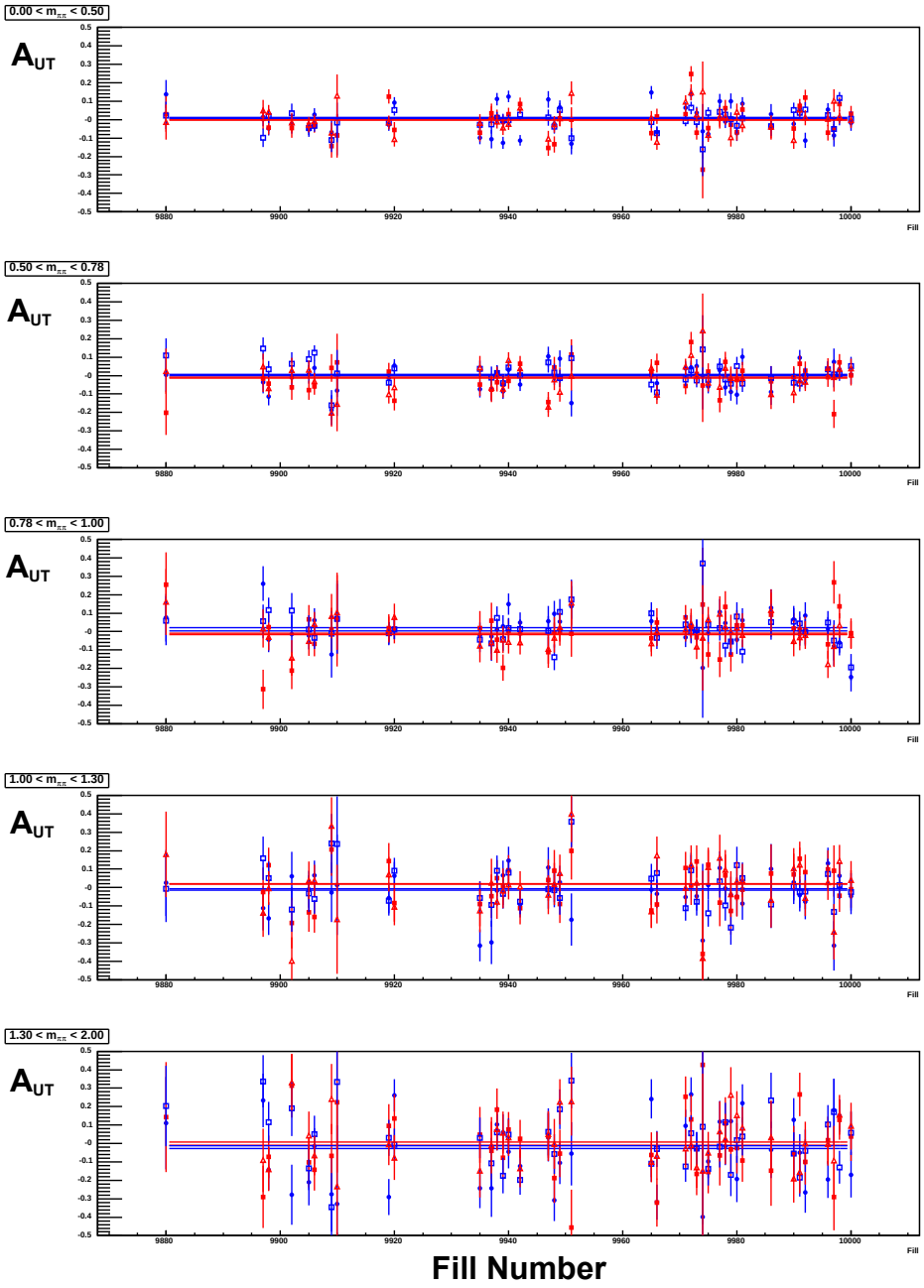

Figure 3.38: Analyzing power for each fill from $\pi^0 h^+$ pairs in 5 bins of pair mass. Blue and red markers correspond to blue and yellow beam, square and triangular markers correspond to even and odd bunch crossings.

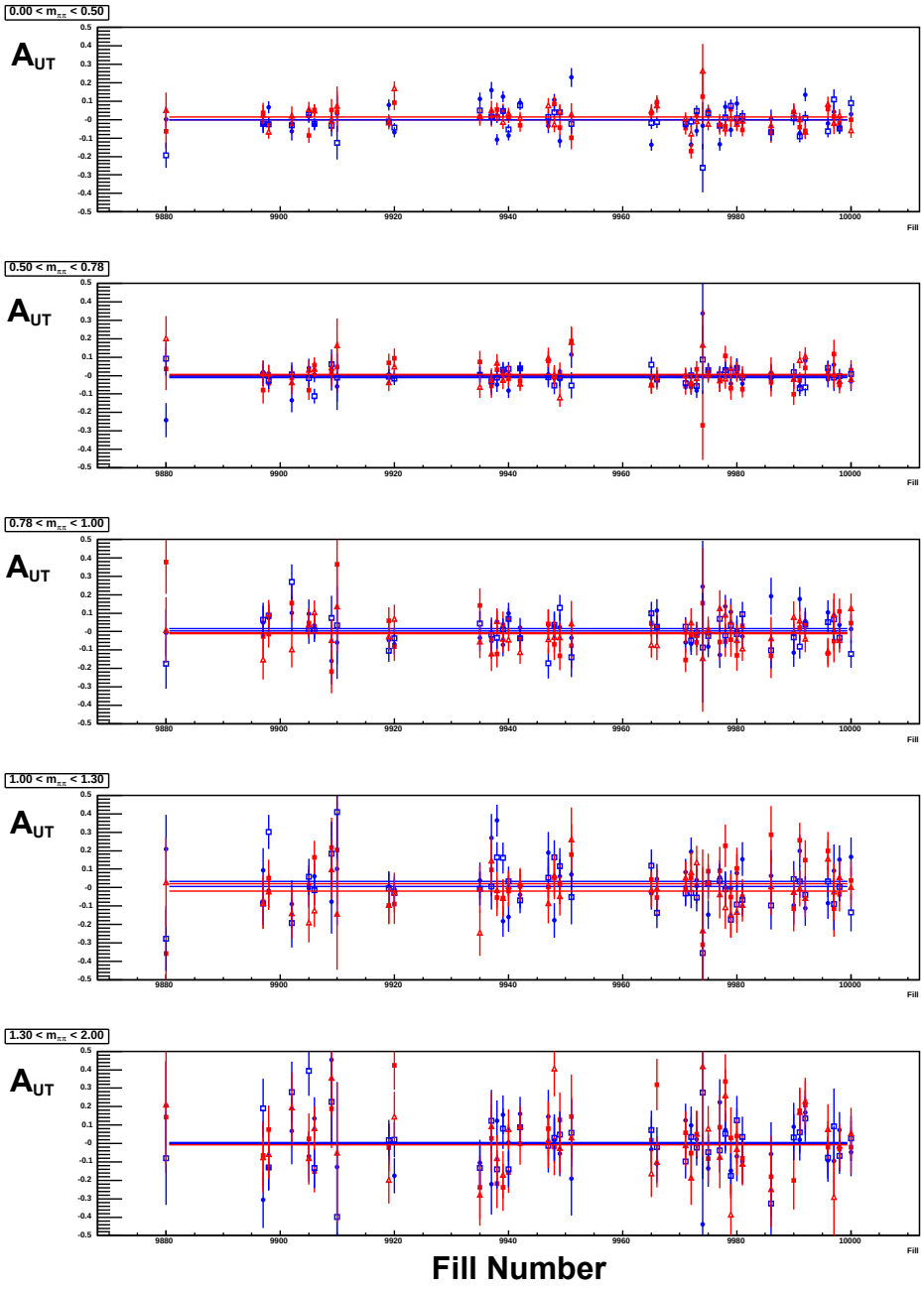

Figure 3.39: Analyzing power for each fill from $\pi^0 h^-$ pairs in 5 bins of pair mass. Blue and red markers correspond to blue and yellow beam, square and triangular markers correspond to even and odd bunch crossings.

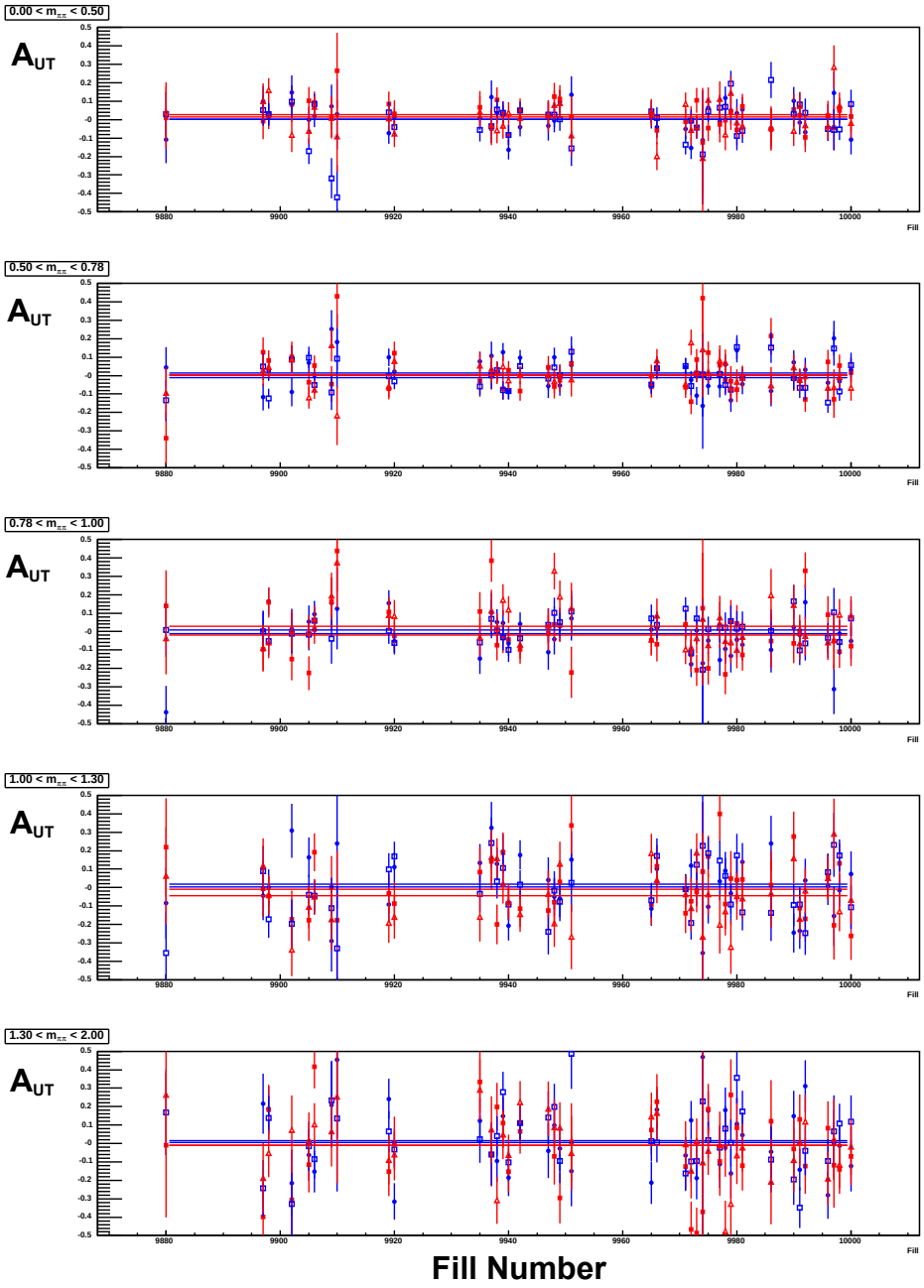

Figure 3.40: Analyzing power for each fill from h^+h^- pairs in 5 bins of pair mass. Blue and red markers correspond to blue and yellow beam, square and triangular markers correspond to even and odd bunch crossings.

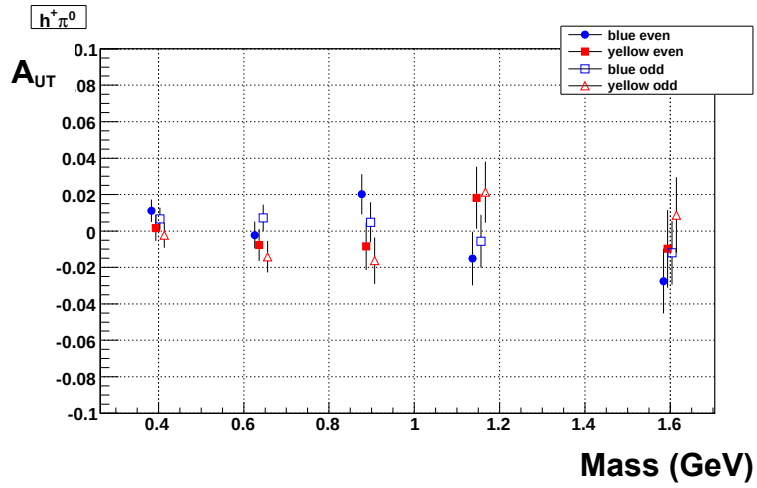

Figure 3.41: Analyzing power for $\pi^0 h^+$ pairs with all fills combined in 5 bins of pair mass. Even and odd crossings separated.

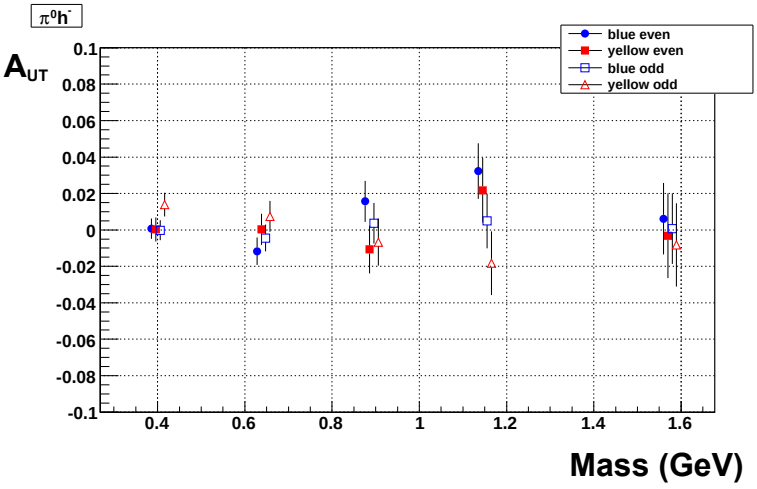

Figure 3.42: Analyzing power for $\pi^0 h^-$ pairs with all fills combined in 5 bins of pair mass. Even and odd crossings separated.

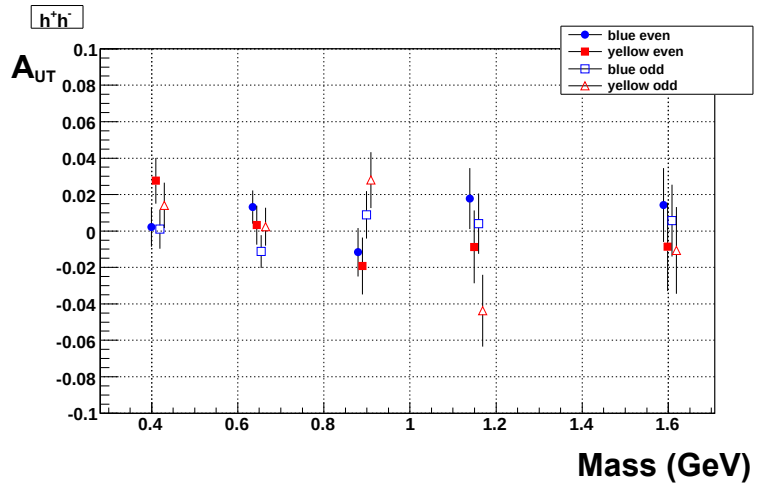

Figure 3.43: Analyzing power for h^+h^- pairs with all fills combined in 5 bins of pair mass. Even and odd crossings separated.

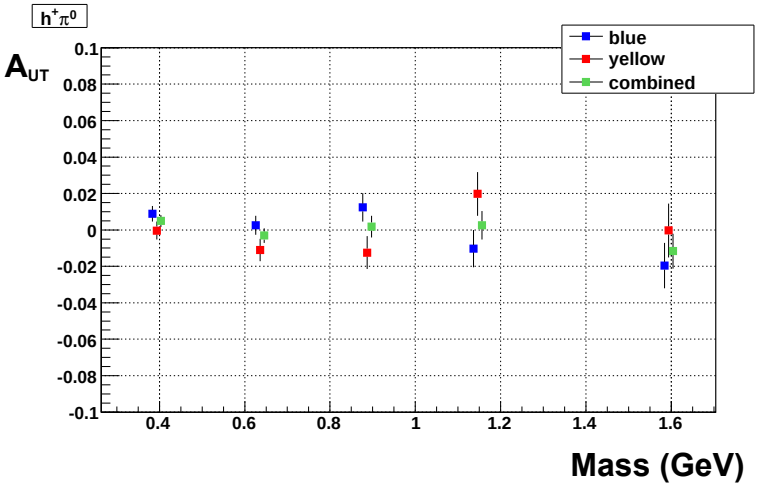

Figure 3.44: Analyzing power for $\pi^0 h^+$ pairs with all fills combined in 5 bins of pair mass. For blue and yellow beams, and both beams combined.

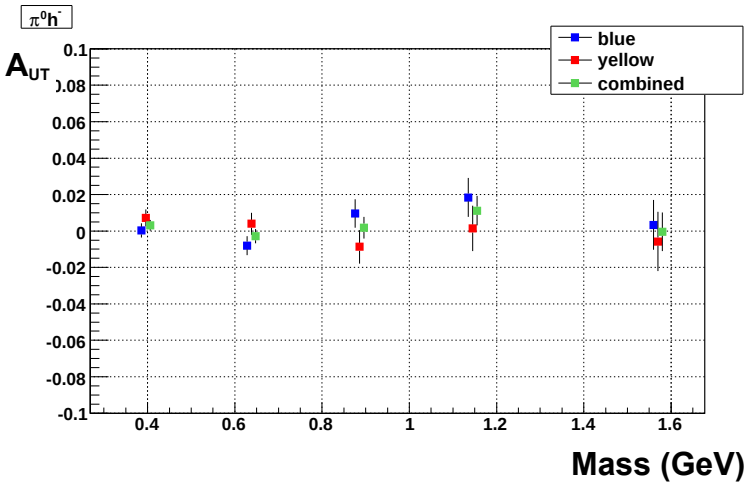

Figure 3.45: Analyzing power for $\pi^0 h^-$ pairs with all fills combined in 5 bins of pair mass. For blue and yellow beams, and both beams combined.

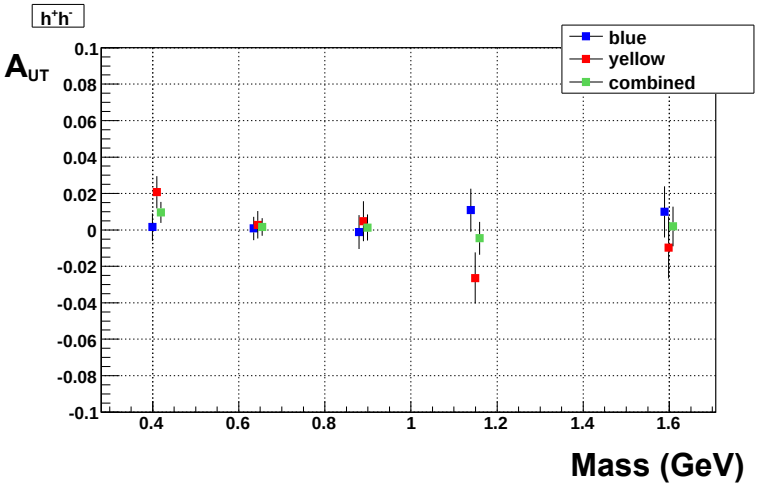

Figure 3.46: Analyzing power for $h^+ h^-$ pairs with all fills combined in 5 bins of pair mass. For blue and yellow beams, and both beams combined.

Mass bin (GeV/c^2)	m_{avg}	$A_{UT}^{\sin\phi}$ (blue)	stat. err.	$A_{UT}^{\sin\phi}$ (yellow)	stat. err.	$A_{UT}^{\sin\phi}$ (comb'd)	stat. err.
0.00 - 0.50	0.39	-0.0001	0.0045	0.0038	0.0053	0.0016	0.0034
0.50 - 0.78	0.63	-0.0011	0.0053	-0.0153	0.0063	-0.0070	0.0040
0.78 - 1.00	0.88	0.0112	0.0077	-0.0070	0.0091	0.0036	0.0059
1.00 - 1.30	1.14	-0.0147	0.0103	0.0164	0.0121	-0.0016	0.0078
1.30 - 2.00	1.59	-0.0099	0.0128	-0.0021	0.0151	-0.0067	0.0098

Table 3.6: Analyzing power $A_{UT}^{\sin\phi}$ for blue beam, yellow beams and two beams combined from $\pi^0 h^+$ pairs.

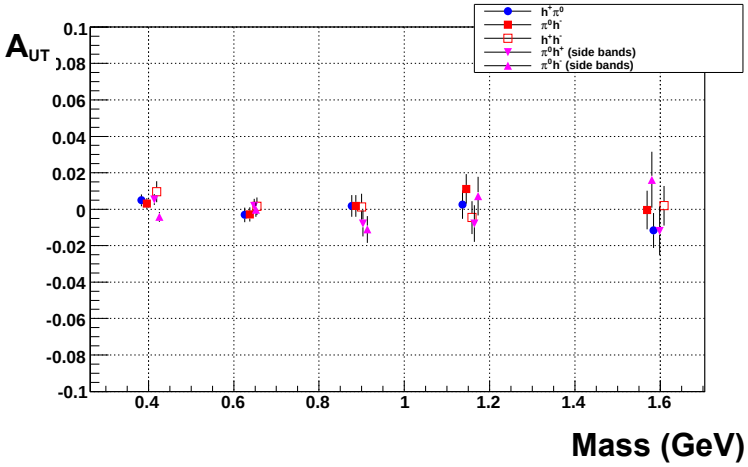

Figure 3.47: Analyzing power for 3 pairs in 5 bins of pair mass.

Mass bin (GeV/c^2)	m_{avg}	$A_{UT}^{\sin\phi}$ (blue)	stat. err.	$A_{UT}^{\sin\phi}$ (yellow)	stat. err.	$A_{UT}^{\sin\phi}$ (comb'd)	stat. err.
0.00 - 0.50	0.39	0.0033	0.0041	0.0112	0.0048	0.0066	0.0031
0.50 - 0.78	0.63	-0.0039	0.0052	0.0051	0.0059	0.0000	0.0039
0.78 - 1.00	0.88	0.0090	0.0077	-0.0042	0.0089	0.0034	0.0058
1.00 - 1.30	1.14	0.0120	0.0104	-0.0021	0.0122	0.0060	0.0079
1.30 - 2.00	1.56	0.0032	0.0134	-0.0007	0.0159	0.0016	0.0103

Table 3.7: Analyzing power $A_{UT}^{\sin\phi}$ for blue beam, yellow beams and two beams combined from $\pi^0 h^-$ pairs.

Mass bin (GeV/c^2)	m_{avg}	$A_{UT}^{\sin\phi}$ (blue)	stat. err.	$A_{UT}^{\sin\phi}$ (yellow)	stat. err.	$A_{UT}^{\sin\phi}$ (comb'd)	stat. err.
0.00 - 0.50	0.40	0.0018	0.0078	0.0146	0.0090	0.0072	0.0059
0.50 - 0.78	0.63	0.0034	0.0065	0.0063	0.0076	0.0046	0.0049
0.78 - 1.00	0.88	0.0074	0.0092	0.0059	0.0108	0.0068	0.0070
1.00 - 1.30	1.14	0.0156	0.0116	-0.0133	0.0138	0.0037	0.0089
1.30 - 2.00	1.59	0.0108	0.0142	-0.0196	0.0169	-0.0017	0.0109

Table 3.8: Analyzing power $A_{UT}^{\sin\phi}$ for blue beam, yellow beams and two beams combined from h^+h^- pairs.

3.3.2 Background Subtraction for $\pi^0 h^{+/-}$ Pairs

As mentioned above, the mass window used for the π^0 signal in the di-photon invariant spectra extends from 112 to 162 MeV/c^2 ("peak region"). Therefore, the analyzing power calculated for $\pi^0 h^+$ and $\pi^0 h^-$ pairs actually includes contributions from both π^0 and di-photon combinatorial background. The measured analyzing power can be separated into contributions from signal π^0s and from the combinatorial background:

$$A^{total} = (1 - r)A^{sig} + rA^{bg}, \tag{3.14}$$

where the background ratio $r = N^{bg}/(N^{sig} + N^{bg})$. From Eq. 3.14, the actual analyzing power is

$$A^{sig} = \frac{A^{total} - rA^{bg}}{1 - r}, \tag{3.15}$$

and its uncertainty is

$$\sigma_{A^{sig}} = \frac{\sqrt{\sigma^2_{A^{total}} + r^2\sigma^2_{A^{bg}}}}{1 - r}. \tag{3.16}$$

In order to measure A^{bg}, a pure sample of the combinatorial background is selected from the di-photon invariant mass spectrum at 47-97 and 177-227 MeV/c^2 ("side bands"). The analyzing power is then calculated for pairs that have a "π^0" from the side bands and a $h^{+/-}$. Results are shown in Figs. 3.48 and 3.49.

The background ratio r under the peak region is determined by fitting signal and background region of the di-photon invariant mass spectrum and by extrapolating the background from the fit into the signal region. Since the analyzing power has been calculated in 5 bins of the pair mass, The di-photon mass distributions are shown for the different pair mass bins in Figs. 3.50 and 3.51. The spectra are fit with a gaussian plus a second order polynomial

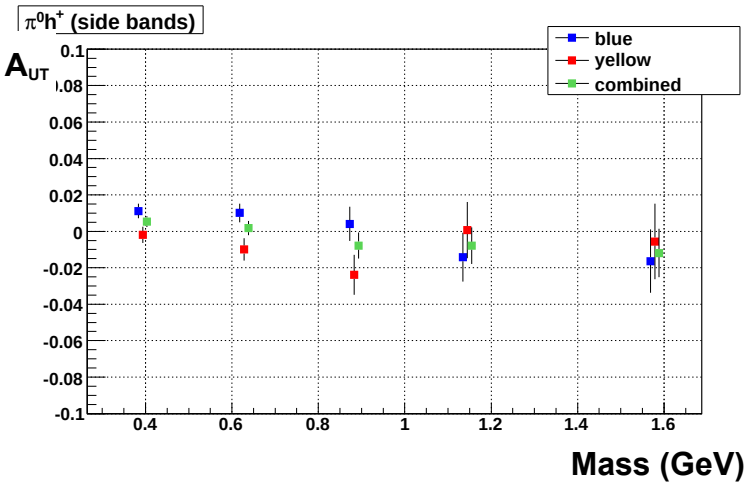

Figure 3.48: Background analyzing power for $\pi^0 h^+$ pairs with all fills combined in 5 bins of pair mass. The π^0s are taken as combinatorial di-photons from the side bands. The background asymmetries are shown for the two beams separately and for the results from the two beams combined.

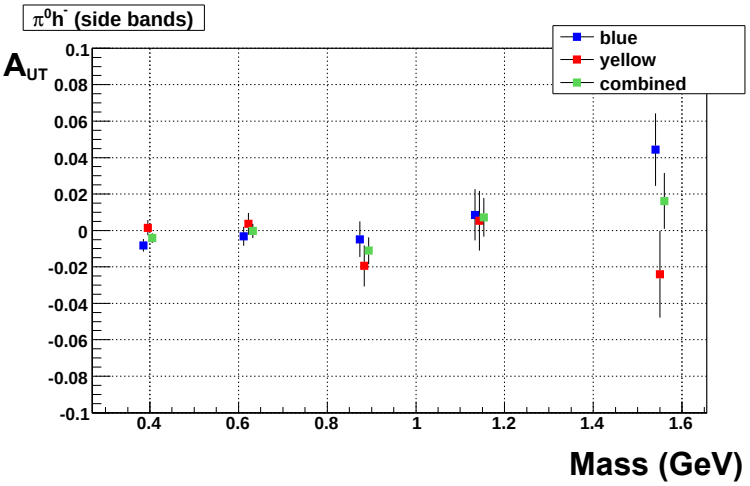

Figure 3.49: Analyzing power for $\pi^0 h^-$ pairs with all fills combined in 5 bins of pair mass. The π^0s are taken as combinatorial di-photons from the side bands. The background asymmetries are shown for the two beams separately and for the results from the two beams combined.

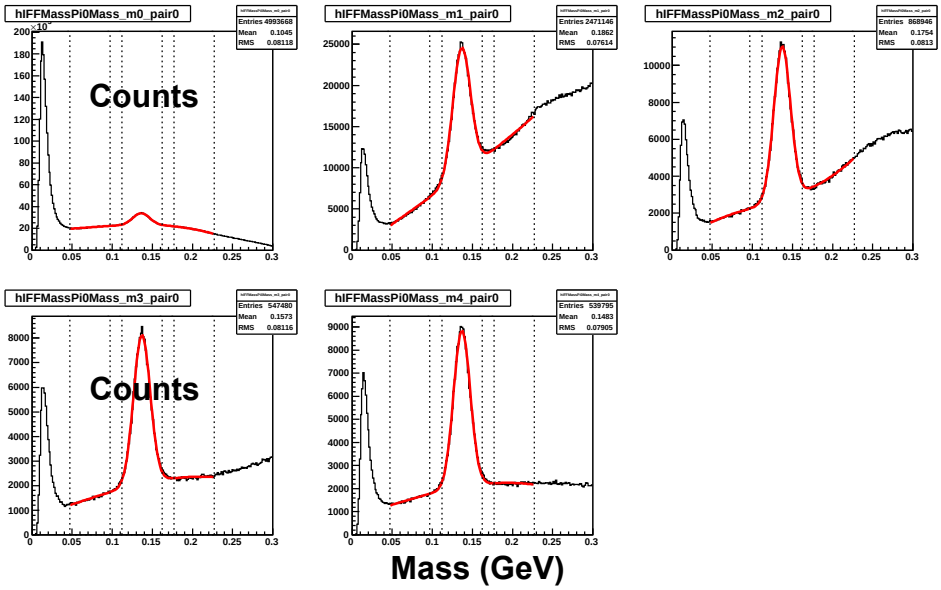

Figure 3.50: Di-photon invariant mass distribution in different ranges of pair mass. (For $\pi^0 h^+$ pairs)

to describe both the signal and background in the di-photon spectra. The values of r for $\pi^0 h^{+/-}$ pairs in 5 bins of the pair mass are listed in Table 3.9

m bin	0	1	2	3	4
$\pi^0 h^+$	0.81	0.54	0.40	0.40	0.38
$\pi^0 h^-$	0.81	0.52	0.39	0.40	0.36

Table 3.9: Background ratio under peak region in the di-photon invariant mass spectrum.

Using Eqs. 3.15 and 3.16, the analyzing power and its statistical uncertainty is calculated for $\pi^0 h^{+/-}$ pairs. The results are listed in Tables 3.10 and 3.11.

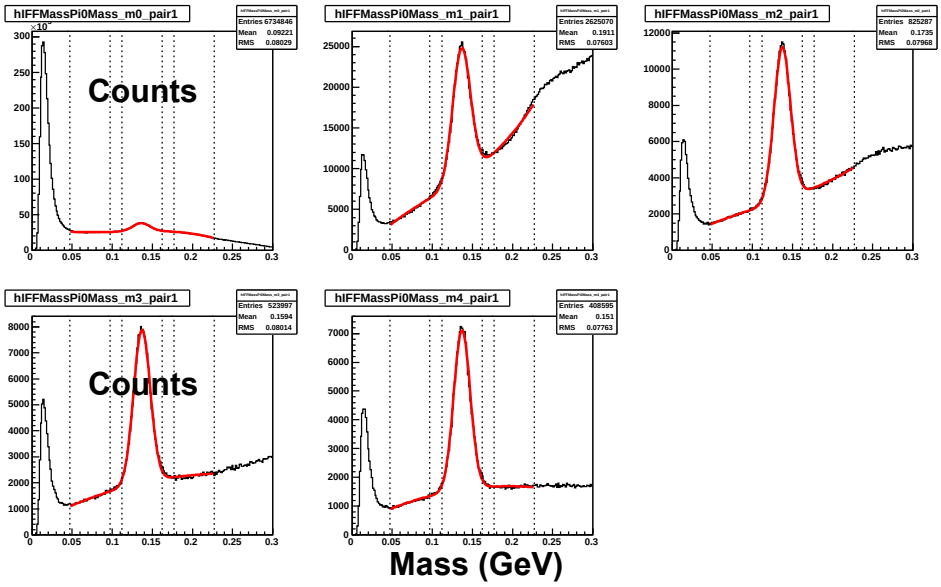

Figure 3.51: Di-photon invariant mass distribution in different ranges of pair mass. (For $\pi^0 h^-$ pairs)

m bin (GeV/c^2)	$\langle m \rangle$	$A_{UT}^{\sin\phi}$ (comb'd)	stat. err.
0.00 - 0.50	0.39	0.0020	0.0224
0.50 - 0.78	0.64	0.0169	0.0099
0.78 - 1.00	0.88	-0.0098	0.0108
1.00 - 1.30	1.14	-0.0032	0.0147
1.30 - 2.00	1.59	0.0040	0.0177

Table 3.10: Analyzing power for $\pi^0 h^+$ pairs (after subtraction of combinatorial background for π^0).

m bin (GeV/c^2)	$\langle m \rangle$	$A_{UT}^{\sin\phi}$ (comb'd)	stat. err.
0.00 - 0.50	0.39	0.0353	0.0224
0.50 - 0.78	0.65	-0.0024	0.0099
0.78 - 1.00	0.88	0.0122	0.0108
1.00 - 1.30	1.14	0.0099	0.0147
1.30 - 2.00	1.57	-0.0073	0.0177

Table 3.11: Analyzing power for $\pi^0 h^-$ pairs (after subtraction of combinatorial background for π^0).

m bin (GeV/c^2)	$\langle m \rangle$	$A_{UT}^{\sin\phi}$ (comb'd)	stat. err.
0.00 - 0.50	0.39	0.0353	0.0224
0.50 - 0.78	0.65	-0.0024	0.0099
0.78 - 1.00	0.88	0.0122	0.0108
1.00 - 1.30	1.14	0.0099	0.0147
1.30 - 2.00	1.57	-0.0073	0.0177

Table 3.12: Analyzing power for $h^+ h^-$ pairs. Not updated from the previous section as no background subtraction is needed for charged hadron pairs.

The analyzing power are shown in Fig. 3.52 where the analyzing power for $\pi^0 h^{+/-}$ pairs, background analyzing power from combinatorial di-photons has been subtracted.

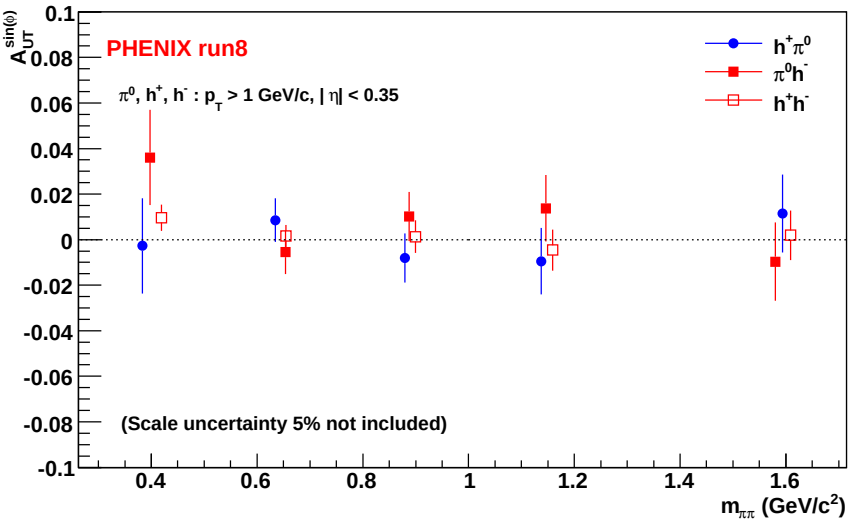

Figure 3.52: Analyzing power for 3 pairs as a function of invariant mass of the pair. (For $\pi^0 h^+$ and $\pi^0 h^-$ pairs, combinatorial background for π^0 has been subtracted.) This plot is from 4x4c triggered data sample. The 4x4c trigger has a threshold at 1.5 GeV for electromagnetic clusters in the EMCal detector.

The same analysis was repeated for 4x4a triggered data sample too. The result is shown in Fig. 3.53 and Tables 3.13,3.14,3.15.

3.3.3 Analyzing Power vs. p_T of the Pair

The analyzing power is also calculated for different of ranges p_T. The boundaries for the p_T bins are 2.0, 3.0, 4.0, 5.0, 6.0 and 10.0 GeV/c. The results are shown in Fig. 3.68, and the data is listed in Tables 3.17, 3.18, 3.19.

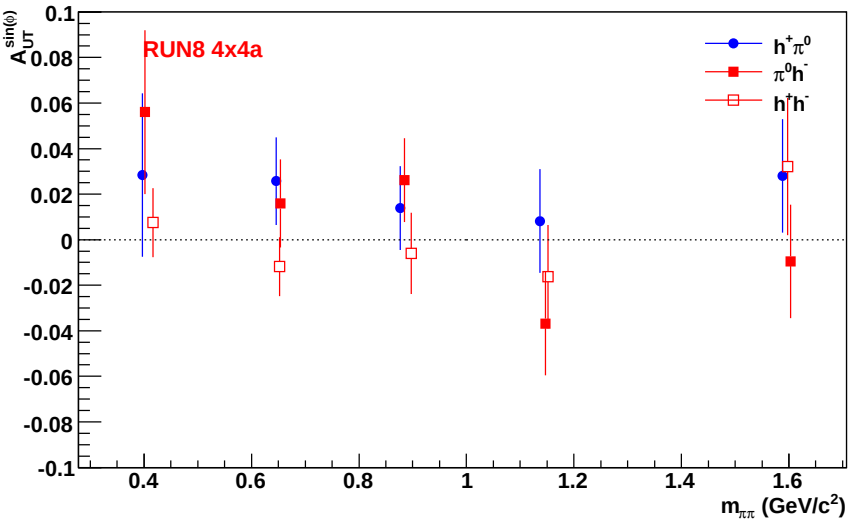

Figure 3.53: Analyzing power for 3 pairs as a function of invariant mass of the pair. (For $\pi^0 h^+$ and $\pi^0 h^-$ pairs, combinatorial background for π^0 has been subtracted.) This plot is from 4x4a triggered data sample.

m bin (GeV/c^2)	$\langle m \rangle$	$A_{UT}^{\sin\phi}$ (comb'd)	stat. err.
0.00 - 0.50	0.397	0.0284	0.0359
0.50 - 0.78	0.646	0.0257	0.0193
0.78 - 1.00	0.877	0.0138	0.0184
1.00 - 1.30	1.137	0.0082	0.0227
1.30 - 2.00	1.588	0.0280	0.0249

Table 3.13: Analyzing power for $\pi^0 h^+$ pairs (after subtraction of combinatorial background for π^0). This is from 4x4a data sample.

m bin (GeV/c^2)	$\langle m \rangle$	$A_{UT}^{\sin\phi}$ (comb'd)	stat. err.
0.00 - 0.50	0.394	0.0560	0.0359
0.50 - 0.78	0.646	0.0159	0.0193
0.78 - 1.00	0.877	0.0262	0.0184
1.00 - 1.30	1.139	-0.0368	0.0227
1.30 - 2.00	1.595	-0.0095	0.0249

Table 3.14: Analyzing power for $\pi^0 h^-$ pairs (after subtraction of combinatorial background for π^0). This is from 4x4a data sample.

m bin (GeV/c^2)	$\langle m \rangle$	$A_{UT}^{\sin\phi}$ (comb'd)	stat. err.
0.00 - 0.50	0.401	0.0075	0.0152
0.50 - 0.78	0.636	-0.0118	0.0129
0.78 - 1.00	0.881	-0.0060	0.0179
1.00 - 1.30	1.136	-0.0163	0.0227
1.30 - 2.00	1.582	0.0321	0.0301

Table 3.15: Analyzing power for $h^+ h^-$ pairs. This is from 4x4a data sample.

Model calculations suggest that non-zero asymmetries may be observed in the ρ meson mass region. Consequently, the p_T dependence of A_{UT} has been studied for di-hadron masses between 0.5 and 1.0 GeV/c^2.

Similar to the previous analysis of the invariant mass dependence of the analyzing power, it is first verified that the A_{UT} only shows statistical fluctuations as function of time. Figs. 3.54, 3.55 and 3.56 show the analyzing power for the three different hadron pairs a function of fill number. The asymmetries are found consistent with statistical fluctuations. The analyzing powers from all fills combined are shown in Figs. 3.57, 3.58 and 3.59 for blue/yellow beams and even/odd bunch crossings. Summing the asymmetries for both beams and even and odd bunch crossings results in the asymmetries shown in Figs. 3.60, 3.61 and 3.62.

The background for π^0 is subtracted in a way similar to what was described in the previous section. In order to measure A^{bg}, a sample of the combinatorial background is selected from the di-photon invariant mass spectrum at 47-97 and 177-227 MeV/c^2 ("side bands"). The analyzing power is

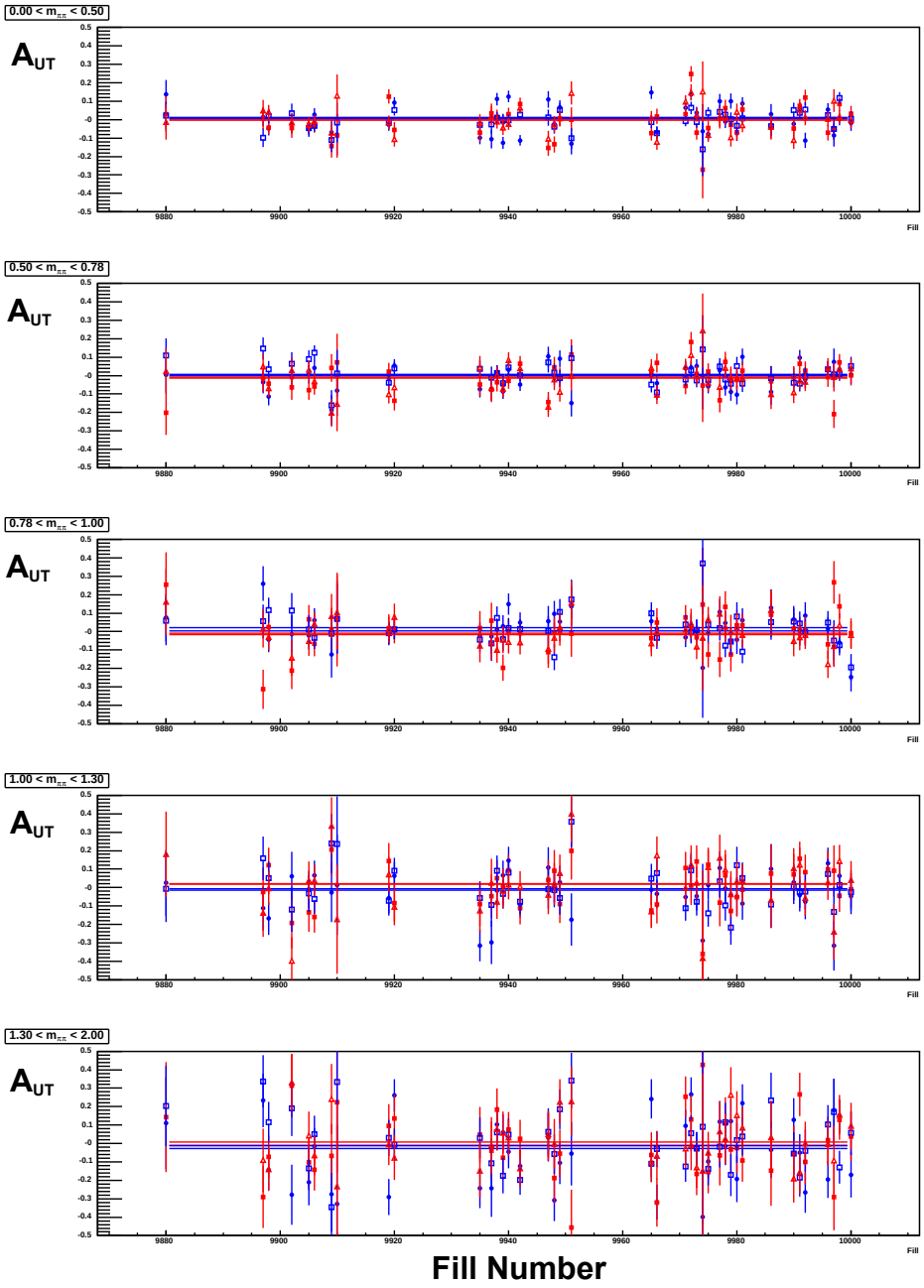

Figure 3.54: Analyzing power for each fill from $\pi^0 h^+$ pairs in 5 bins of pair p_T. Blue and red markers correspond to blue and yellow beam, square and triangular markers correspond to even and odd bunch crossings.

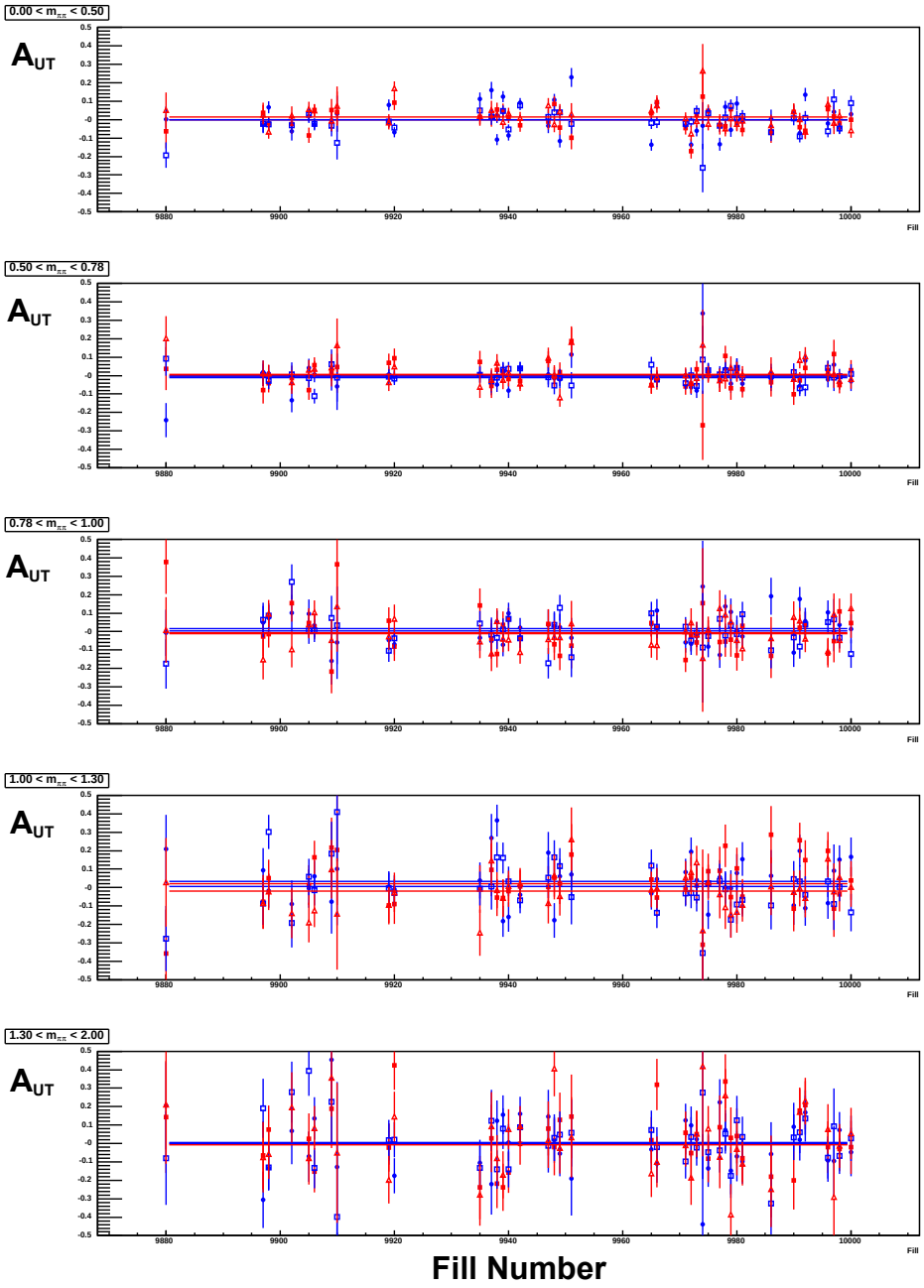

Figure 3.55: Analyzing power for each fill from $\pi^0 h^-$ pairs in 5 bins of pair p_T. Blue and red markers correspond to blue and yellow beam, square and triangular markers correspond to even and odd bunch crossings.

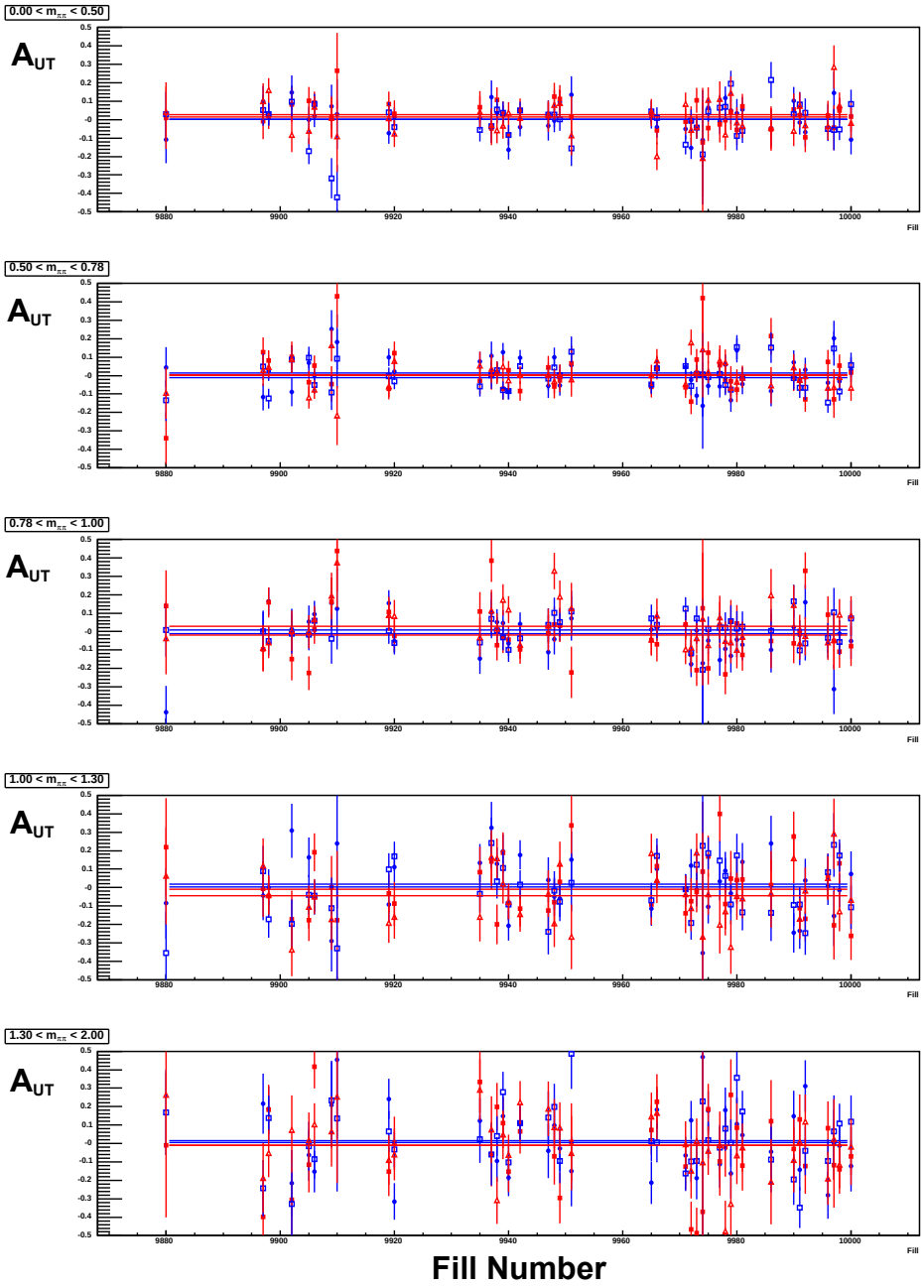

Figure 3.56: Analyzing power for each fill from h^+h^- pairs in 5 bins of pair p_T. Blue and red markers correspond to blue and yellow beam, square and triangular markers correspond to even and odd bunch crossings.

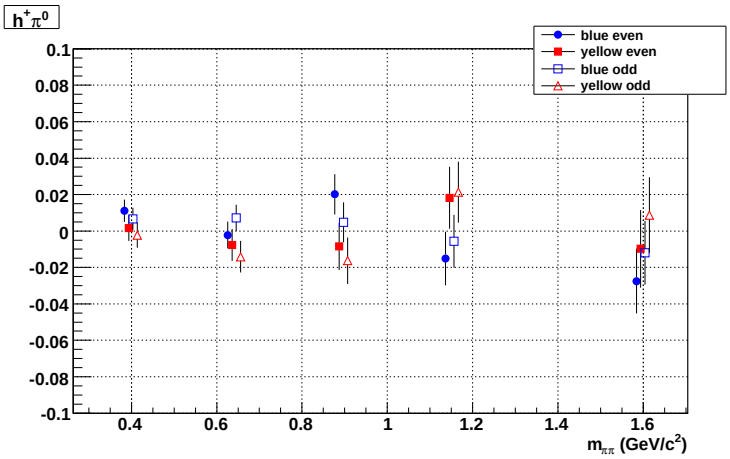

Figure 3.57: Analyzing power for $\pi^0 h^+$ pairs with all fills combined in 5 bins of pair p_T. Even and odd crossings separated.

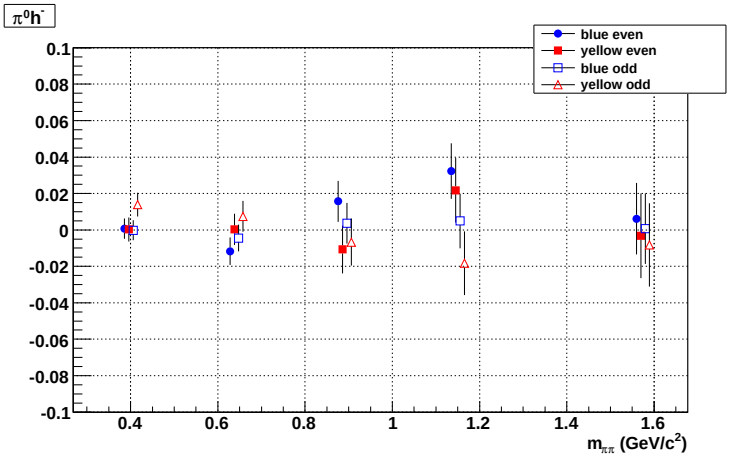

Figure 3.58: Analyzing power for $\pi^0 h^-$ pairs with all fills combined in 5 bins of pair p_T. Even and odd crossings separated.

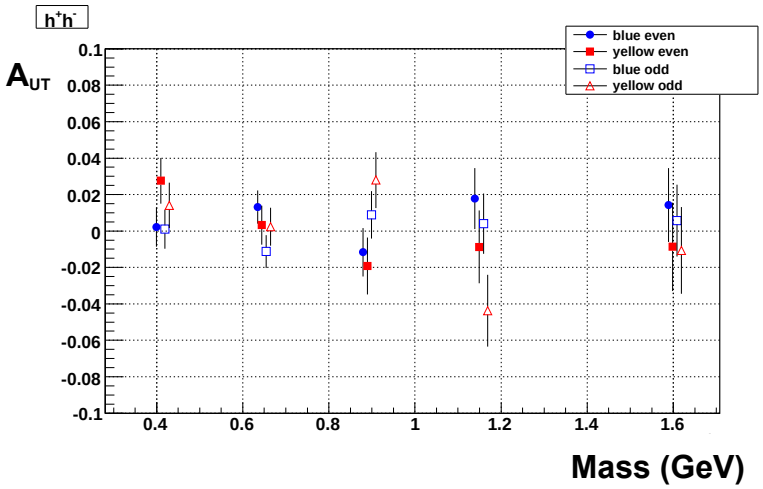

Figure 3.59: Analyzing power for h^+h^- pairs with all fills combined in 5 bins of pair p_T. Even and odd crossings separated.

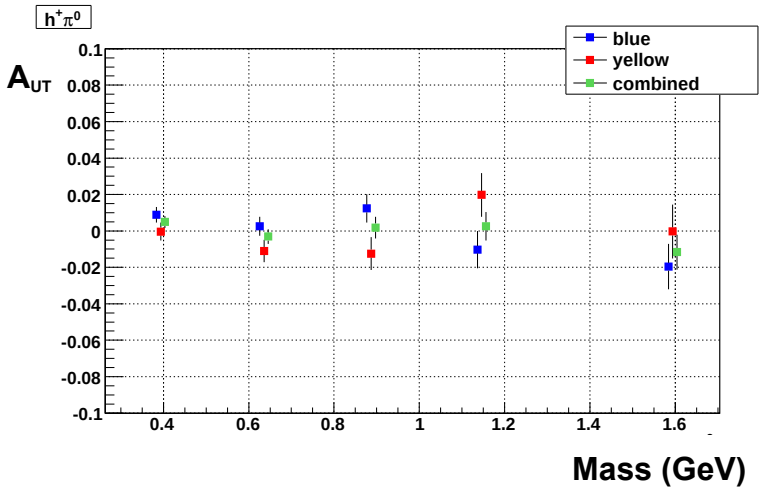

Figure 3.60: Analyzing power for $\pi^0 h^+$ pairs with all fills combined in 5 bins of pair p_T. For blue and yellow beams, and both beams combined.

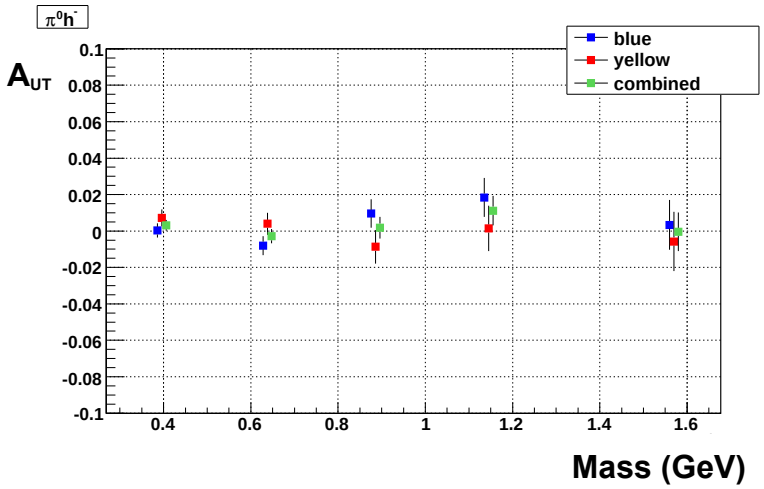

Figure 3.61: Analyzing power for $\pi^0 h^-$ pairs with all fills combined in 5 bins of pair p_T. For blue and yellow beams, and both beams combined.

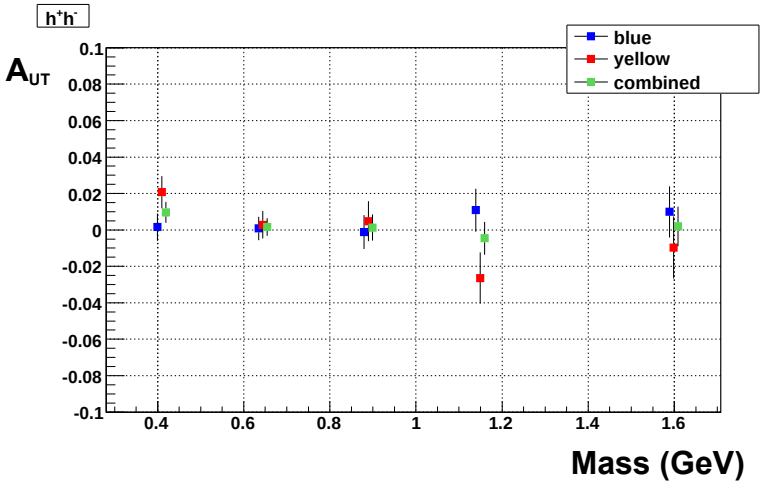

Figure 3.62: Analyzing power for $h^+ h^-$ pairs with all fills combined in 5 bins of pair p_T. For blue and yellow beams, and both beams combined.

then calculated for pairs that have a "π^0" from the side bands and a $h^{+/-}$. Results are shown in Figs. 3.63 and 3.64.

Figure 3.65 compares the asymmetries with for the different hadron pairs with the side band asymmetries.

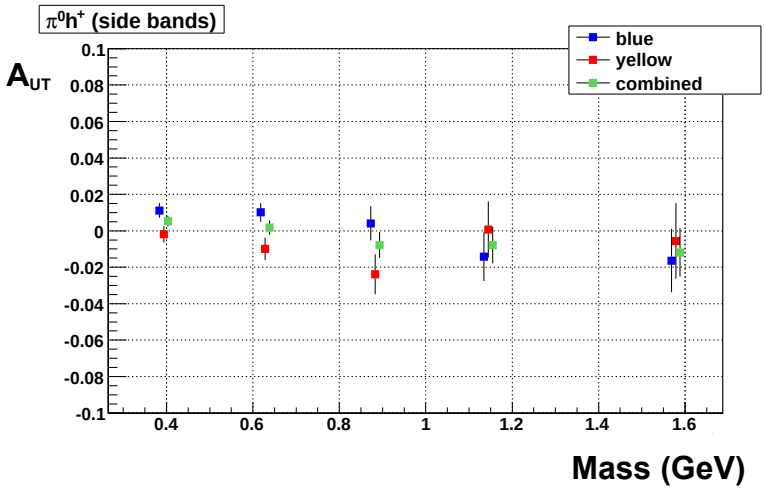

Figure 3.63: Analyzing power for $\pi^0 h^+$ pairs with all fills combined in 5 bins of pair mass (here the "π^0" is from side bands). For blue and yellow beams, and both beams combined.

Di-photon mass spectra are shown for different hadron pair p_T bins in Figs. 3.66 and 3.67. These spectra are then fit with a gaussian plus a second order polynomial to find out the background ratio r in the peak region. The values of r for $\pi^0 h^{+/-}$ pairs in 5 bins of the pair mass are listed in Table 3.16

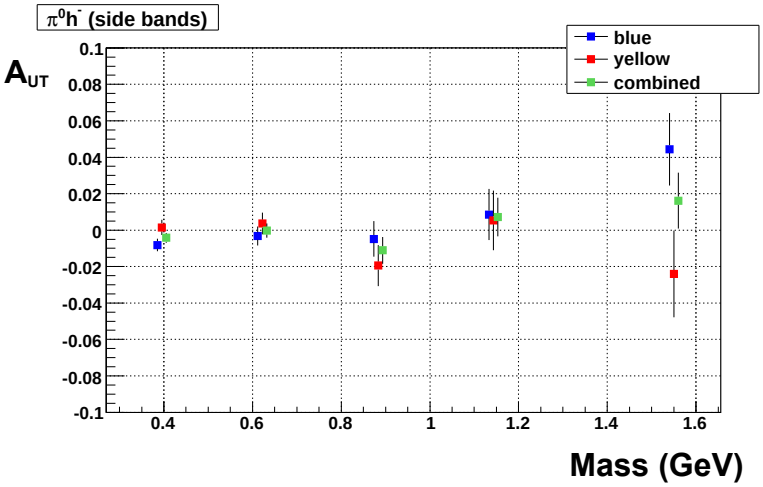

Figure 3.64: Analyzing power for $\pi^0 h^-$ pairs with all fills combined in 5 bins of pair mass (here the "π^0" is from side bands). For blue and yellow beams, and both beams combined.

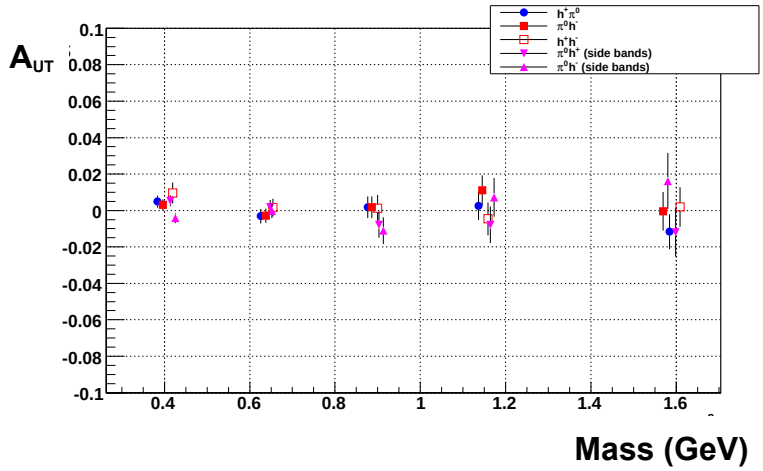

Figure 3.65: Analyzing power in 5 bins of pair p_T.

m bin	0	1	2	3	4
$\pi^0 h^+$	0.72	0.57	0.48	0.44	0.30
$\pi^0 h^-$	0.73	0.58	0.49	0.43	0.30

Table 3.16: Background ratio r under peak region in the di-photon invariant mass spectrum.

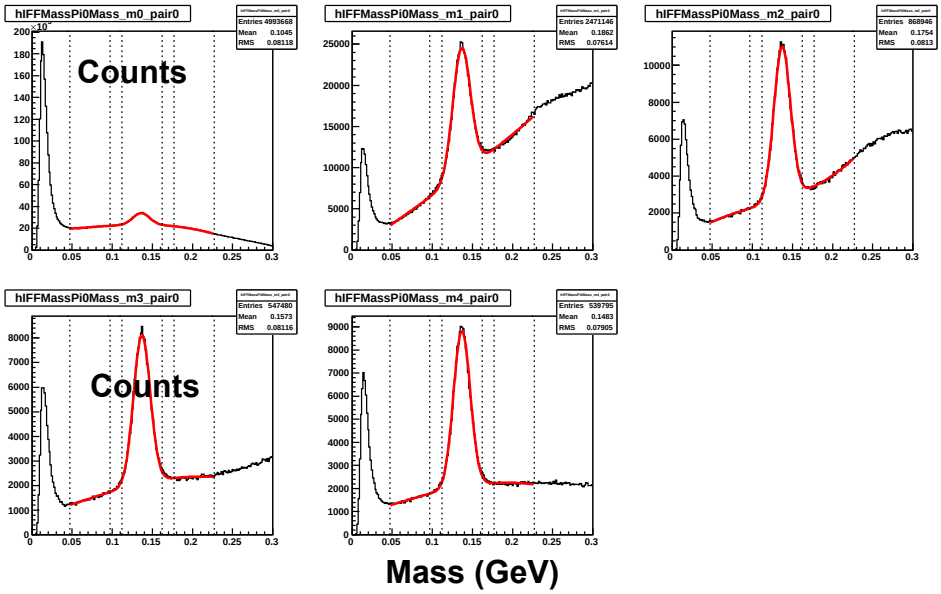

Figure 3.66: Di-photon invariant mass distribution in different ranges of pair p_T. (For $\pi^0 h^+$ pairs)

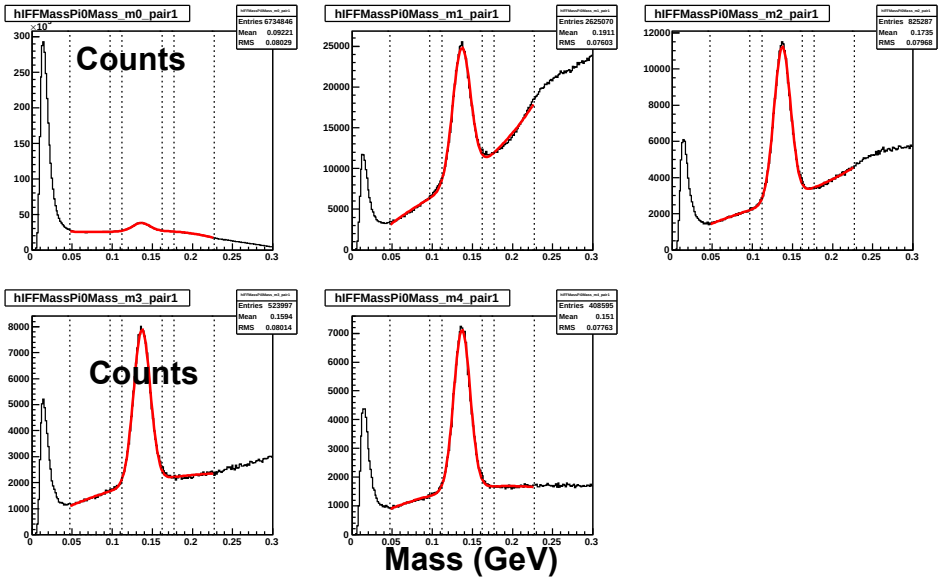

Figure 3.67: Di-photon invariant mass distribution in different ranges of pair p_T. (For $\pi^0 h^-$ pairs)

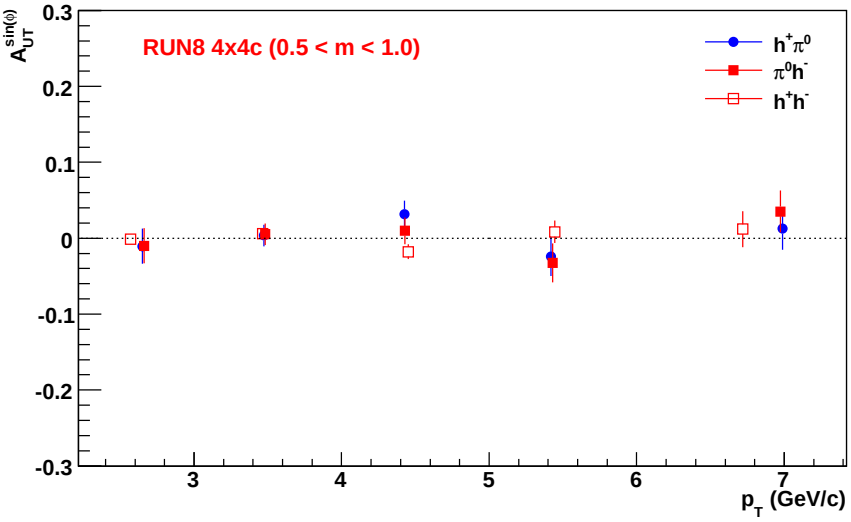

Figure 3.68: Analyzing power for 3 pairs in 5 bins of pair p_T. For $\pi^0 h^+$ and $\pi^0 h^-$ pairs, combinatorial background for π^0 has been subtracted.

p_T bin (GeV/c^2)	$\langle m \rangle$	$A_{UT}^{\sin\phi}$ (comb'd)	stat. err.
2.00 - 3.00	2.650	-0.0106	0.0231
3.00 - 4.00	3.473	0.0035	0.0142
4.00 - 5.00	4.426	0.0318	0.0176
5.00 - 6.00	5.420	-0.0243	0.0258
6.00 - 10.00	6.988	0.0125	0.0275

Table 3.17: Analyzing power for $\pi^0 h^+$ pairs after background subtraction.

p_T bin (GeV/c^2)	$\langle m \rangle$	$A_{UT}^{\sin\phi}$ (comb'd)	stat. err.
2.00 - 3.00	2.651	-0.0100	0.0231
3.00 - 4.00	3.472	0.0052	0.0142
4.00 - 5.00	4.419	0.0096	0.0176
5.00 - 6.00	5.421	-0.0326	0.0258
6.00 - 10.00	6.965	0.0351	0.0275

Table 3.18: Analyzing power for $\pi^0 h^-$ pairs after background subtraction.

p_T bin (GeV/c^2)	$\langle m \rangle$	$A_{UT}^{\sin\phi}$ (comb'd)	stat. err.
2.00 - 3.00	2.549	-0.0011	0.0064
3.00 - 4.00	3.444	0.0060	0.0068
4.00 - 5.00	4.432	-0.0179	0.0098
5.00 - 6.00	5.426	0.0083	0.0147
6.00 - 10.00	6.700	0.0119	0.0236

Table 3.19: Analyzing power for $h^+ h^-$ pairs.

All results shown above are for the transverse momentum dependence of the analyzing power, A_{UT} in the pair invariant mass region from 0.5 to 1.0 GeV/c^2. However, model calculations by Jaffe and collaborators, [28], predict a sign change of the interference fragmentation function at the ρ mass. In order to study the possibility of cancellation of contributions below and above the ρ mass, the p_T dependence is also calculated for two invariant mass bins, one below and one above the ρ mass. The lower mass bin extends from 0.5 to 0.78 GeV/c^2 and the higher mass bin from 0.78 to 1.0 GeV/c^2. The results for the mass bin from 0.5 to 0.78 GeV/c^3 are shown in Fig. 3.69 and Table 3.20, Table 3.21 and Table 3.22. The results for the mass bin from 0.78 to 1.0 GeV/c^2 are shown in Fig. 3.70 and Table 3.23, Table 3.24 and Table 3.25.

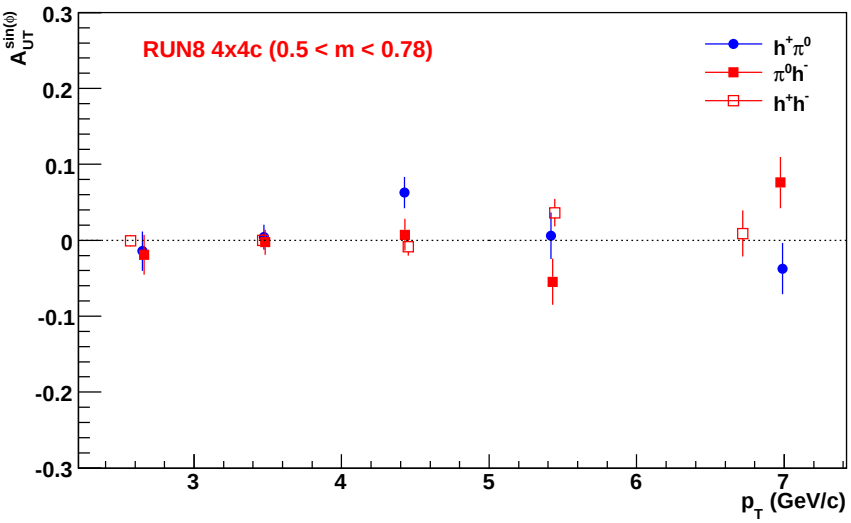

Figure 3.69: Analyzing power for three different hadron pairs in 5 bins of pair p_T. For π^0h^+ and π^0h^- pairs, combinatorial background for π^0 has been subtracted. The invariant mass of the pairs are within the interval 0.5-0.78 GeV/c^2.

p_T bin (GeV/c^2)	$\langle m \rangle$	$A_{UT}^{\sin\phi}$ (comb'd)	stat. err.
2.00 - 3.00	2.650	-0.0143	0.0261
3.00 - 4.00	3.473	0.0041	0.0165
4.00 - 5.00	4.426	0.0628	0.0207
5.00 - 6.00	5.420	0.0058	0.0306
6.00 - 10.00	6.988	-0.0375	0.0337

Table 3.20: Analyzing power for $\pi^0 h^+$ pairs. The invariant mass of the pairs are within the interval 0.5-0.78 GeV/c^2.

p_T bin (GeV/c^2)	$\langle m \rangle$	$A_{UT}^{\sin\phi}$ (comb'd)	stat. err.
2.00 - 3.00	2.651	-0.0193	0.0261
3.00 - 4.00	3.472	-0.0026	0.0165
4.00 - 5.00	4.419	0.0073	0.0207
5.00 - 6.00	5.421	-0.0546	0.0306
6.00 - 10.00	6.965	0.0760	0.0337

Table 3.21: Analyzing power for $\pi^0 h^-$ pairs. The invariant mass of the pairs are within the interval 0.5-0.78 GeV/c^2.

p_T bin (GeV/c^2)	$\langle m \rangle$	$A_{UT}^{\sin\phi}$ (comb'd)	stat. err.
2.00 - 3.00	2.549	-0.0005	0.0075
3.00 - 4.00	3.444	0.0000	0.0082
4.00 - 5.00	4.432	-0.0084	0.0120
5.00 - 6.00	5.426	0.0362	0.0180
6.00 - 10.00	6.700	0.0089	0.0303

Table 3.22: Analyzing power for $h^+ h^-$ pairs. The invariant mass of the pairs are within the interval 0.5-0.78 GeV/c^2.

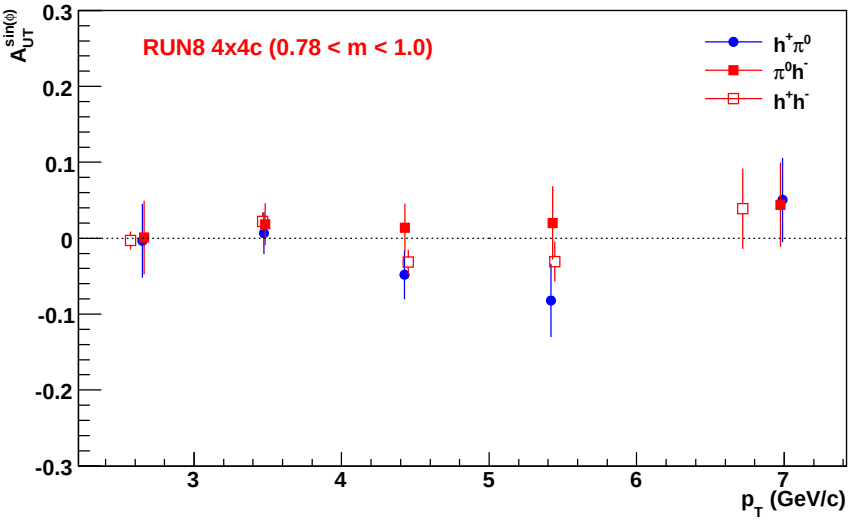

Figure 3.70: Analyzing power for 3 pairs in 5 bins of pair p_T. (For $\pi^0 h^+$ and $\pi^0 h^-$ pairs, combinatorial background for π^0 has been subtracted.) The invariant mass of the pairs are within the interval 0.78-1.0 GeV/c^2.

The same analysis was repeated for 4x4a triggered data sample. Results are shown in Figs. 3.71, 3.72, 3.73.

3.4 Systematic Checks

3.4.1 Bunch Shuffling

Spin asymmetry measurements at polarized colliders allow a unique technique for studying the errors assigned to the asymmetries. The fast succession of

p_T bin (GeV/c^2)	$\langle m \rangle$	$A_{UT}^{\sin\phi}$ (comb'd)	stat. err.
2.00 - 3.00	2.650	-0.0036	0.0487
3.00 - 4.00	3.473	0.0066	0.0276
4.00 - 5.00	4.426	-0.0482	0.0321
5.00 - 6.00	5.420	-0.0819	0.0481
6.00 - 10.00	6.988	0.0504	0.0555

Table 3.23: Analyzing power for $\pi^0 h^+$ pairs. The invariant mass of the pairs are within the interval 0.78-1.0 GeV/c^2.

p_T bin (GeV/c^2)	$\langle m \rangle$	$A_{UT}^{\sin\phi}$ (comb'd)	stat. err.
2.00 - 3.00	2.651	0.0009	0.0487
3.00 - 4.00	3.472	0.0184	0.0276
4.00 - 5.00	4.419	0.0137	0.0321
5.00 - 6.00	5.421	0.0201	0.0481
6.00 - 10.00	6.965	0.0441	0.0555

Table 3.24: Analyzing power for $\pi^0 h^-$ pairs. The invariant mass of the pairs are within the interval 0.78-1.0 GeV/c^2.

p_T bin (GeV/c^2)	$\langle m \rangle$	$A_{UT}^{\sin\phi}$ (comb'd)	stat. err.
2.00 - 3.00	2.549	-0.0030	0.0119
3.00 - 4.00	3.444	0.0221	0.0116
4.00 - 5.00	4.432	-0.0317	0.0163
5.00 - 6.00	5.426	-0.0310	0.0261
6.00 - 10.00	6.700	0.0390	0.0530

Table 3.25: Analyzing power for $h^+ h^-$ pairs. The invariant mass of the pairs are within the interval 0.78-1.0 GeV/c^2.

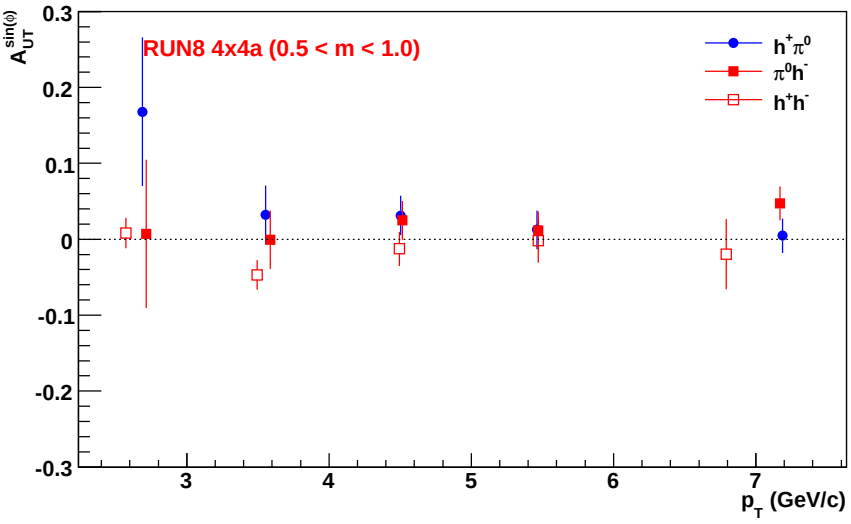

Figure 3.71: Analyzing power for 3 pairs in 5 bins of pair p_T. For $\pi^0 h^+$ and $\pi^0 h^-$ pairs, combinatorial background for π^0 has been subtracted.

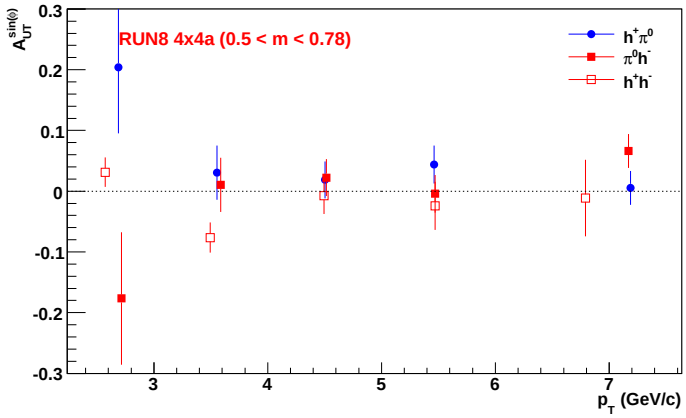

Figure 3.72: Analyzing power for three hadron pairs in 5 bins of pair p_T. For $\pi^0 h^+$ and $\pi^0 h^-$ pairs, combinatorial background for π^0 has been subtracted. The invariant mass of the pairs are within the interval 0.5-0.78 GeV/c^2 for 4x4a triggered sample.

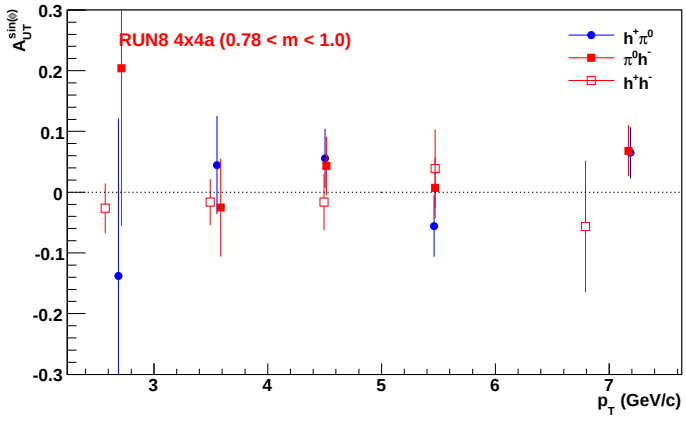

Figure 3.73: Analyzing power for three hadron pairs in 5 bins of pair p_T. For $\pi^0 h^+$ and $\pi^0 h^-$ pairs, combinatorial background for π^0 has been subtracted. The invariant mass of the pairs are within the interval 0.78-1.0 GeV/c^2 for 4x4a triggered sample.

bunch crossings with different spin orientations in a collider eliminates traditional systematic errors in spin asymmetry measurements related to detector stability and acceptance effects. The remaining sources of error are statistical errors and, depending on the asymmetry algorithm used, errors on relative luminosity. The so-called "bunch shuffeling technique" allows to verify the assigned errors and thus probe for the possible presence of unaccounted systematic effects. The test is based on randomly assigning spin patterns to the bunch crossings. Random spin patterns can be chosen to average the beam polarization in the yiels used for the asymmetry calcuation to 0. For a set of random spin patterns the resulting asymmetries will approach a gaussian distribtuion with a mean value of 0 and a width of the assigned error. Deviation in the mean value and the error would indicate the presence of previously undetected systematic effects. Generally, the results from bunch shuffling for $A_{UT}^{\sin\phi}$ confirm the assigned statistical errors and the absence of unknown systematic effects. In this section the results of the bunch shuffling stuides will be presented.

The distributions of the bunch shuffled analyzing powers $A_{UT}^{\sin\phi}$, normalized by the calculated errrors are shwon in Figs. 3.74, 3.75 and 3.76. The results are shown for 5 bins of the pair's invariant mass, and for blue beam and yellow beam. Each distribution is fit with a gaussian function, the mean and the width of the gaussian function are listed in the Tables 3.26, 3.27 and 3.28. Within the errors the means of the bunch shuffled $A_{UT}^{\sin\phi}$ distributions are found to be consistent with 0 and the widths are found to be consistent with 1; confirming the absence of previously undetected systematic effects and the correct evaluation of the errors.

As discussed in the previous section, di-photon pairs from "side bands" are used to evaluate the contribution from combinatorial background from neutral pions in $\pi^0 h^{+/-}$ pairs. In order to probe for possible undetected systematic effects in the side band asymmetries and in order to verify the assigned errors to them, buch shuffling was also carried out for the background asymmetries obtained from the $\pi^0 h^{+/-}$ side bands. The resultes are shown in Figs. 3.77 and 3.78, Tables 3.29 and 3.30. All distributions have mean value close to 0, and width close to 1.

Finally, it was tested that the asymmetries extracted for individual fills are consistent with the overall average asymmetry and that the statistical fluctuations from fill to fill are consistent with Gaussian statistics. For this test for each random spin pattern χ^2 was calculated as

$$\chi^2 = \sum_{i=fills} \left(\frac{A_{UT,i}^{\sin\phi} - \langle A_{UT}^{\sin\phi} \rangle}{\sigma_i} \right)^2. \tag{3.17}$$

The distribution of the variable χ^2 will approach the χ^2 distribution function after repeating the bunch shuffling many times. The probability density for the χ^2 distribution is

$$f(x;k) = \frac{1}{2^{k/2}\Gamma(k/2)} x^{k/2-1} \exp(-x/2). \tag{3.18}$$

The distribution of χ^2 is fit with the following function:

$$g\left(\frac{x}{k}\right) = Af\left(\frac{1}{B^2}\frac{x}{k}; k\right) \tag{3.19}$$

where the parameter k, degree of freedom, is fixed to the number of fills minus 1 in the fitting. A is a normalization factor, B is a scale factor which should be 1 for a perfect χ^2 distribution function.

The distribution for χ^2 from bunch shuffling are shown in Figs. 3.79, 3.80, 3.81, 3.82, and 3.83 for different pairs. The scaling factor B from the fitting is listed in Tables 3.31, 3.32, 3.33, 3.34 and 3.35. All factors are close to 1. This indicates that all errors have been assigned properly to the analyzing power $A_{UT}^{\sin\phi}$.

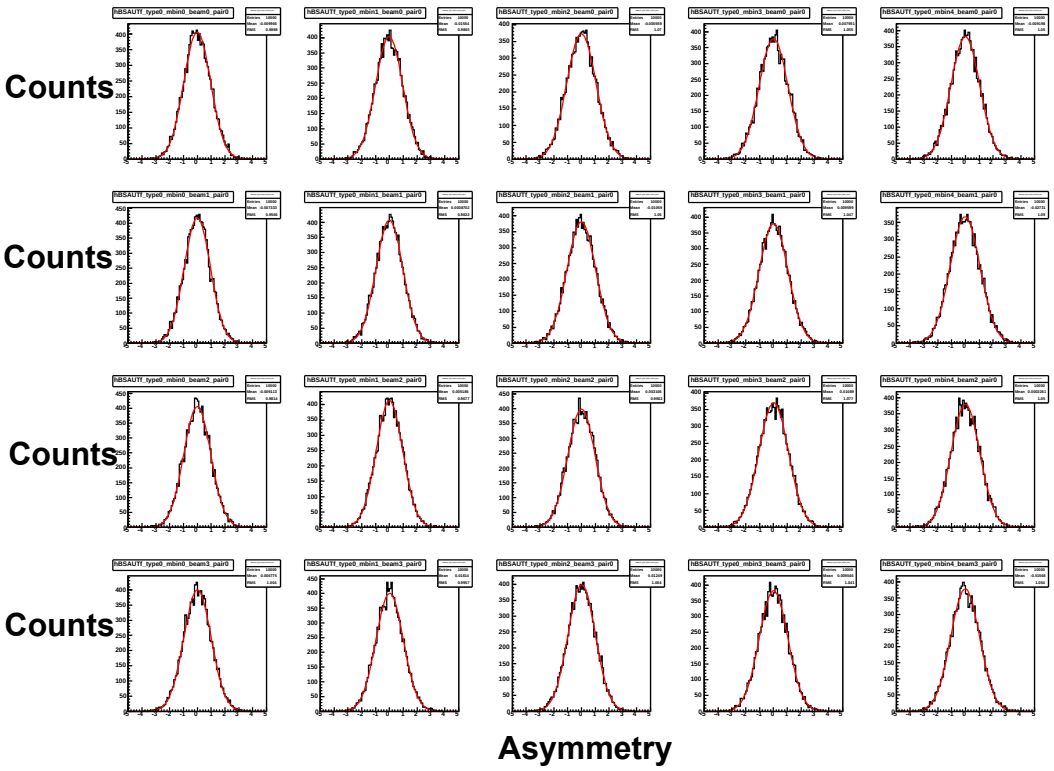

Figure 3.74: Analyzing power from bunch shuffling for $\pi^0 h^+$ pairs.

Beam	m bin	0	1	2	3	4
blue (even)	Mean	-0.008	0.021	0.005	-0.003	-0.018
blue (even)	Width	0.98	0.98	1.06	1.03	1.05
yellow (even)	Mean	-0.006	-0.018	-0.004	0.029	-0.003
yellow (even)	Width	0.95	0.98	1.05	1.03	1.09
blue (odd)	Mean	0.009	0.009	0.021	0.006	0.018
blue (odd)	Width	0.96	0.95	0.98	1.04	1.06
yellow (odd)	Mean	0.018	-0.013	-0.002	-0.020	-0.002
yellow (odd)	Width	0.98	0.98	1.02	1.05	1.05

Table 3.26: Fitting results for the distribution of $A_{UT}^{\sin\phi}$ from bunch shuffling for $\pi^0 h^+$ pairs.

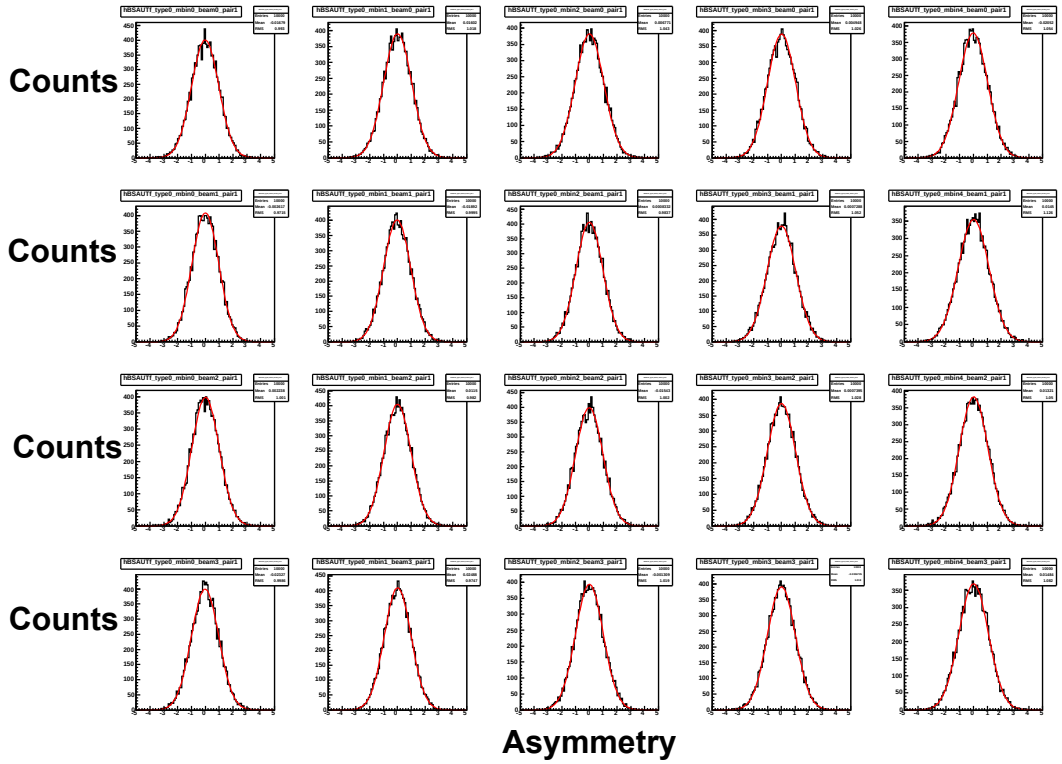

Figure 3.75: Analyzing power from bunch shuffling for $\pi^0 h^-$ pairs.

Beam	m bin	0	1	2	3	4
blue (even)	Mean	0.004	-0.009	-0.009	-0.007	0.006
blue (even)	Width	0.98	1.01	1.05	1.01	1.06
yellow (even)	Mean	-0.005	-0.001	0.008	-0.015	-0.001
yellow (even)	Width	0.96	0.99	1.00	1.03	1.11
blue (odd)	Mean	0.015	0.001	0.002	0.021	-0.002
blue (odd)	Width	0.99	0.96	1.01	1.02	1.05
yellow (odd)	Mean	0.020	-0.006	-0.006	-0.010	-0.017
yellow (odd)	Width	0.98	0.96	1.02	1.02	1.05

Table 3.27: Fitting results for the distribution of $A_{UT}^{\sin\phi}$ from bunch shuffling for $\pi^0 h^-$ pairs.

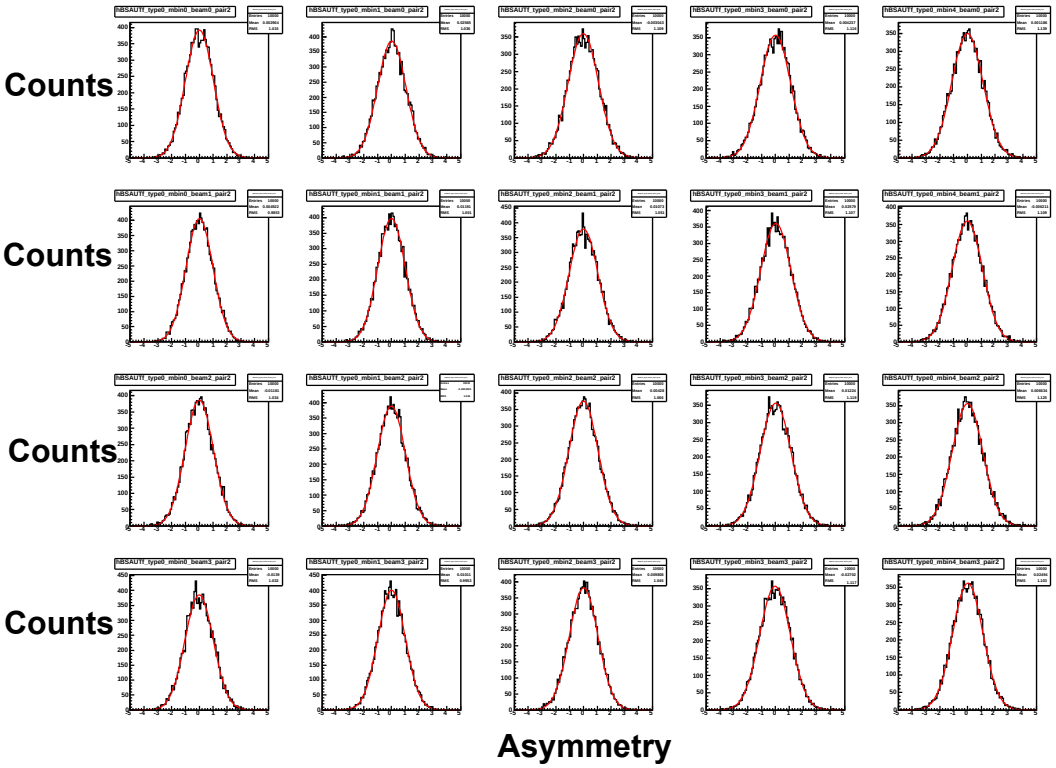

Figure 3.76: Analyzing power from bunch shuffling for h^+h^- pairs.

Beam	m bin	0	1	2	3	4
blue (even)	Mean	-0.003	-0.005	0.003	-0.007	0.011
blue (even)	Width	1.02	1.04	1.10	1.13	1.11
yellow (even)	Mean	-0.014	0.001	0.006	0.001	-0.007
yellow (even)	Width	0.99	1.00	1.04	1.10	1.10
blue (odd)	Mean	0.006	0.007	0.011	0.008	-0.006
blue (odd)	Width	1.02	1.01	1.05	1.12	1.12
yellow (odd)	Mean	-0.003	-0.012	0.013	-0.012	-0.006
yellow (odd)	Width	1.03	1.00	1.04	1.11	1.09

Table 3.28: Fitting results for the distribution of $A_{UT}^{\sin\phi}$ from bunch shuffling for h^+h^- pairs.

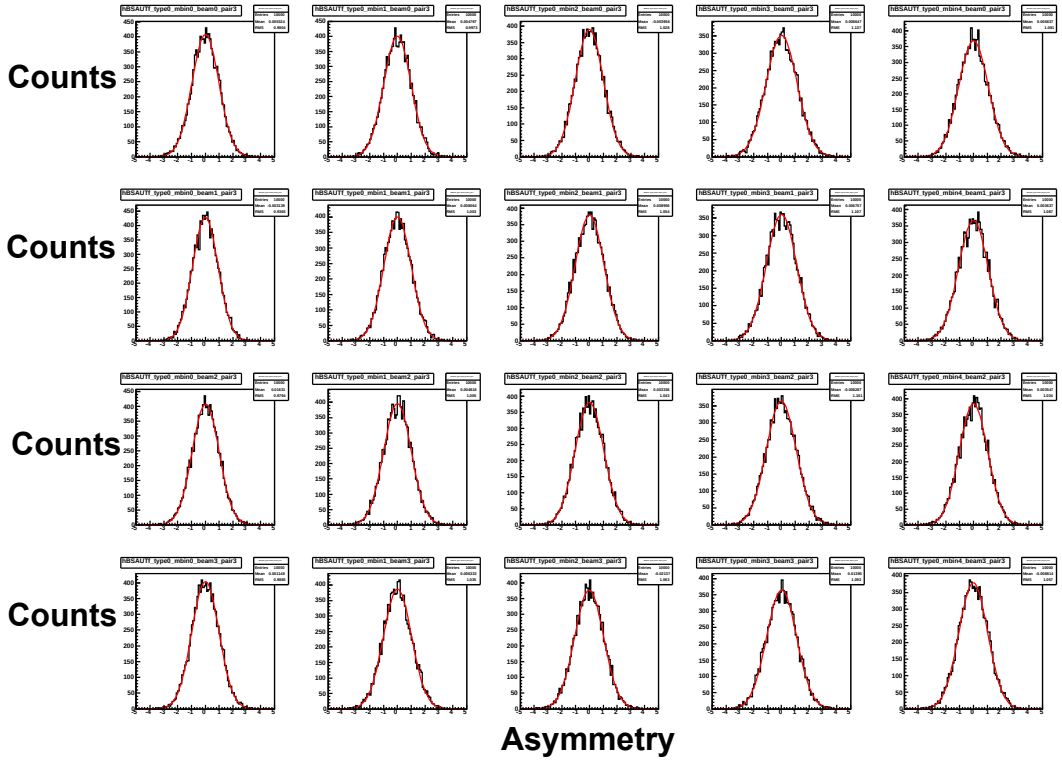

Figure 3.77: Analyzing power from bunch shuffling for $\pi^0 h^+$ pairs. ("π^0" is taken from side bands)

Beam	m bin	0	1	2	3	4
blue (even)	Mean	0.007	0.011	-0.013	-0.026	0.003
blue (even)	Width	0.96	1.00	1.01	1.14	1.07
yellow (even)	Mean	-0.010	-0.007	0.005	-0.003	0.010
yellow (even)	Width	0.94	1.02	1.06	1.10	1.08
blue (odd)	Mean	0.010	0.003	-0.017	-0.014	-0.006
blue (odd)	Width	0.98	1.02	1.02	1.08	1.04
yellow (odd)	Mean	0.001	0.010	0.008	-0.014	0.004
yellow (odd)	Width	1.00	1.02	1.04	1.10	1.03

Table 3.29: Fitting results for the distribution of $A_{UT}^{\sin\phi}$ from bunch shuffling for $\pi^0 h^+$ (side bands) pairs.

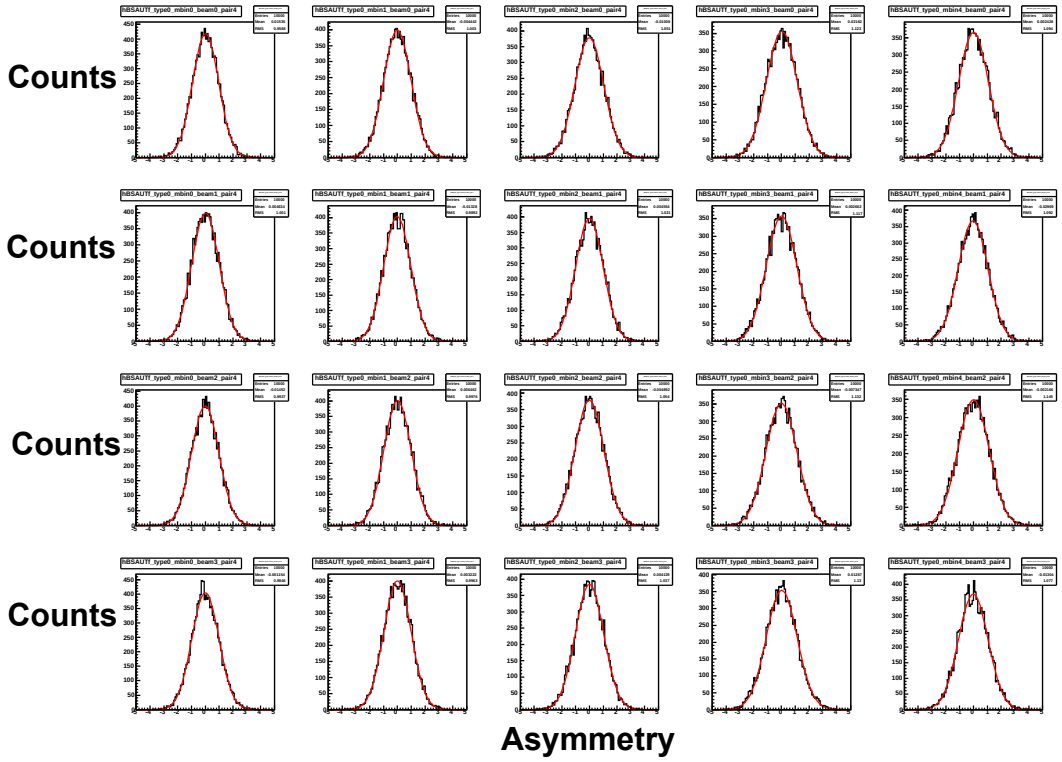

Figure 3.78: Analyzing power from bunch shuffling for $\pi^0 h^-$ pairs. ("π^0" is taken from side bands)

Beam	m bin	0	1	2	3	4
blue (even)	Mean	0.012	0.002	-0.013	0.013	0.003
blue (even)	Width	0.95	0.98	1.04	1.09	1.11
yellow (even)	Mean	0.017	0.010	0.001	-0.000	-0.001
yellow (even)	Width	1.00	0.98	1.01	1.12	1.11
blue (odd)	Mean	0.008	-0.014	0.011	0.002	-0.000
blue (odd)	Width	0.97	0.99	1.04	1.13	1.14
yellow (odd)	Mean	-0.012	-0.008	-0.015	-0.013	0.010
yellow (odd)	Width	0.97	0.99	1.05	1.12	1.08

Table 3.30: Fitting results for the distribution of $A_{UT}^{\sin\phi}$ from bunch shuffling for $\pi^0 h^-$ (side bands) pairs.

Beam	m bin	0	1	2	3	4
blue (even)	Scale	0.999	0.983	1.041	1.049	1.046
yellow (even)	Scale	0.987	0.996	1.040	1.097	1.106
blue (odd)	Scale	0.976	0.985	1.090	1.049	1.045
yellow (odd)	Scale	0.995	1.008	1.041	1.046	1.075

Table 3.31: Results from χ^2 fitting for $\pi^0 h^+$ pairs.

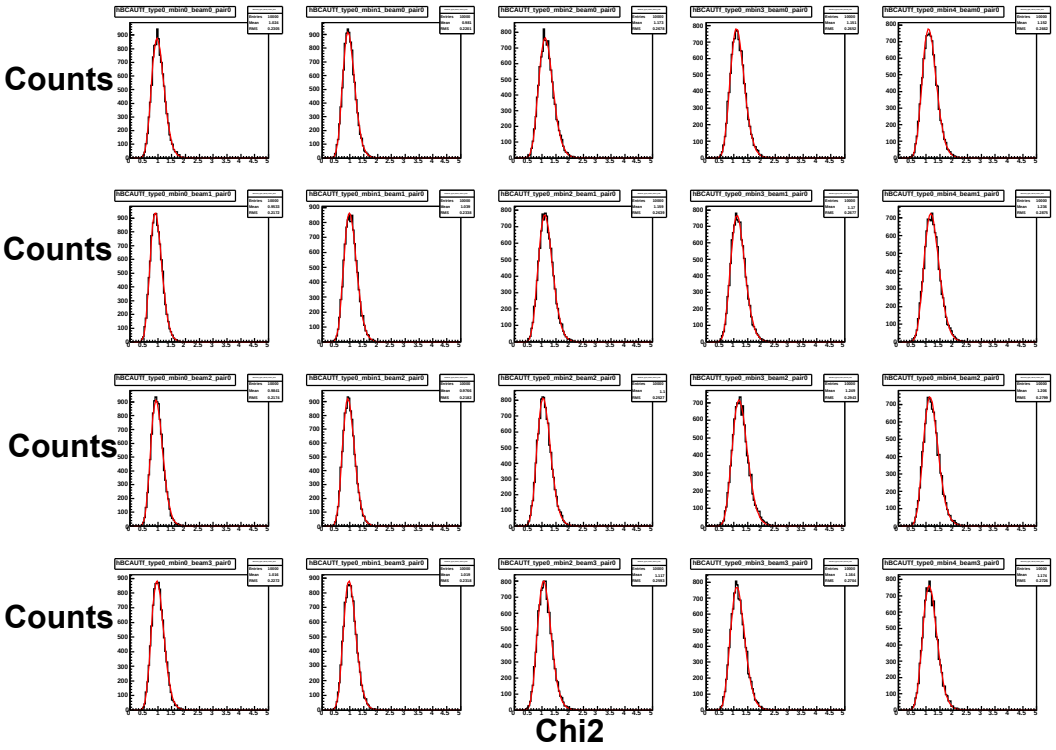

Figure 3.79: χ^2 distribution from bunch shuffling for $\pi^0 h^+$ pairs.

Beam	m bin	0	1	2	3	4
blue (even)	Scale	0.990	1.037	1.102	1.020	1.069
yellow (even)	Scale	0.994	1.008	1.025	1.061	1.060
blue (odd)	Scale	0.995	0.977	1.065	1.040	1.040
yellow (odd)	Scale	1.011	0.994	1.028	1.077	1.043

Table 3.32: Results from χ^2 fitting for $\pi^0 h^-$ pairs.

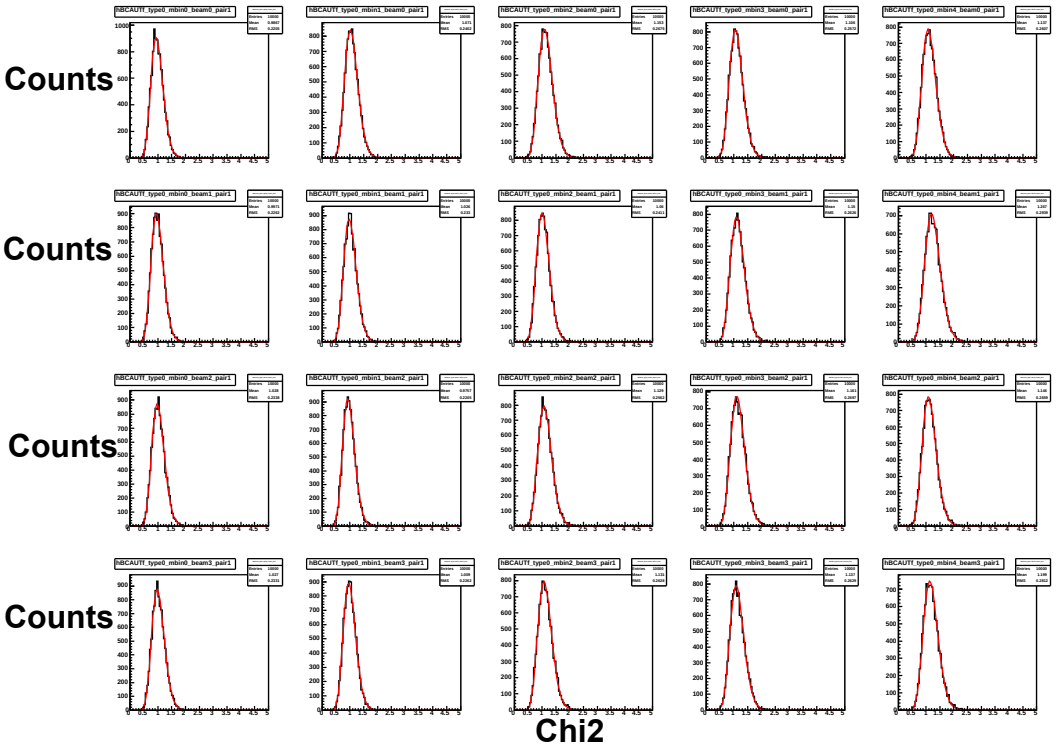

Figure 3.80: χ^2 distribution from bunch shuffling for $\pi^0 h^-$ pairs.

Beam	m bin	0	1	2	3	4
blue (even)	Scale	1.025	1.099	1.138	1.060	1.124
yellow (even)	Scale	1.023	1.072	1.038	1.053	1.115
blue (odd)	Scale	1.039	1.023	1.086	1.055	1.056
yellow (odd)	Scale	1.036	1.024	1.046	1.050	1.051

Table 3.33: Results from χ^2 fitting for h^+h^- pairs.

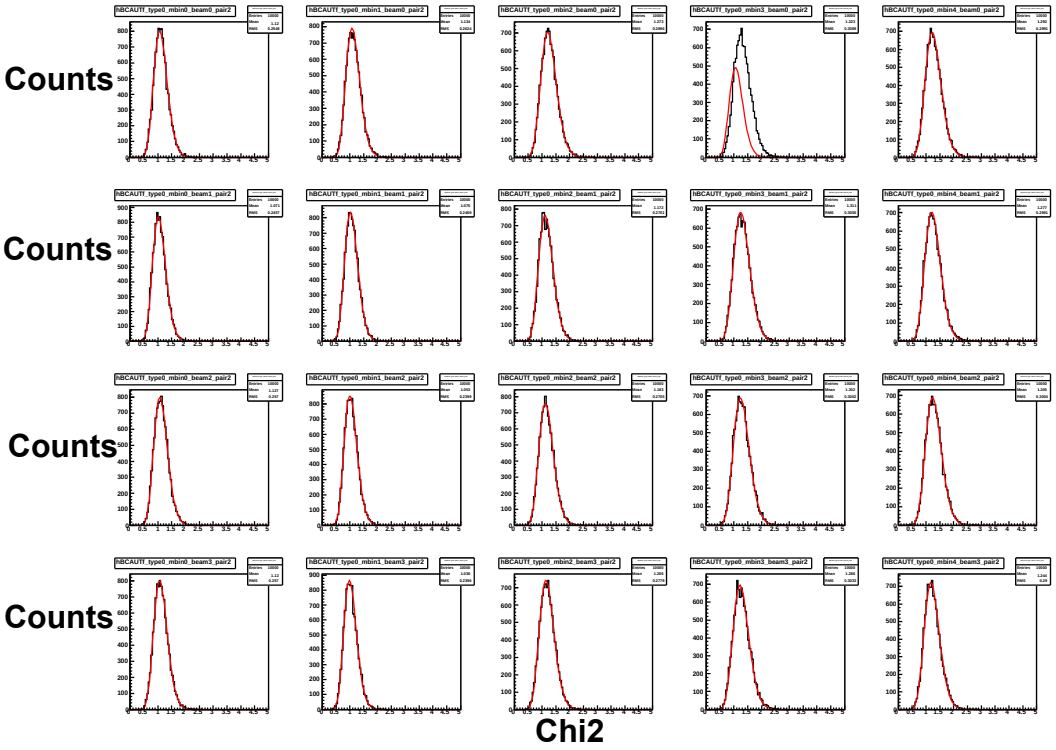

Figure 3.81: χ^2 distribution from bunch shuffling for h^+h^- pairs.

Beam	m bin	0	1	2	3	4
blue (even)	Scale	0.999	1.003	1.028	1.052	1.046
yellow (even)	Scale	0.994	1.051	1.047	1.049	1.048
blue (odd)	Scale	0.978	1.050	1.043	1.051	1.018
yellow (odd)	Scale	1.008	1.023	1.047	1.049	1.078

Table 3.34: Results from χ^2 fitting for π^0h^+ (side bands) pairs.

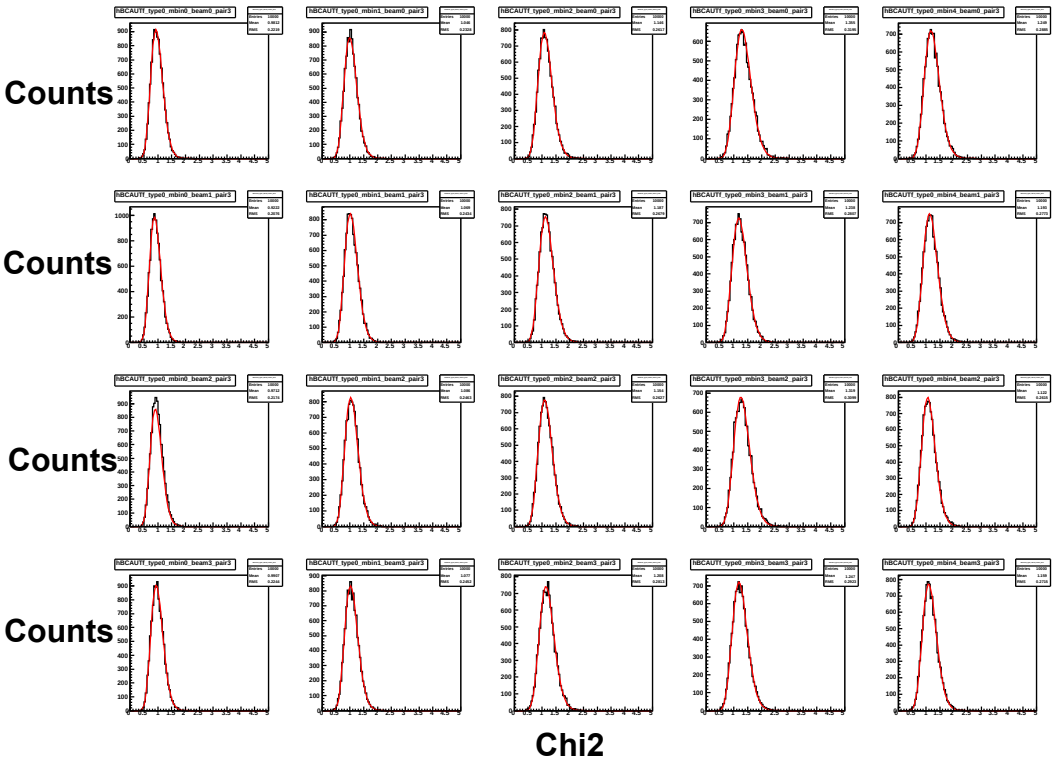

Figure 3.82: χ^2 distribution from bunch shuffling for $\pi^0 h^+$ pairs. ("π^0" are taken from the side bands.)

Beam	m bin	0	1	2	3	4
blue (even)	Scale	0.975	1.006	1.040	1.134	1.117
yellow (even)	Scale	0.984	0.998	1.067	1.102	1.048
blue (odd)	Scale	0.994	1.017	1.043	1.047	1.055
yellow (odd)	Scale	0.995	1.022	1.110	1.052	1.050

Table 3.35: Results from χ^2 fitting for $\pi^0 h^-$ (side bands) pairs.

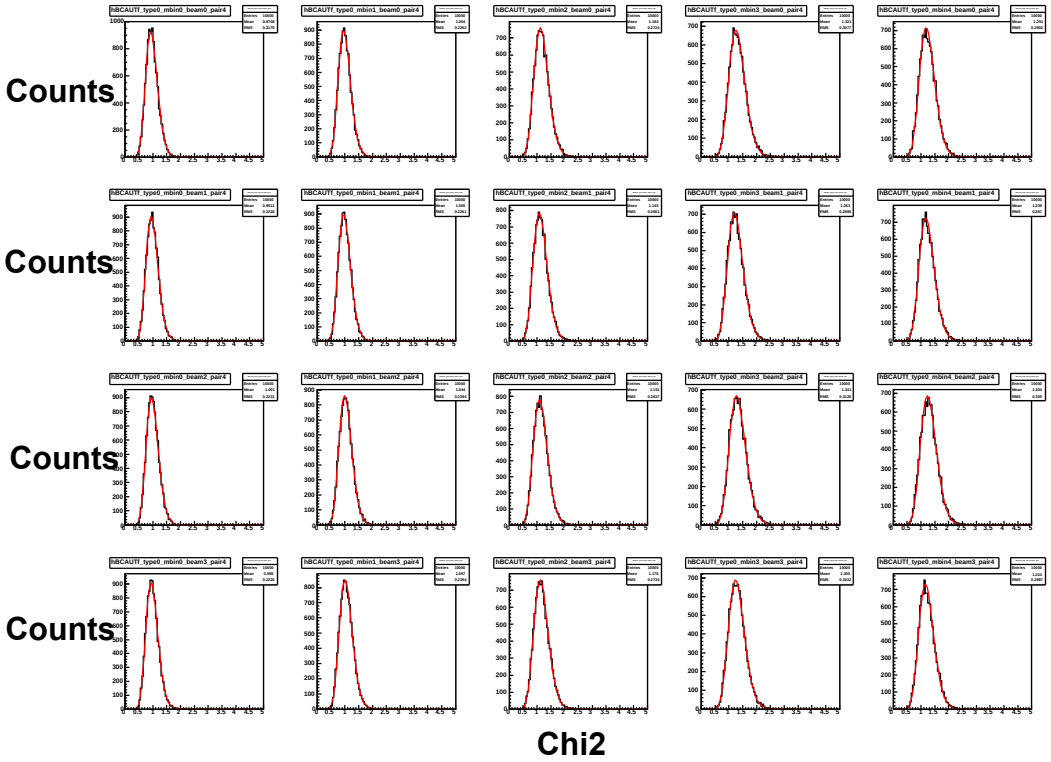

Figure 3.83: χ^2 distribution from bunch shuffling for $\pi^0 h^-$ pairs. ("π^0" are taken from the side bands.)

3.4.2 Analyzing Power Calculated from Mixed Events

Event mixing can be done by taking two hadrons from different events to form the pairs. This completely eliminates possible physics asymmetries and therefore provides an alternative way to detect possible non-physical bias in the measured asymmetries. The analyzing power calculated from mixed events are shown in Fig. 3.84. The analyzing powers are consistent with 0.

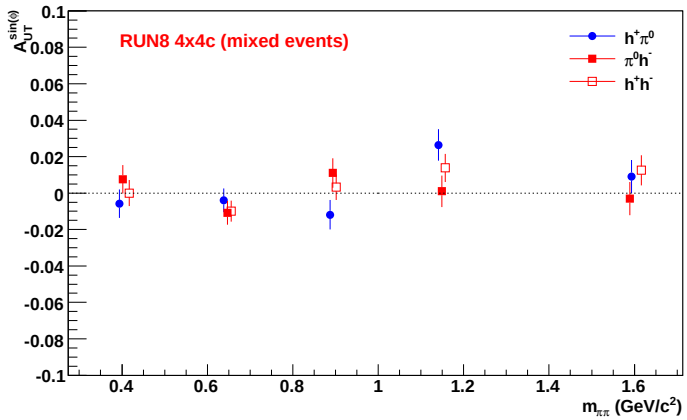

Figure 3.84: Mixed events: analyzing power $A_{UT}^{\sin\phi'}$ for 3 pairs in 5 bins of pair mass.

3.4.3 Distribution of the ϕ Angle

The angle ϕ used in this analysis has been defined in the previous section as $\phi = \phi_{R_C} - \phi_{S_B}$. The distribution of ϕ from real data is shown in Fig. 3.35. The shape of the distribution results from the limited acceptance of the PHENIX central arm.

A simple Monte Carlo was used to understand this distribution. First, a sample of random unit vectors are generated, their directions are distributed

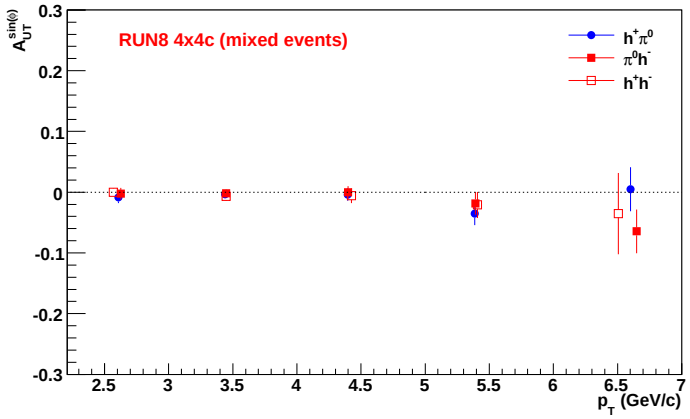

Figure 3.85: Mixed events: analyzing power $A_{UT}^{\sin\phi'}$ for 3 pairs in 5 bins of pair p_T.

uniformly in 4π. Then, every two of them are used as the momenta of two hadrons. The angles ϕ_{R_C} and ϕ_{S_B} are calculated following exactly the same method as used in the analysis. The distributions of ϕ_{R_C}, ϕ_{S_B} and ϕ are shown in the three columns of Fig. 3.86. The first row shows the distributions with no acceptance cut, the second row shows the distributions after applying a limit of azimuthal acceptance, and the third row shows the distributions with limits on both azimuthal acceptance and rapidity coverage.

As mentioned in the previous section, the angle ϕ_{S_B} is the angle from the polarization vector to the scattering plane. The orientation of the scattering plane is limited by the west and east arm's geometric acceptance in the azimuthal direction. Since during Run-6 the proton beam polarization vector was in the radial direction, ϕ_{S_B} will not have a uniform distribution but peaks at around 0 and π. The distribution of ϕ_{S_B} for different geometric acceptance is demonstrated by the Monte Carlo as shown in the first column in Fig. 3.86.

In addition, ϕ_{R_C} is the angle from the scattering plane to the hadron plane. For a detector with 4π acceptance, the distribution of ϕ_{R_C} should be uniform. However, if there is a limit on the azimuthal acceptance such as PHENIX central arm, the distribution will peak at 0 and π. The limited

rapidity coverage of PHENIX central arm also needs to be considered. After applying limits on both azimuthal coverage and rapidity coverage, the distribution of ϕ_{R_C} peaks at $\pm\pi/2$. The distribution of ϕ_{R_C} for different geometric acceptance from simple Monte Carlo is shown in the second column in Fig. 3.86. The shape of the distribution of ϕ indicates that vertical beam polarization leads to higher analyzing power than radial polarization since the analyzing power to be measured comes from a $\sin\phi$ modulation.

Since the ϕ angle is defined as $\phi = \phi_{S_B} - \phi_{R_C}$, the distribution of ϕ can be derived from the distributions of ϕ_{S_B} and ϕ_{R_C}. The Monte Carlo result is shown in Fig. 3.86. The distribution of ϕ peaks at around $\pm\pi/2$. This matches the distribution shown in Fig. 3.35 from real data.

Although the distribution of ϕ is not uniform, no significant effects from detector acceptance have been found in calculating the analyzing power. The reason is that the single spin asymmetry is calculated as a function for ϕ. From Eq. 3.8 the acceptance term should cancel out cancel out as long as the acceptance does not depend on the spin states.

During the 2008 running at PHENIX interaction point, the spin orientation was vertical while during 2006 running, the spin orientation was radial. Given the same number of events in the data sample, different orientations give different statistical uncertainties for measured asymmetry.

A toy Monte Carlo is used to demonstrate the effect of different polarization orientations on the calculated asymmetries and their errors. An arbitrary asymmetry is used as input, then the kinematics for each pair is weighted with the $\sin\phi$ value for the pair. The asymmetry is then reconstructed, observing the PHENIX acceptance.

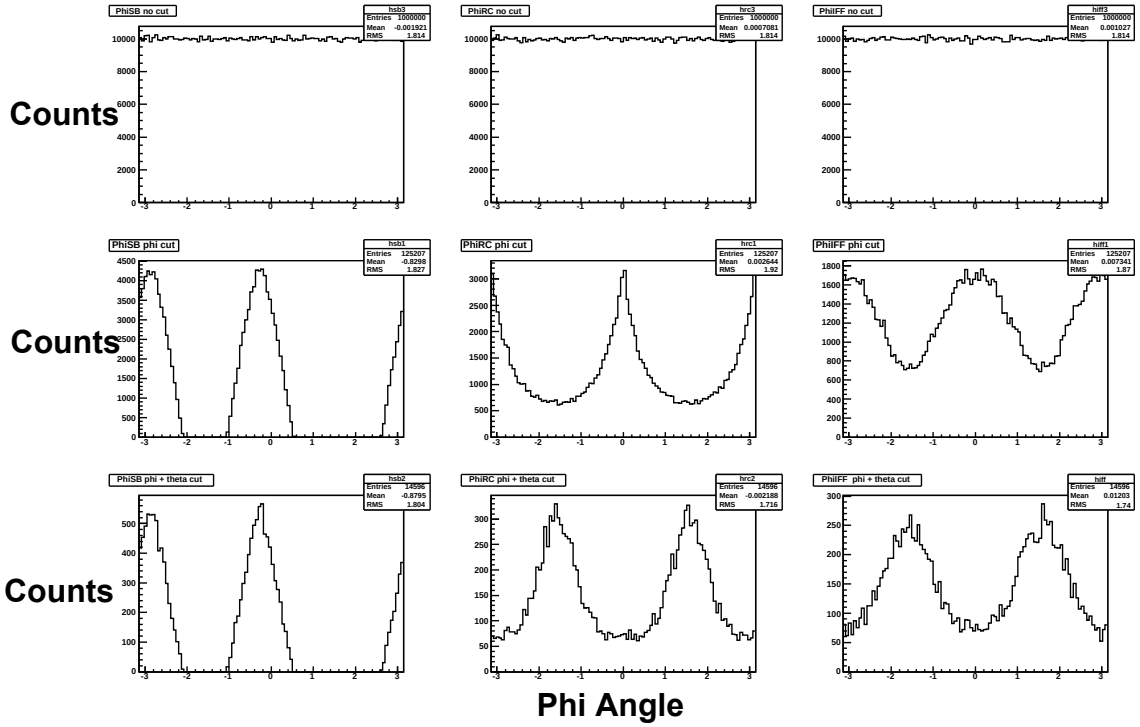

Figure 3.86: Distributions of ϕ_{R_C}, ϕ_{S_B} and ϕ from a simple Monte Carlo are shown in the three columns. The first row shows the distributions with no acceptance cut, the second row shows the distributions after applying a limit of azimuthal acceptance, and the third row shows the distributions with limits on both azimuthal acceptance and rapidity coverage.

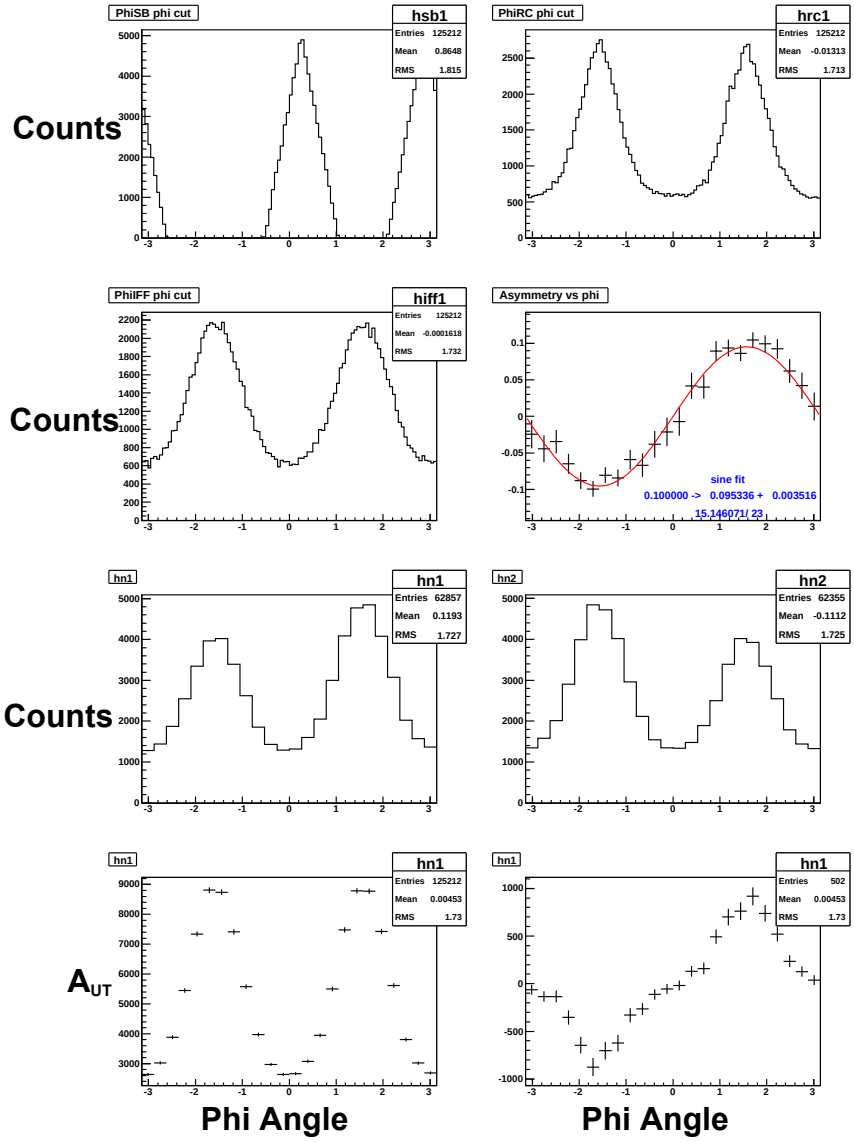

Figure 3.87: Toy MC study of asymmetry reconstruction for a known radial input asymmetry of 0.1. The first three plots show the angular distributions for ϕ_{SB}, ϕ_{RC} and ϕ. The fourth plot shows the reconstructed asymmetry as a function of ϕ, fitted with a sin-function. Shown on this plot are the numbers for the input asymmetry (0.1), the reconstructed asymmetry (0.103), the error (0.0048), the χ^2 and the number of degrees of freedom for the fit. The MC study demonstrates that the input asymmetry is extracted correctly.

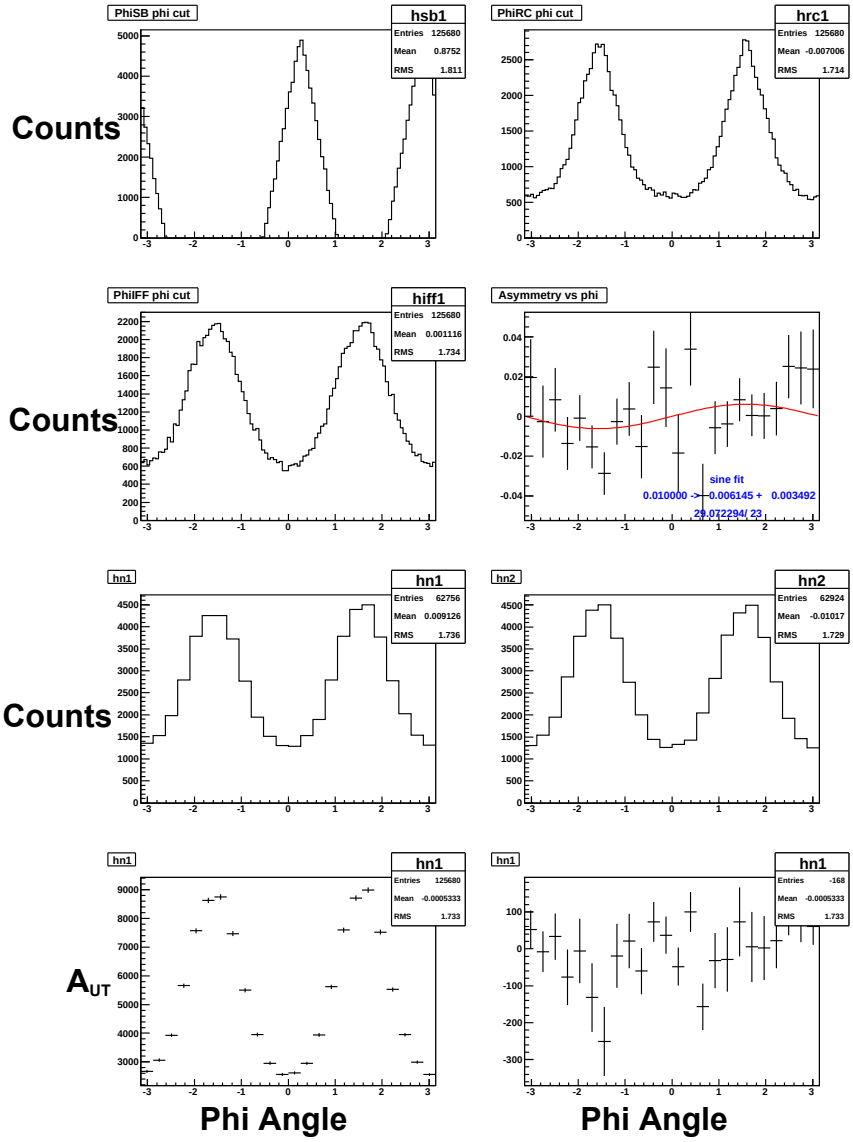

Figure 3.88: Toy MC study of asymmetry reconstruction for a known radial input asymmetry of 0.01. The first three plots show the angular distributions for ϕ_{SB}, ϕ_{RC} and ϕ. The fourth plot shows the reconstructed asymmetry as a function of ϕ, fitted with a sin-function. Shown on this plot are the numbers for the input asymmetry, the reconstructed asymmetry, the error, the χ^2 and the number of degrees of freedom for the fit. The MC study demonstrates that the input asymmetry is extracted correctly.

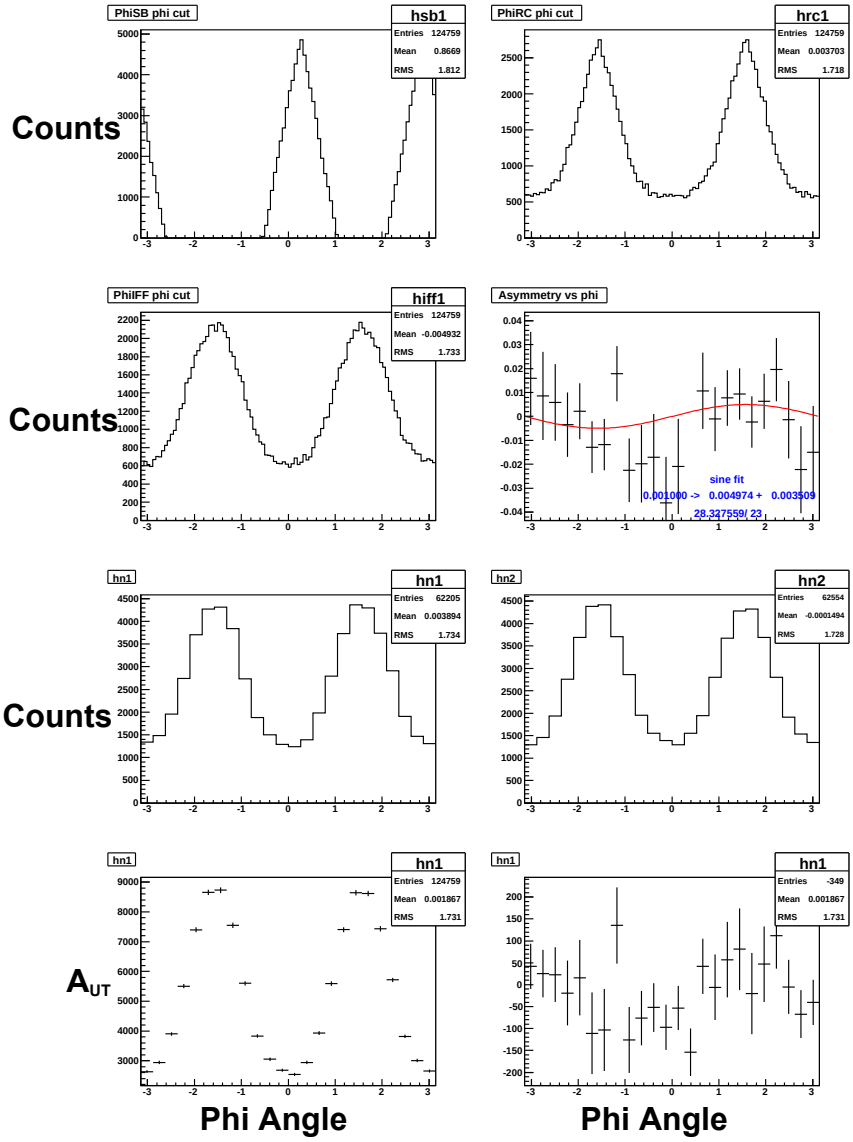

Figure 3.89: Toy MC study of asymmetry reconstruction for a known radial input asymmetry of 0.001. The first three plots show the angular distributions for ϕ_{SB}, ϕ_{RC} and ϕ. The fourth plot shows the reconstructed asymmetry as a function of ϕ, fitted with a sin-function. Shown on this plot are the numbers for the input asymmetry, the reconstructed asymmetry, the error, the χ^2 and the number of degrees of freedom for the fit. The MC study demonstrates that the input asymmetry is extracted correctly.

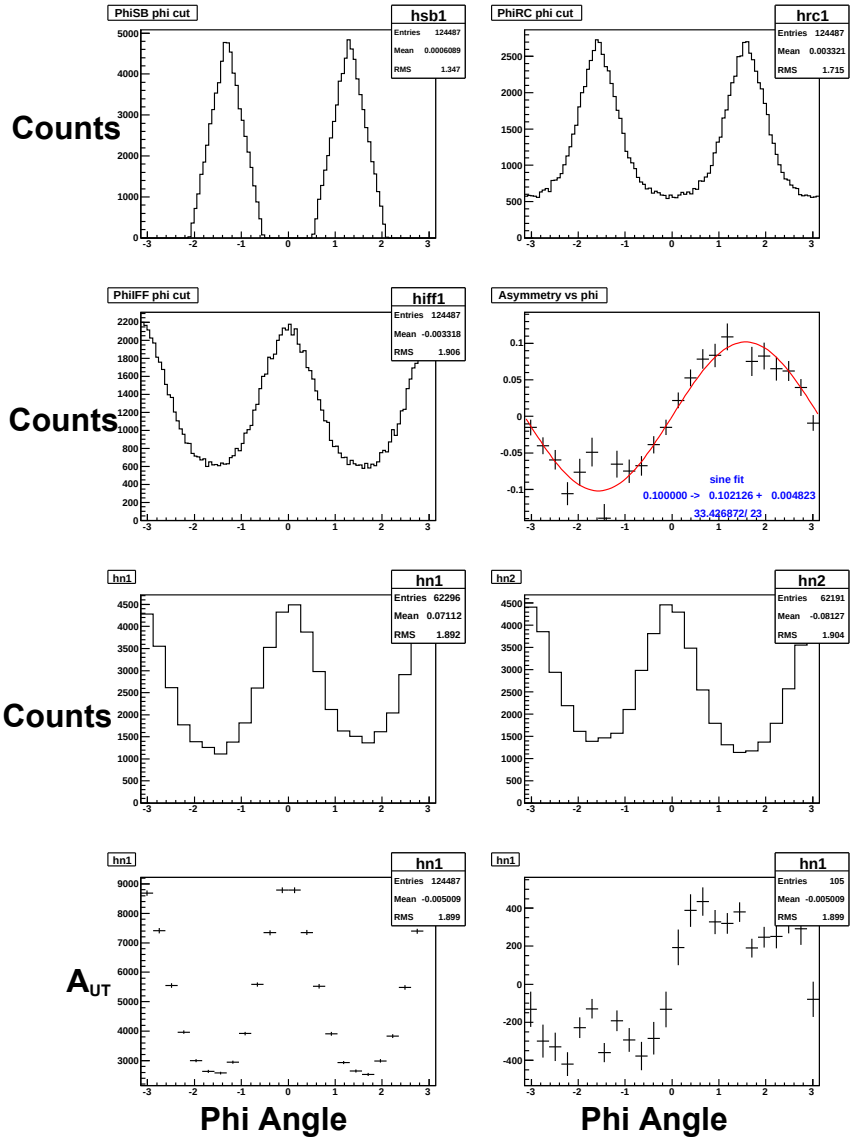

Figure 3.90: Toy MC study of asymmetry reconstruction for a known vertical input asymmetry of 0.1. The first three plots show the angular distributions for ϕ_{SB}, ϕ_{RC} and ϕ. The fourth plot shows the reconstructed asymmetry as a function of ϕ, fitted with a sin-function. Shown on this plot are the numbers for the input asymmetry, the reconstructed asymmetry, the error, the χ^2 and the number of degrees of freedom for the fit. The MC study demonstrates that the input asymmetry is extracted correctly.

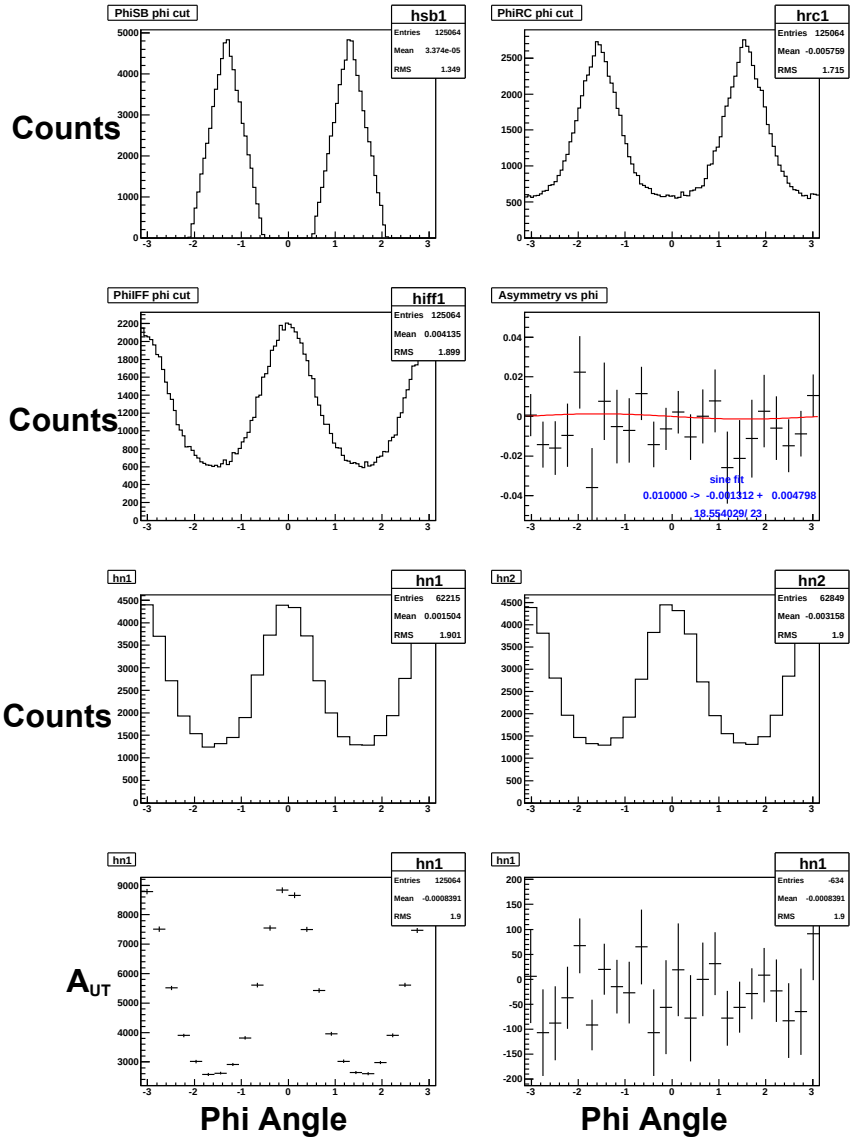

Figure 3.91: Toy MC study of asymmetry reconstruction for a known vertical input asymmetry of 0.01. The first three plots show the angular distributions for ϕ_{SB}, ϕ_{RC} and ϕ. The fourth plot shows the reconstructed asymmetry as a function of ϕ, fitted with a sin-function. Shown on this plot are the numbers for the input asymmetry, the reconstructed asymmetry, the error, the χ^2 and the number of degrees of freedom for the fit. The MC study demonstrates that the input asymmetry is extracted correctly.

input	reconstructed (vertical)	reconstructed (radial)
0.1000	0.1021 ± 0.0048	0.0953 ± 0.0035
0.0100	-0.0013 ± 0.0047	0.0061 ± 0.0034
0.0010	-0.0025 ± 0.0047	0.0049 ± 0.0035

Table 3.36: Comparison of input and reconstructed asymmetries for a toy Monte Carlo used to study the impact of PHENIX acceptance and the orientation of the proton polarization.

Table 3.36 shows the input asymmetries and reconstructed asymmetries and their errors. The ratio of statistical uncertainties of vertical polarization to that of radial polarization is 0.0048/0.0035=1.37 for the same number of events.

3.4.4 Testing for the Presence of other Angular Modulations

In the previous sections, we have focused on the $\sin\phi$ modulation of the single spin asymmetry. As a cross check, $\cos\phi$ modulation is also calculated. The analyzing powers $A_{UT}^{\cos\phi}$ are shown in Fig. 3.93 in 5 bins of pair mass, and they are all consistent with 0.

When calculating the $\sin\phi$ and $\cos\phi$ modulations, $\phi = \phi_{S_B} - \phi_{R_C}$. It would be interesting to also test for the presence of modulations $\sin\phi'$ and $\cos\phi'$ for the angle $\phi' = \phi_{S_B} + \phi_{R_C}$. The motivation for this check comes from

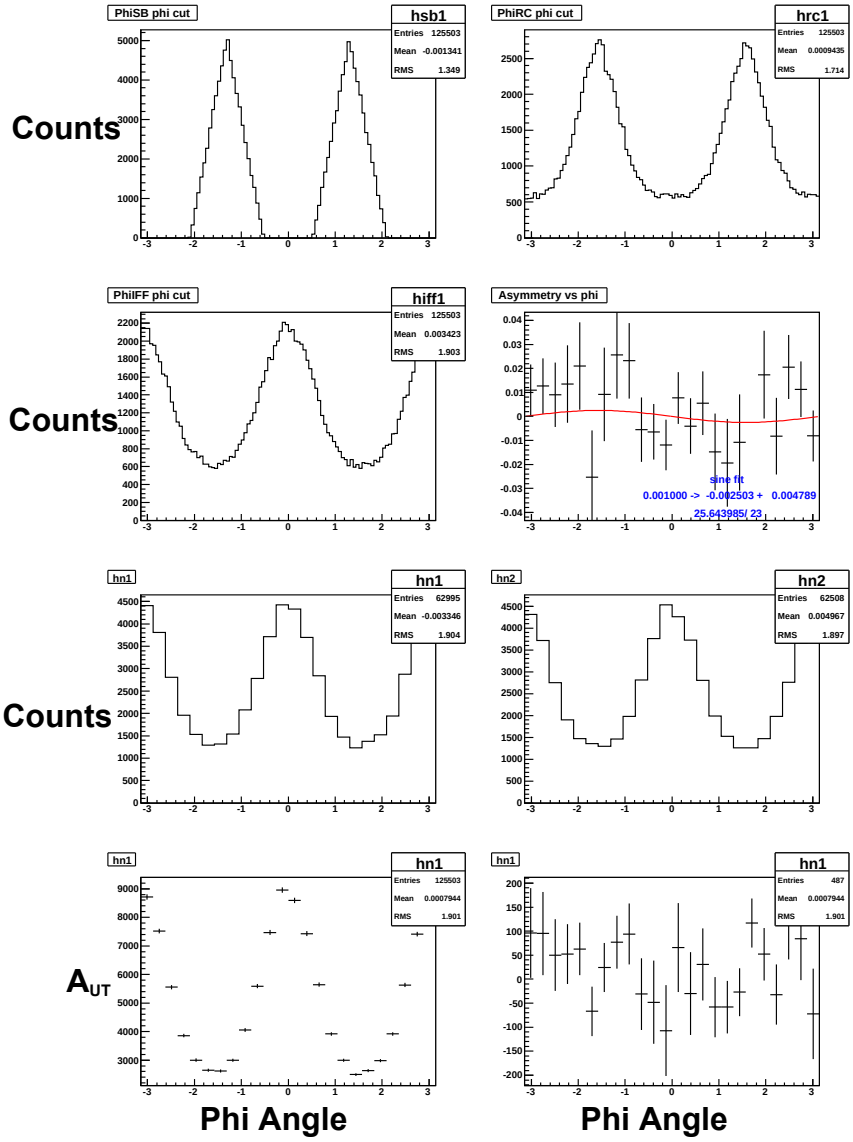

Figure 3.92: Toy MC study of asymmetry reconstruction for a known vertical input asymmetry of 0.001. The first three plots show the angular distributions for ϕ_{SB}, ϕ_{RC} and ϕ. The fourth plot shows the reconstructed asymmetry as a function of ϕ, fitted with a sin-function. Shown on this plot are the numbers for the input asymmetry, the reconstructed asymmetry, the error, the χ^2 and the number of degrees of freedom for the fit. The MC study demonstrates that the input asymmetry is extracted correctly.

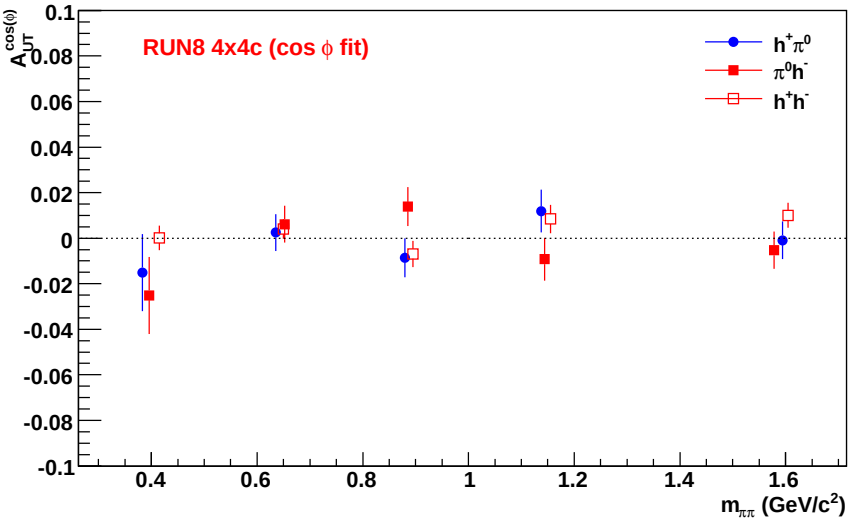

Figure 3.93: Analyzing power $A_{UT}^{\cos\phi}$ for three different hadron pairs in 5 bins of pair mass. (fitting with $\cos\phi$ function.)

the measurement of the Collins effect and the Sivers effect in semi-inclusive deep in-elastic scattering experiment where the two effects have modulation such as $\sin(\phi_h + \phi_S)$ and $\sin(\phi_h - \phi_S)$ respectively [25].

The analyzing powers for $\sin\phi'$ and $\cos\phi'$ are shown in Figs. 3.94 and 3.95 for 5 bins of pair mass. All analyzing powers are consistent with 0.

3.4.5 Different Binning of the Azimuthal Angle

In the previous sections, the single spin asymmetry has been calculated in 24 bins of ϕ for the range of $(-\pi, \pi]$. To test the effect on the results from ϕ binning, the calculation is repeated using 12 bins of the angle ϕ.

The results are shown in Fig. 3.96. Compared to results in Fig. 3.52, there is no significant difference.

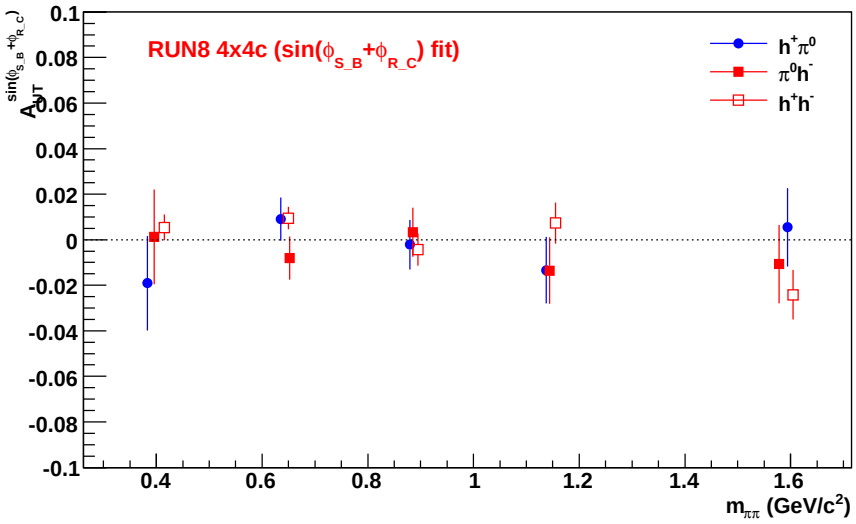

Figure 3.94: Analyzing power $A_{UT}^{\sin\phi'}$ for three different hadron pairs in 5 bins of pair mass.

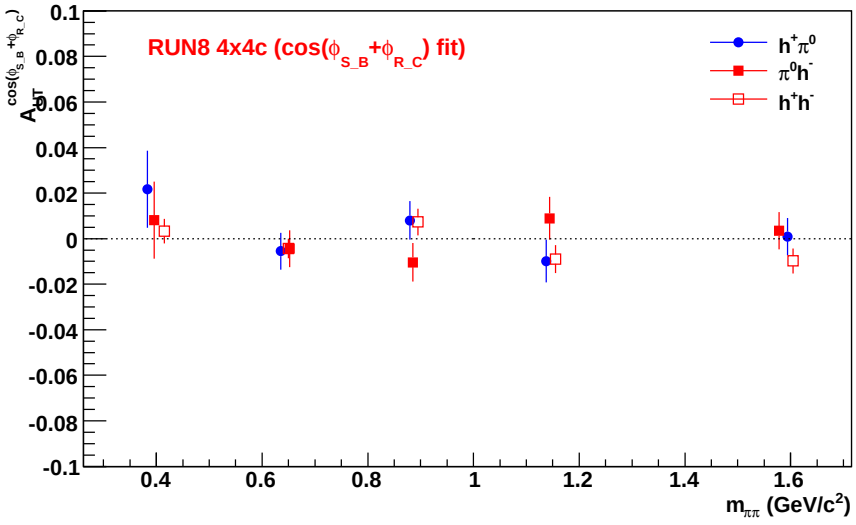

Figure 3.95: Analyzing power $A_{UT}^{\cos\phi'}$ for three different hadron pairs in 5 bins of pair mass.

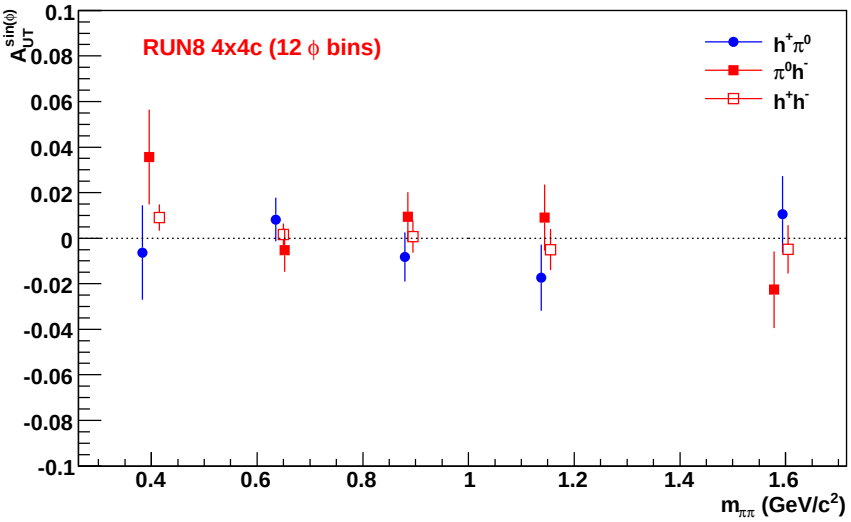

Figure 3.96: Analyzing power $A_{UT}^{\sin\phi}$ for 3 pairs in 5 bins of pair mass. (Using 12 bins of ϕ instead of 24 bins)

3.4.6 Calculating the Asymmetry without Relative Luminosity

As shown in Eq. 3.8, to calculate the single spin asymmetry, the counts of hadron pairs for two different spin states are normalized by relative luminosity. Since the single spin asymmetry is calculated as a function of ϕ, there is another way to calculate the analyzing power without relying on relative luminosity.

The raw asymmetry is defined as

$$A_{UT}(\phi) = \frac{1}{P}\frac{N_\uparrow(\phi) - N_\downarrow(\phi)}{N_\uparrow(\phi) + N_\downarrow(\phi)}. \tag{3.20}$$

The definition of the variables are the same as in Eq. 3.8. The difference between the asymmetry in Eq. 3.20 and Eq. 3.8 is a constant term ($\sim (1-R)/(1+R)$ when the asymmetry $\ll 1$). Therefore, to extract the analyzing power from $A_{UT}(\phi)$, a function $B + A\sin\phi$ is used instead of $A\sin\phi$ used in the previous section. The analyzing power calculated with this method is

shown in 3.97. Compared to results in Fig. 3.52, no significant difference has been found.

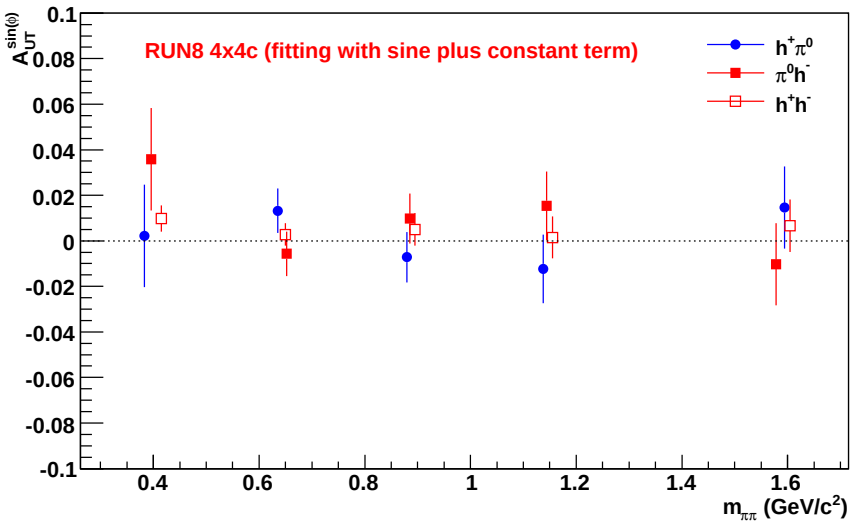

Figure 3.97: Analyzing power for three different hadron pairs as a function of mass of the pair. Relative luminosity is not used here, and the fitting function is $B + A \sin \phi$.

3.4.7 Comparing Forward and Backward Asymmetries

As an additional cross check, the data sample can be separated into hadron pairs emitted in the forward direction and pairs emited in the backward direction. Transversity asymmetries are dominated by contributions from valence quarks and therefore forward pairs should see larger asymmetries given enough statistics.

The forward pairs are defined as the pairs going along the same direction as the "polarized" proton (in the actual experiment, both beams are polarized, but when calculating the single spin asymmetry, one usually assumes that one beam is polarized, and the other beam's polarization averages out

therefore is approximately zero, see the discussion on residual polarization in the next section).

The results for forward and backward pairs are shown in Figs. 3.98 and 3.99 as a function of invariant mass, and in Figs. 3.100 and 3.101 as a function of p_T.

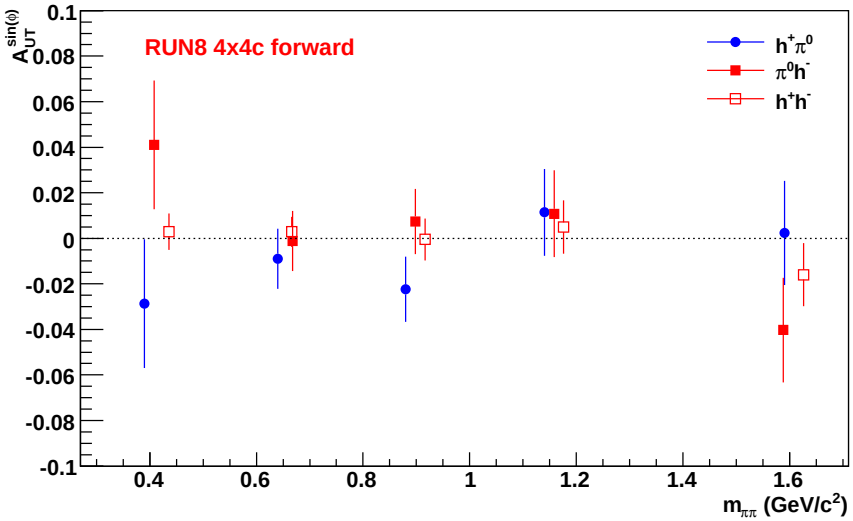

Figure 3.98: Analyzing power for three different hadron pairs as a function of mass of the pair. Only pairs emitted in the forward direction have been included in the analysis.

3.4.8 Plotting Mass Dependence with Higher p_T Cuts

According to the model prediction from Ref. [28], the single spin asymmetry can be larger at higher p_T. Therefore, selecting high p_T pair would enhance

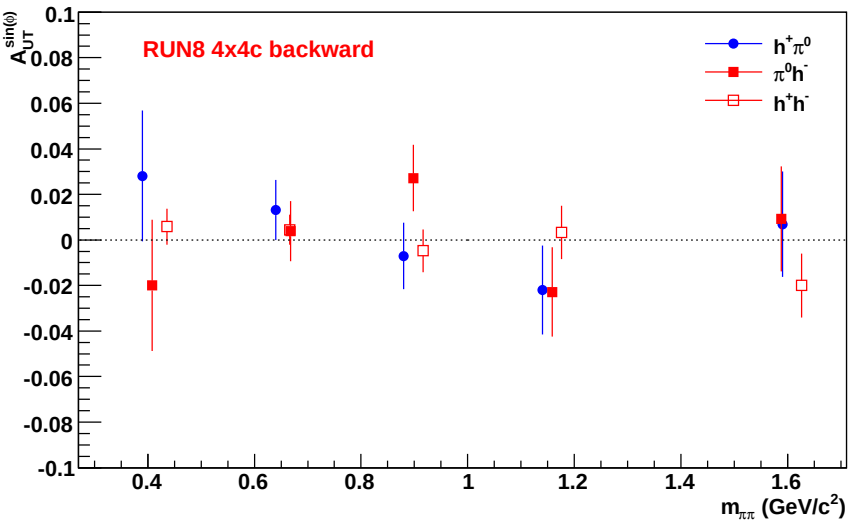

Figure 3.99: Analyzing power for three different hadron pairs as a function of mass of the pair. Only pairs emitted in the backward direction have been included in the analysis.

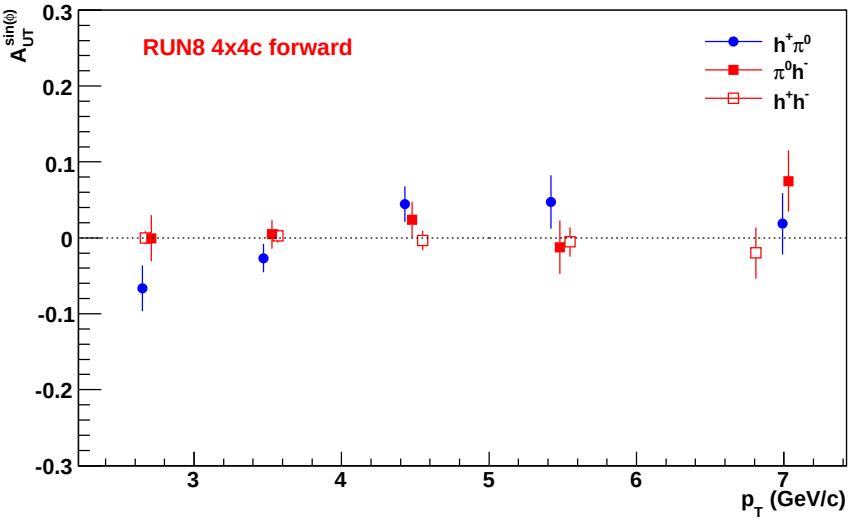

Figure 3.100: Analyzing power for three different hadron pairs as a function of the pair p_T. (pairs are in the forward direction)

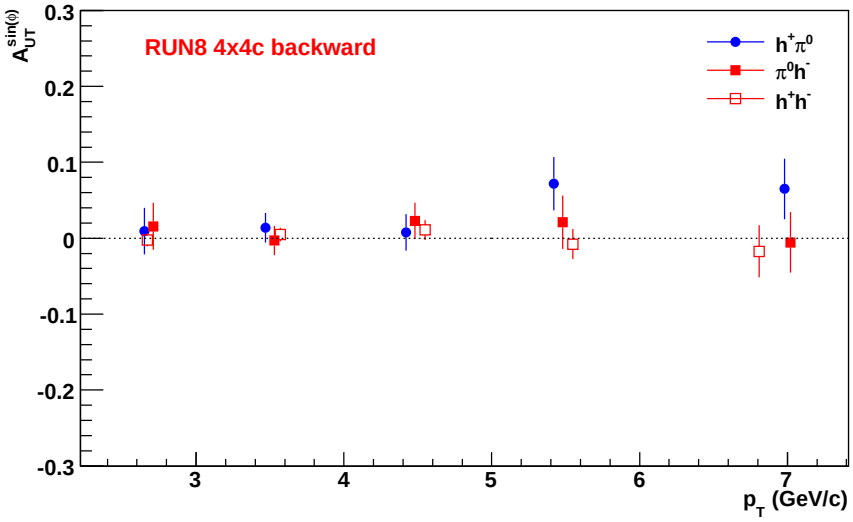

Figure 3.101: Analyzing power for three different hadron pairs as a function of the pair p_T. (pairs are in the backward direction)

the asymmetry while increasing the statistical uncertainties at the same time. The results for the 4x4c and 4x4a samples are shown in Figs. 3.102 and 3.103.

The results show large statistical uncertainties. A few data points seem to deviate from zero. However, there is not statistically significant signal for non zero asymmetries at high p_T.

3.4.9 Calculate Asymmetries with Random Ordering of Particles

When calculating the asymmetries in this analysis, the order of the two particles are always fixed: the particle with the more positive charge is taken as particle one and the other as the second particle: $h^+\pi^0$, i.e. $h^+\pi^0$, π^0h^- and h^+h^-. If the ordering within each pair and for each event is randomized

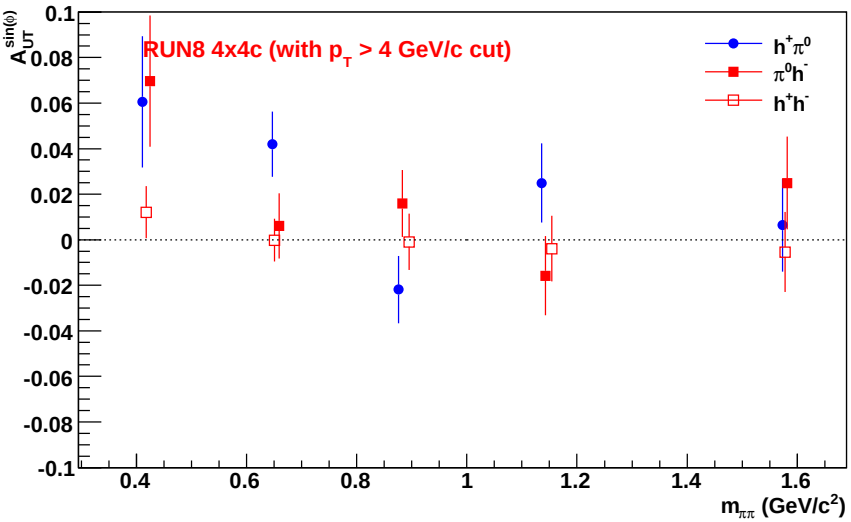

Figure 3.102: Analyzing power for three different hadron pairs as a function of the pair mass and p_T of the pairs is required to be greater than 4 GeV/c. The 4x4c sample is used.

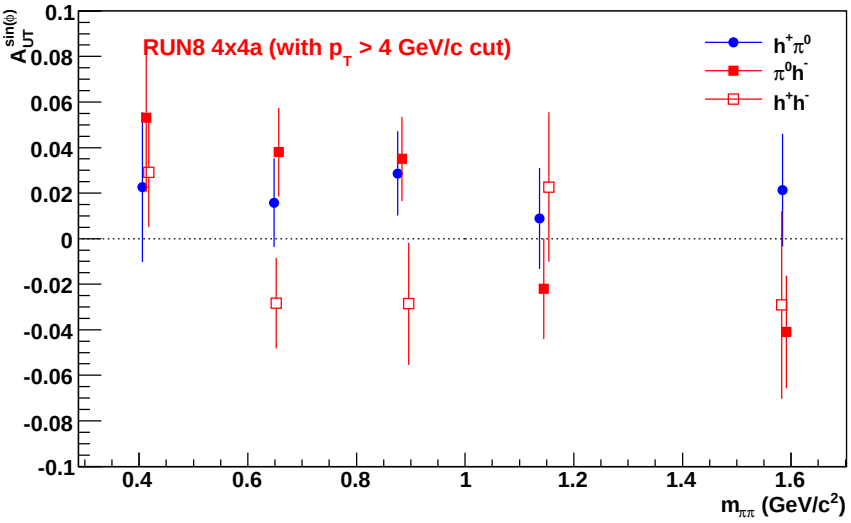

Figure 3.103: Analyzing power for three different hadron pairs as a function of the pair mass and p_T of the pairs is required to be greater than 4 GeV/c. The 4x4a sample is used.

then the physical asymmetries should average to zero. The results are shown in Figs. 3.104 and 3.104. As expected, all asymmetries are found consistent with zero.

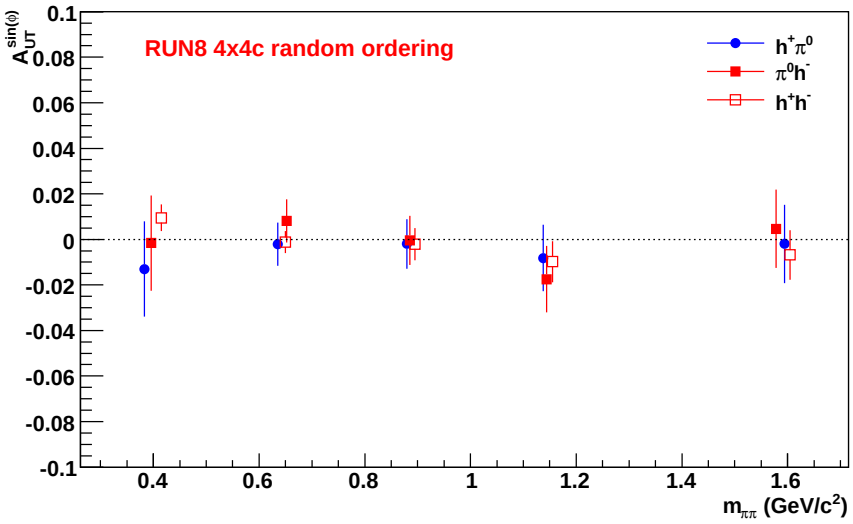

Figure 3.104: Analyzing power for three different hadron pairs as a function of the pair mass. The 4x4c sample is used.

3.4.10 Other Systematic Uncertainties

An important contribution to the systematic error stems from the uncertainty in the relative luminosity. The upper limit for this error was estimated in a previous analysis to be 2×10^{-3} and is adapted here. This will be added as an systematic error.

When calculating single spin asymmetry for one polarized beam, the polarization in the other beam is averaged and it is assumed that the second beam is unpolarized. However, at RHIC, both beams are polarized and therefore a residual polarization can exist in the unpolarized beam. As shown in

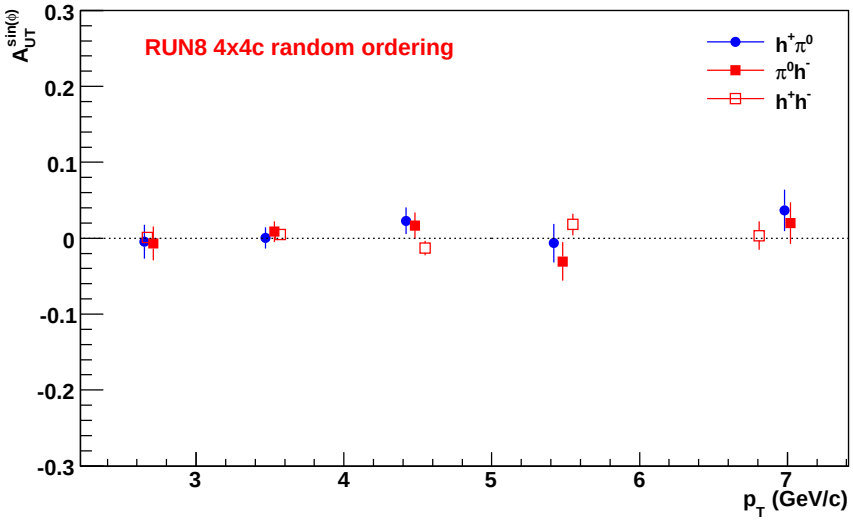

Figure 3.105: Analyzing power for 3 pairs as a function of the pair p_T. (4x4c sample is used here)

Fig. 3.106, this residual polarization is smaller than 8%. The residual polarization will introduce a double spin asymmetry in Eq. 3.8. But since this asymmetry is suppressed by the size of the residual polarization, its effect is negligible.

Finally, we briefly discuss the uncertainties for the beam polarization. The beam polarization analysis is carried out by the RHIC polarimeter group. For the analysis presented in this thesis the polarization values and uncertainties obtained by this group are used. The global uncertainties for the polarizations are are 4.2% and 7.2% for blue and yellow respectively. Uncertainties in the beam polarization can affect both the analyzing power $A_{UT}^{\sin\phi}$ and its uncertainty, $\Delta P/P$ is considered as a scaling error for the results in this analysis.

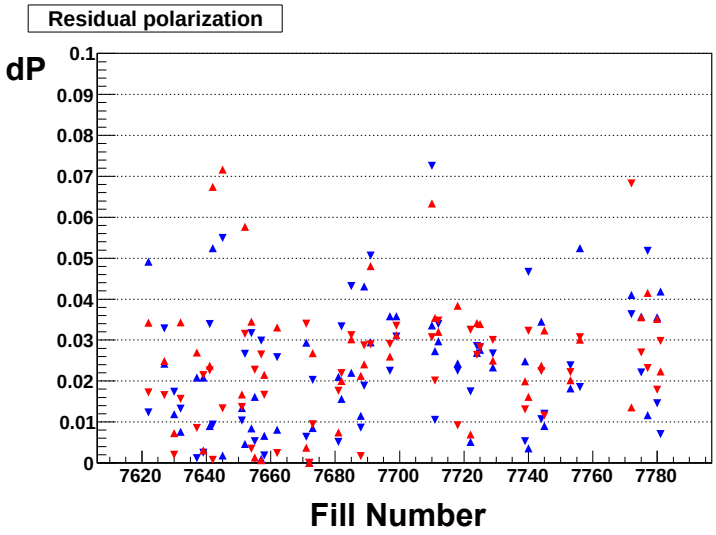

Figure 3.106: The residual polarization when one beam (blue/red markers for blue/yellow beams) has up/down (up/down triangle markers) polarization state for all fills in the transverse running.

Chapter 4

Results and Discussion

In the previous chapter the analysis for single spin asymmetries in the inclusive production of di-hadron pairs was developed using the data sample from the RHIC run in 2008. An identical analysis was carried out for the data sample collected in 2006. In this section we combine the di-hadron single spin asymmetries obtained from the run6 and run8 samples. It is found that with the combined data sets the observed asymmetries $A_{UT}^{\sin\phi}$ are consistent with zero.

4.1 Comparison and Combination of the 2006 and 2008 Data Samples

243 physics runs collected during the 2006 PHENIX transverse running are used, 236 runs are used in 2008. The integrated luminosity used in the analysis is $1.9pb^{-}1$ for run6 and $4.4pb^{-}1$ for run8 respectively.

Table 4.1 shows the count of triggers from all runs used in the run6 and run8 analysis. Although the luminosity increased by a factor of 2 in 2008, the PgGl-calorimeter, corresponding to about 25% of the acceptance was masked off in the calorimeter trigger. The increase in the number of hadron pairs for run8 therefore is only a factor 2*3/4=1.5 compared to run 6. This is evident from the numbers in Table 4.1.

trigger	N(run8)	N(run6)	R
4x4c	549823695	494099567	1.11
4x4a	274950791	95708756	2.87
4x4b	68876888	23396049	2.94

Table 4.1: Number of calorimeter energy cluster triggers for all runs used. The ratios R=N(run8)/N(run6) compares the statistics in runs 6 and 8.

	4x4c			4x4a
type of pair	N(run6)	N(run8)	R	N(run8)
$\pi^0 h^+$	1574849	2176522	1.38	311406
$\pi^0 h^-$	1497171	2299047	1.53	302166
$h^+ h^-$	582867	815591	1.40	302166
$\pi^0 h^-$ (sideband)	1605933	2448102	1.52	255169
$\pi^0 h^-$ (sideband)	1641126	2718251	1.65	264925

Table 4.2: the number of hadron pairs used in the analysis of the run6 and run8 data samples. The ratio R=N(run8)/N(run6) compares the number of pairs in runs 8 and 6.

To compare the statistical uncertainties between run6 and run8, the difference in polarization orientation also needs to be considered. Running with vertical polarization will increase statistical uncertainty by a factor of 1.4 as discussed in a previous section. In addition, the average polarization in run8 is lower than in run6 as shown in Table 4.1 which increases the statistical uncertainties. More specifically the yellow beam in run8 had significantly lower polarizations which can be seen by comparing the errors bars for the two different beam asymmetries calculated for run8.

The results from run6 and run8 are shown in Fig. 4.1 as function of pair invariant mass and 4.2 as function of p_T. The combined run6 and run8 results is also shown in Figs. 4.1 and 4.2 with improved statistical uncertainties. However, the asymmetries with the combined statistics are still compatible

beam	run6	run8
blue	51%	50%
yellow	52%	43%

Table 4.3: Comparison of the beam polarization for the yellow and blue beams in runs 6 and 8.

with zero within the statistical errors.

The analysis presented in this thesis is the first measurement of single spin asymmetries in inclusive di-hadron production in polarized proton-proton collisions. With the presently available data samples available from past RHIC runs the asymmetries are found to be consistent with zero. The errors allow to place a bound on the maximum size of the asymmetries of about $1-2\%$.

Future transverse spin data runs at RHIC are scheduled for the years 2012 and 2013. It is assumed that this will increase the available data sample to about $40 pb^{-1}$. Fig. 4.3 shows projected errors bars for $A_{UT}^{\sin\phi}$ with $\int Ldt = 40\, pb^{-1}$. Based on the current results on transversity quark distributions and recent results from the Belle collaboration on spin asymmetries in di-hadron fragmentation a simple estimate suggest that di-hadron asymmetries in PHENIX may be of the order of $A_{UT}^{\sin\phi} \sim 0.005$. As can be seen from the projected error bars in Fig. 4.3 asymmetries of this size can be detected with the additional transverse spin runs scheduled at RHIC.

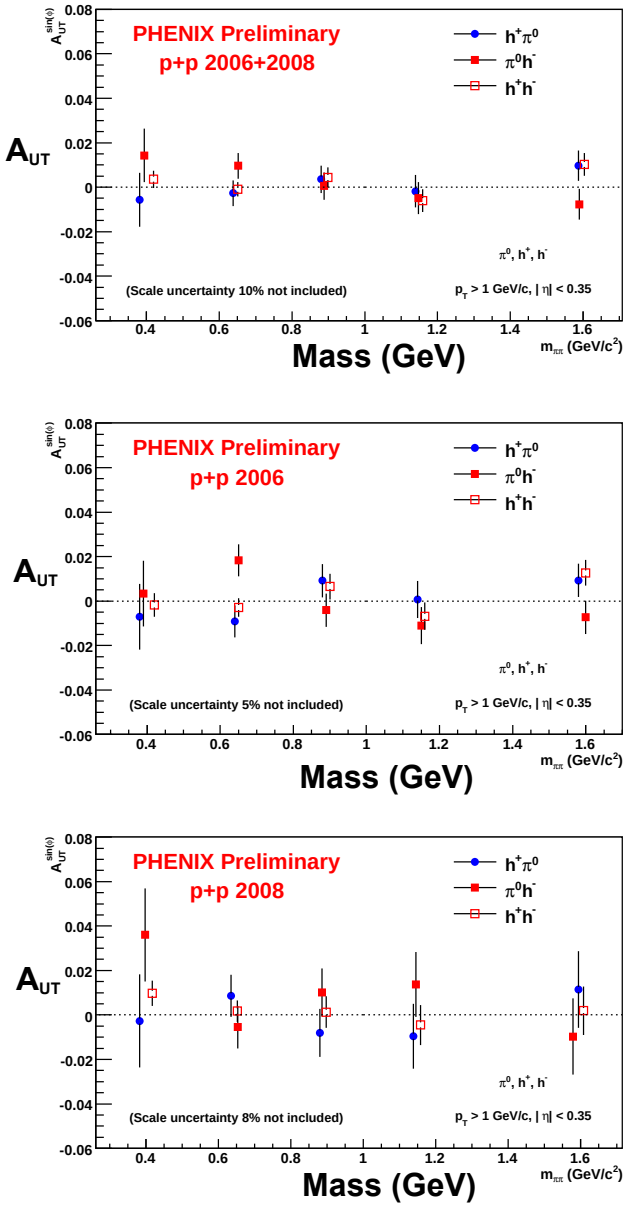

Figure 4.1: Analyzing power for three different hadron pairs as a function of invariant mass of the pair. The top plots shows the combined result for the data samples from run6 and run8. The second and third plot from top are the results from runs 6 and 8 separately.

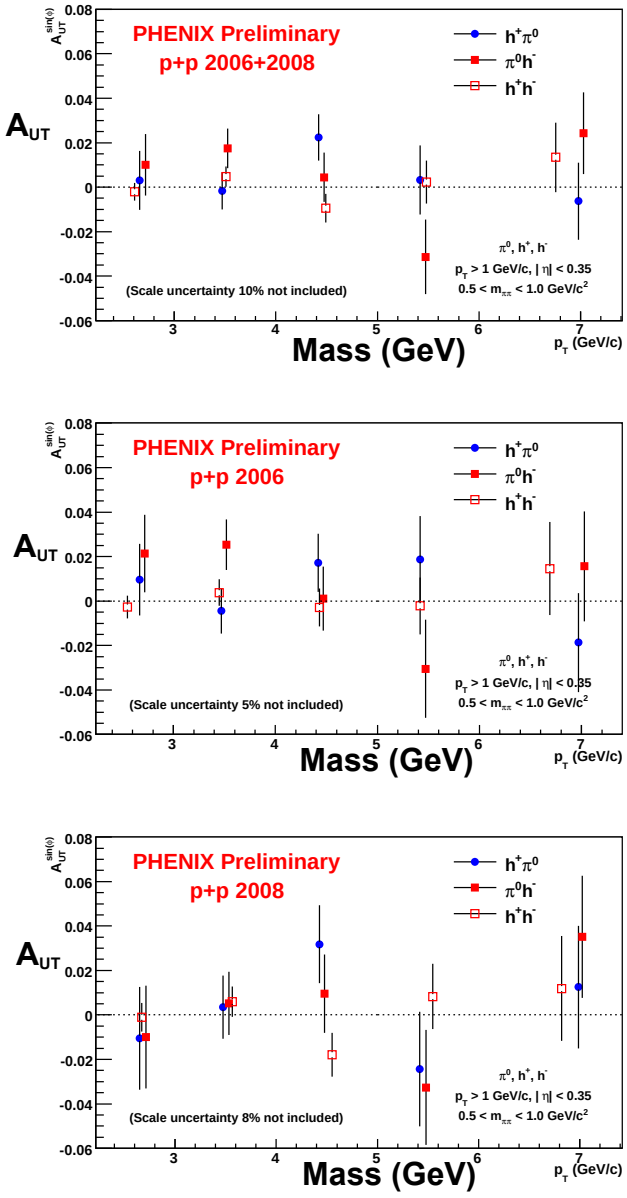

Figure 4.2: Analyzing power for three different hadron pairs as a function of p_T of the pair. First one is combined results from run6 and run8. The second and he third plots are run6 and run8 results separately.

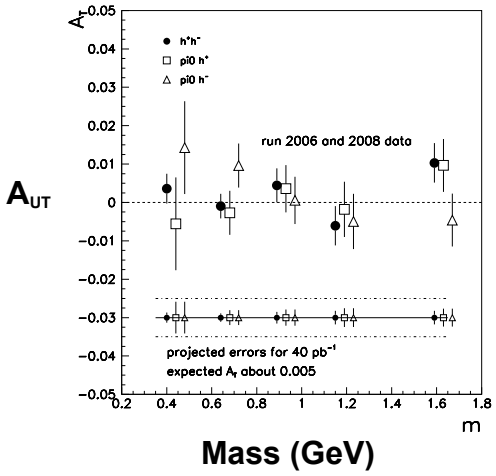

Figure 4.3: Final results from run6 and run8 data, and projected statistical uncertainties on $A_{UT}^{\sin\phi}$ for different hadron pairs with $40pb^{-1}$ integrated luminosity of transverse polarized p+p running.

Chapter 5

Flavor Asymmetry via W Boson Production

The earliest parton models assumed that the proton sea was flavor symmetric, even though proton's valence quark distributions were known to be flavor asymmetric. Inherent in this assumption is that the content of the sea is independent of the valence quark's composition. The assumption of sea-quark flavor symmetry was not based on any known physics, and it remained to be tested by experiments. Neutrino-induced charm production experiments [61] provided clear evidences that the strange-quark content of the nucleon is only about half of the up or down sea quarks. This flavor asymmetry is attributed to the much heavier mass for strange quark compared to the up and down quarks. The similarity between the masses of up and down quarks suggests that the nucleon sea should be nearly up-down symmetric. However, it was pointed out that the existence of a pion cloud in the proton could lead to an asymmetric up-down sea [62].

A measurement of the Gottfried integral in deep-inelastic scattering (DIS) provides a direct check of the $\bar{d}/\bar{u}$ flavor-symmetry assumption. The Gottfried integral [63] is defined as

$$I_G = \int_0^1 \left[F_2^p(x) - F_2^n(x)\right]/x \; dx = \frac{1}{3} + \frac{2}{3}\int_0^1 \left[\bar{u}_p(x) - \bar{d}_p(x)\right] dx, \qquad (5.1)$$

where F_2^p and F_2^n are the proton and neutron structure functions measured in DIS experiments and x is the fraction of the nucleon's momentum carried by the quark. The second step in Eq. 5.1 follows from the assumption of charge symmetry (CS) at the partonic level, namely, $u_p(x) = d_n(x)$, $d_p(x) = u_n(x)$, $\bar{u}_p(x) = \bar{d}_n(x)$, and $\bar{u}_p(x) = \bar{d}_n(x)$. Under the assumption of a symmetric sea, $\bar{u}_p = \bar{d}_p$, the Gottfried Sum Rule (GSR), $I_G = 1/3$, is obtained. The most accurate test of the GSR was reported by the New Muon Collaboration (NMC) [64], which measured F_2^p and F_2^n over the region $0.004 \leq x \leq 0.8$. They determined the Gottfried integral to be 0.235 ± 0.026, significantly below 1/3. This surprising result has generated much interest. Although the violation of the GSR can be explained by assuming unusual behavior of the parton distributions at very small x, a more natural explanation is that the assumption $\bar{u} = \bar{d}$ is invalid.

The proton-induced Drell-Yan (DY) process provides an independent means to probe the flavor asymmetry of the nucleon sea [65]. An important advantage of the DY process is that the x dependence of $\bar{d}/\bar{u}$ asymmetry can be determined. Using a 450 GeV proton beam, the NA51 Collaboration [66] at CERN measured dimuons produced in $p + p$ and $p + d$ reaction and obtained $\bar{u}/\bar{d} = 0.51 \pm 0.04(stat) \pm 0.05(syst)$ at $x = 0.18$ and $\langle M_{\mu\mu} \rangle = 5.22$ GeV. At Fermilab, a DY experiment (E866/NuSea) covering a broad kinematic range with high statistics has been carried out [67, 68, 69]. The E866 Collaboration measured the DY cross section ratios for $p+d$ to that of $p+p$ at the forward-rapidity region using intense 800 GeV proton beams. At forward rapidity region and assuming the validity of charge symmetry, one obtains

$$\sigma_{DY}(p + d)/2\sigma_{DY}(p + p) \simeq (1 + \bar{d}(x)/\bar{u}(x))/2. \tag{5.2}$$

This ratio was found to be significantly different from unity for $0.015 < x < 0.35$, indicating an excess of $\bar{d}$ with respect to $\bar{u}$ over an appreciable range in x.

The HERMES Collaboration has also reported a semi-inclusive DIS measurement of charged pions from hydrogen and deuterium targets [70]. Based

on the differences between charged-pion yields from the two targets, $\bar{d} - \bar{u}$ is determined in the kinematic range $0.02 < x < 0.3$ and 1 GeV^2/c^2 $< Q^2 <$ 10 GeV^2/c^2. The HERMES results are consistent with the E866 results obtained at significantly higher Q^2.

Many theoretical models, including meson-cloud model, chiral-quark model, Pauli-blocking model, instanton model, chiral-quark soliton model, and statistical model, have been proposed to explain the $\bar{d}/\bar{u}$ asymmetry, as reviewed in [71, 72]. While these models can describe the general trend of the $\bar{d}/\bar{u}$ asymmetry, they all have difficulties explaining the $\bar{d}/\bar{u}$ data at large x ($x > 0.2$) [73]. Since the perturbative process gives a symmetric $\bar{d}/\bar{u}$ while a non-perturbative process is needed to generate an asymmetric $\bar{d}/\bar{u}$ sea, the relative importance of these two components is directly reflected in the $\bar{d}/\bar{u}$ ratios. Thus, it would be very important to have new measurements sensitive to the $\bar{d}/\bar{u}$ ratios at $x > 0.2$. The upcoming Fermilab E906 Drell-Yan experiment [74] plans to extend the measurement to larger x region.

With the advent of $p + p$ colliders at RHIC and LHC, an independent technique to study the $\bar{d}/\bar{u}$ asymmetry now becomes available. By measuring the ratio of W^+ versus W^- production in unpolarized $p+p$ collision, the $\bar{d}/\bar{u}$ asymmetry can be determined [75, 76, 77] with some distinct advantages over the existing methods. First, this method does not require the assumption of the validity of charge symmetry. All existing experimental evidences for $\bar{d}/\bar{u}$ asymmetry depend on the comparison between DIS or DY scattering cross sections off hydrogen versus deuterium targets. The possibility that charge symmetry could be violated at the parton level has been discussed by several authors [78, 79, 80, 81, 82, 83]. Ma and collaborators [78, 79] pointed out that the violation of the Gottfried Sum Rule can be caused by charge symmetry violation as well as by flavor asymmetry of the nucleon sea. They also showed that DY experiments, such as NA51 and E866, are subject to both flavor asymmetry and charge symmetry violation effects. In fact, an even larger amount of flavor asymmetry is required to compensate for the possible charge symmetry violation effect [84]. A comparison between W

production in $p+p$ collision with the NA51 and E866 Drell-Yan experiments would disentangle the flavor asymmetry from the charge symmetry violation effects.

Another advantage of W production in $p+p$ collision is that it is free from any nuclear effects. As pointed out by several authors [85, 86, 87, 88], the nuclear modification of parton distributions should be taken into account for DIS and DY process involving deuterium targets. The nuclear shadowing effect for deuteron at small x could lead to a 4% to 10% decrease in the evaluation of the Gottfried integral by the NMC [85, 88]. Moreover, the nucleon Fermi motion at large x also affects the extraction of neutron structure function and would cause additional uncertainty in the evaluation of the Gottfried integral [86]. The nuclear effects and the associated uncertainty are absent in W production in $p+p$ production.

Finally, the W production is sensitive to $\bar{d}/\bar{u}$ flavor asymmetry at a Q^2 scale of ~ 6500 GeV^2/c^2, significantly larger than all existing measurements. This offers the opportunity to examine the QCD evolution of the sea-quark flavor asymmetry. The large mass of W also implied that the RHIC data are sensitive to the sea-quark flavor asymmetry at the large x region, which remains poorly known both experimentally and theoretically as discussed earlier.

The differential cross section for W^+ production in hadron-hadron collision can be written as [89]

$$\begin{aligned}\frac{d\sigma}{dx_F}(W^+) &= K\frac{\sqrt{2}\pi}{3}G_F\left(\frac{x_1x_2}{x_1+x_2}\right)\left\{\cos^2\theta_c\left[u(x_1)\bar{d}(x_2)+\bar{d}(x_1)u(x_2)\right]+\right.\\ &\left.\sin^2\theta_c\left[u(x_1)\bar{s}(x_2)+\bar{s}(x_1)u(x_2)\right]\right\}, \qquad (5.3)\end{aligned}$$

where $u(x), d(x)$, and $s(x)$ signify the up, down, and strange quark distribution functions in the hadrons. x_1, x_2 are the fractional momenta carried by the partons in the colliding hadron pair and $x_F = x_1 - x_2$. G_F is Fermi coupling constant and θ_c is the Cabbibo angle. The factor K takes into account the contributions from first-order QCD corrections [89]

$$K \simeq 1 + \frac{8\pi}{9}\alpha_s(Q^2). \tag{5.4}$$

At the W mass scale, $\alpha_s \simeq 0.1158$ and $K \simeq 1.323$. This indicates that higher-order QCD processes are relatively unimportant for W production. An analogous expression for W^- production cross section is given as

$$\begin{aligned}\frac{d\sigma}{dx_F}(W^-) &= K\frac{\sqrt{2}\pi}{3}G_F\left(\frac{x_1x_2}{x_1+x_2}\right)\left\{\cos^2\theta_c\left[\bar{u}(x_1)d(x_2)+d(x_1)\bar{u}(x_2)\right]+\right.\\ &\left.\sin^2\theta_c\left[\bar{u}(x_1)s(x_2)+s(x_1)\bar{u}(x_2)\right]\right\},\end{aligned} \tag{5.5}$$

An interesting quantity to be considered is the ratio of the differential cross sections for W^+ and W^- production. If one ignores the much smaller contribution from the strange quarks, this ratio can be written as

$$R(x_F) \equiv \frac{\frac{d\sigma}{dx_F}(W^+)}{\frac{d\sigma}{dx_F}(W^-)} = \frac{u(x_1)\bar{d}(x_2)+\bar{d}(x_1)u(x_2)}{\bar{u}(x_1)d(x_2)+d(x_1)\bar{u}(x_2)}. \tag{5.6}$$

For $p+p$ collision, it is evident that $R(x_F)$ is symmetric with respect to $x_F = 0$, namely, $R(x_F) = R(-x_F)$. It is clear that $R(x_F)$ in $p+p$ collision is sensitive to the sea-quark distributions in the proton. At large x_F, we have

$$R(x_F \gg 0) = \frac{u(x_1)\bar{d}(x_2)+\bar{d}(x_1)u(x_2)}{\bar{u}(x_1)d(x_2)+d(x_1)\bar{u}(x_2)} \approx \frac{u(x_1)}{d(x_1)}\frac{\bar{d}(x_2)}{\bar{u}(x_2)}. \tag{5.7}$$

At $x_F = 0$, where $x_1 = x_2 = x$, one obtains

$$R(x_F = 0) = \frac{u(x)\bar{d}(x)+\bar{d}(x)u(x)}{\bar{u}(x)d(x)+d(x)\bar{u}(x)} = \frac{u(x)}{d(x)}\frac{\bar{d}(x)}{\bar{u}(x)}. \tag{5.8}$$

As the $u(x)/d(x)$ ratios are already well known, a measurement of $R(x_F)$ in $p+p$ collision gives an accurate determination of the ratio $\bar{d}(x)/\bar{u}(x)$.

Figure 1 shows the predictions of $R(x_F)$ for $p+p$ collision at $\sqrt{s} =$ 500 GeV. Four different structure function sets together with the full expressions for W^+, W^- production cross sections given by Eqs. (3) and (5) have

been used in the calculations. The first PDF used here is MRS S0' [90]. It assumes symmetric $\bar{u}$ and $\bar{d}$ distributions, therefore, according to Eq. (8), $R(x_F) \simeq 2$ at $x_F = 0$ as shown in Fig. 1. The other three PDFs used here allowed certain flavor asymmetry in nucleon sea. New experimental data from Drell-Yan measurement by E866 Collaboration is included in the global fit performed by CTEQ6 [91], GJR08 [92] and MSTW2008 [93] to determine x-dependence of $\bar{u}$, $\bar{d}$ asymmetry in the nucleon sea. Thus $R(x_F)$ for those three PDF are similar at $x_F = 0$ and are significantly higher than 2 obtained in the MRS S0' case. Table 5.1 shows the x_1 and x_2 values for W production at RHIC with center of mass energy 500 GeV.

x_F	0.0	0.1	0.2	0.3	0.4	0.5	0.6	0.7	0.8
x_1	0.16	0.22	0.29	0.37	0.46	0.55	0.64	0.73	0.83
x_2	0.16	0.12	0.09	0.07	0.06	0.05	0.04	0.03	0.03

Table 5.1: values for x_1 and x_2 at different x_F for W production at $\sqrt{s} =$ 500 GeV.

Although Fig. 1 shows that the differences between the predictions of $R(x_F)$ for various PDFs are quite conspicuous, in practice it is not the x_F distributions of the W which are measured but rather the charged leptons from the decay of the W-bosons. The measured lepton ratio is defined as:

$$R(y_l) \;=\; \frac{d\sigma/dy_l(W^+ \to l^+)}{d\sigma/dy_l(W^- \to l^-)}, \tag{5.9}$$

where the lepton rapidity $y_l = 1/2 \ln\left[(E_l + p_l)/(E_l - p_l)\right]$ is defined in terms of the decay lepton's energy E_l and longitudinal momentum p_l in the laboratory frame. The differential cross section $d\sigma/dy_l$ is obtained by convoluting the $q\overline{q} \to W$ cross section for each x_F with the relevant $W \to l\ \nu$ decay distribution, $d\sigma/d\cos\theta \propto (1 \pm \cos\theta)^2$, where θ is the angle between the lepton $l^{\pm}$ direction and the $W^{\pm}$ polarization in the W rest frame.

In Fig. 2 we show the predicted lepton ratios $R(y_l)$ calculated for various PDFs. The statistical uncertainties for the lepton ratios are estimated for

recorded luminosity of 300 pb^{-1} at RHIC [94]. The acceptance is for PHENIX experiment [95], which covers $|y| < 0.35$ in central rapidities and $-2.2 < y < -1.1$, $1.1 < y < 2.4$ in forward rapidities. Fig. 2 has clearly demonstrated that a measurement of $R(y_l)$ at RHIC is able to distinguish flavor symmetric and flavor asymmetric nucleon sea.

The calculation for $R(x_F)$ and $R(y_l)$ has also been carried out for CMS experiment at LHC [96]. Fig. 3 shows results for $R(x_F)$ at LHC. At $x_F = 0$, all PDFs used here obtain similar results for $R(x_F)$. This is due to the fact that at much higher c.m.s. energy, this measurement probes sea quark flavor asymmetry at even lower x compared to previous measurements from Drell-Yan process and semi-inclusive DIS, and all four PDFs used here have predicted that flavor asymmetry will diminish as $x \to 0$. Table 5.2 shows the x_1 and x_2 values for W production at LHC with center of mass energy 14 TeV.

x_F	0.0	0.1	0.2	0.3	0.4	0.5	0.6
x_1	0.01	0.10	0.20	0.30	0.40	0.50	0.60
x_2	0.0114	0.0013	0.0007	0.0004	0.0003	0.0003	0.0002

Table 5.2: values for x_1 and x_2 at different x_F for W production at $\sqrt{s} = 7$ TeV.

Fig. 4 shows results of the lepton ratio $R(y_l)$ where integrated luminosity is assumed to be 10 fb $^{-1}$ corresponding to one year low luminosity running of $p + p$ collisions at $\sqrt{s} = 14$ TeV and the pseudorapidity coverage is taken as $|\eta| < 5$ [96]. The sensitivity of $R(y_l)$ in Fig. 4 is more than sufficient to differentiate flavor symmetry and asymmetry used in different parameterizations.

In conclusion, W production at RHIC and LHC would offer an independent means to examine the $\bar{d}/\bar{u}$ flavor asymmetry in the proton. Measurements of the cross section ratios of $W^+ \to l^+$ and $W^- \to l^-$ production in $p + p$ collisions would provide a sensitive test of current PDFs. The W

production experiments at RHIC and LHC will offer the unique opportunity of extracting the $\bar{d}/\bar{u}$ flavor asymmetry at large x and very high Q^2 without the complications associated with the charge symmetry breaking effect and nuclear binding effect. The proposed measurements are within the capabilities of the existing detectors at RHIC and LHC and can be carried out in the near future.

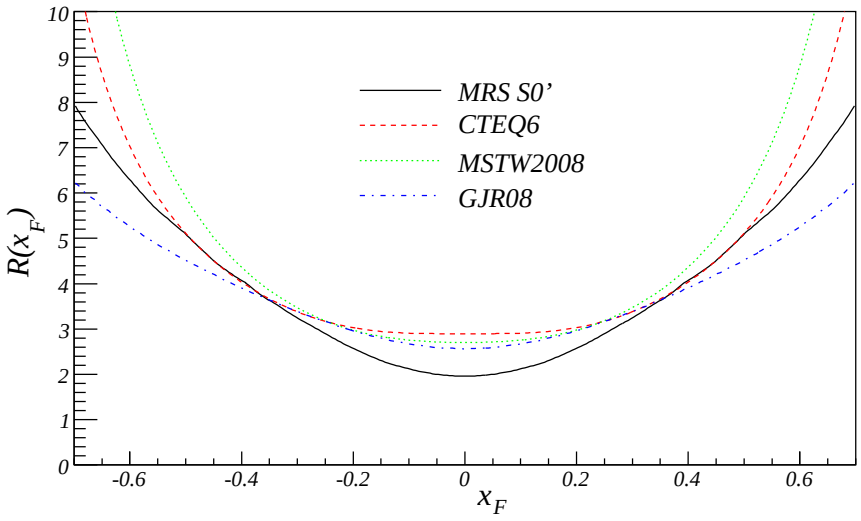

Figure 5.1: Prediction of the ratio $R(x_F)$ as a function of x_F for p+p collision at $\sqrt{s}$ of 500 GeV using various parton distribution functions.

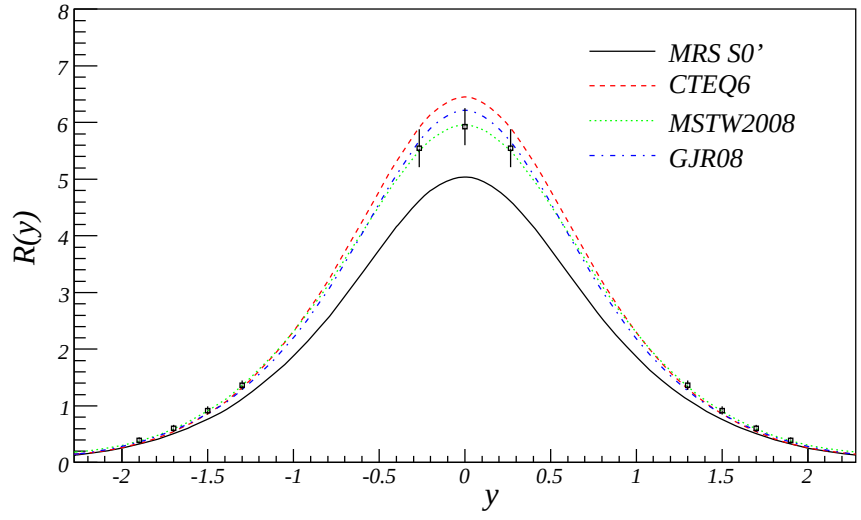

Figure 5.2: Prediction of the ratio $R(y_l)$ as a function of y for p+p collision at $\sqrt{s}$ of 500 GeV using various parton distribution functions. The projected sensitivities for a run with recorded luminosity of 300 pb^{-1} for the PHENIX detector are also shown.

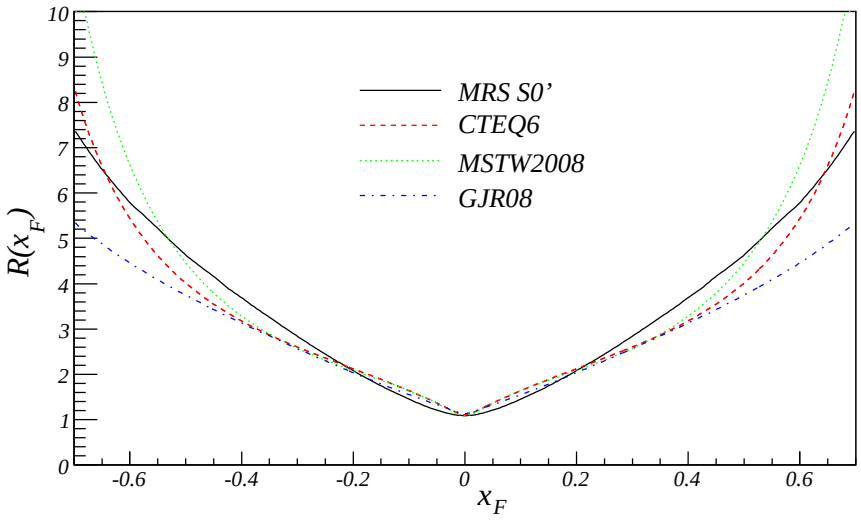

Figure 5.3: Prediction of the ratio $R(x_F)$ as a function of x_F for p+p collision at $\sqrt{s}$ of 14 TeV using various parton distribution functions.

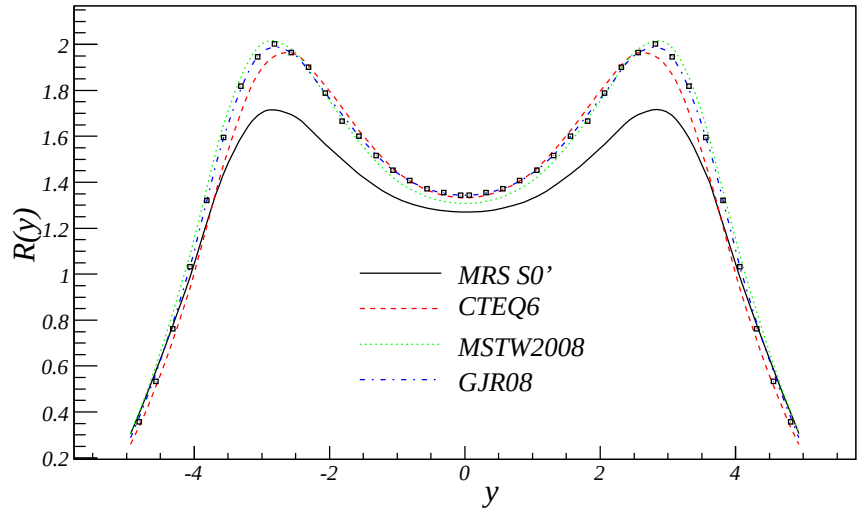

Figure 5.4: Prediction of the ratio $R(y_l)$ as a function of y for p+p collision at $\sqrt{s}$ of 14 TeV using various parton distribution functions. The projected sensitivities for a run with integrated luminosity of 10 fb^{-1} for the CMS detector are also shown.

Bibliography

[1] B. Povh, K. Rith, C. Scholz, and F. Zetsche. *Particles and Nuclei*. Springer-Verlag Berlin Heidelberg, 1999.

[2] G. Miller et al. Inelastic electron-proton scattering at large momentum transfers. *Phys. Rev.*, D5:528, 1972.

[3] M. Peskin and D. Schroeder. *An introduction to quantum field theory*. WestView Press, 1995.

[4] J. Owens and W. K. Tung. Parton distribution functions of hadrons. *Annu. Rev. Nucl. Part. Sci.*, 41:291, 1992.

[5] H. L. Lai et al. Global qcd analysis and the cteq parton distributions. *Phys. Rev. D*, 51(9):4763–4782, May 1995.

[6] J. Pumplin, A. Belyaev, J. Huston, D. Stump, and W. K. Tung. Parton distributions and the strong coupling strength alpha(s). *JHEP*, 02:032, 2006.

[7] V. Barone, A. Drago, and P.G. Ratcliffe. Transverse polarisation of quarks in hadrons. *Physics Reports*, 359:1–168, 2002.

[8] W. Melnitchouk, R. Ent, and C. Keppel. Quark-hadron duality in electron scattering. *Phys. Rept.*, 406:127–301, 2005.

[9] M. Hirai, S. Kumano, and N. Saito. Determination of polarized parton distribution functions and their uncertainties. *Phys. Rev. D*, 69(5):054021, Mar 2004.

[10] Daniel de Florian, Rodolfo Sassot, Marco Stratmann, and Werner Vogelsang. Global Analysis of Helicity Parton Densities and Their Uncertainties. *Phys. Rev. Lett.*, 101:072001, 2008.

[11] J. Collins, S. Heppelmann, and G. Ladinsky. Measuring transversity densities in singly polarized hadonr-hadron and lepton-hadron collisions. *Nucl. Phys.*, B420:562, 1994.

[12] J. Ralston and D. E. Soper. Production of dimuons from high-energy polarized proton-proton collisions. *Nucl. Phys.*, B152:109, 1979.

[13] Xavier Artru and Mustapha Mekhfi. Transversely Polarized Parton Densities, their Evolution and their Measurement. *Z. Phys.*, C45:669, 1990.

[14] Jacques Soffer. Positivity constraints for spin-dependent parton distributions. *Phys. Rev. Lett.*, 74(8):1292–1294, Feb 1995.

[15] R. G. Edwards et al. Nucleon structure in the chiral regime with domain wall fermions on an improved staggered sea. *PoS*, LAT2006:121, 2006.

[16] B. L. G. Bakker, E. Leader, and T. L. Trueman. A critique of the angular momentum sum rules and a new angular momentum sum rule. *Phys. Rev.*, D70:114001, 2004.

[17] R. L. Jaffe. Can transversity be measured? 1997.

[18] F. Halzen and A. Martin. *Quarks and leptons.* John Wiley and Sons, 1984.

[19] Gerry Bunce, Naohito Saito, Jacques Soffer, and Werner Vogelsang. Prospects for spin physics at RHIC. *Ann. Rev. Nucl. Part. Sci.*, 50:525–575, 2000.

[20] O. Martin, A. Schäfer, M. Stratmann, and W. Vogelsang. Transverse double-spin asymmetries for muon pair production in pp collisions. *Phys. Rev. D*, 60(11):117502, Nov 1999.

[21] A. V. Efremov, K. Goeke, and P. Schweitzer. Transversity distribution function in hard scattering of polarized protons and antiprotons in the PAX experiment. *Eur. Phys. J.*, C35:207–210, 2004.

[22] R. Seidl et al. Measurement of azimuthal asymmetries in inclusive production of hadron pairs in e[sup +]e[sup -] annihilation at belle. *Phys. Rev. Lett.*, 96(23):232002, 2006.

[23] D. Adams et al. *Phys. Lett.*, B 264:462, 1991.

[24] Dennis Sivers. Single-spin production asymmetries from the hard scattering of pointlike constituents. *Phys. Rev. D*, 41(1):83–90, Jan 1990.

[25] A. Airapetian et al. Single-spin asymmetries in semi-inclusive deep-inelastic scattering on a transversely polarized hydrogen target. *Phys. Rev. Lett.*, 94:012002, 2005.

[26] E. S. Ageev et al. A new measurement of the Collins and Sivers asymmetries on a transversely polarised deuteron target. *Nucl. Phys.*, B765:31–70, 2007.

[27] M. Anselmino et al. Transversity and collins functions from sidis and e[sup +]e[sup -] data. *Phys. Rev.*, D75(5):054032, 2007.

[28] R. L. Jaffe, Xuemin Jin, and Jian Tang. Interference fragmentation functions and the nucleon's transversity. *Phys. Rev. Lett.*, 80(6):1166–1169, Feb 1998.

[29] Marco Radici, Rainer Jakob, and Andrea Bianconi. Accessing transversity with interference fragmentation functions. *Phys. Rev.*, D65:074031, 2002.

[30] Jian Tang. Probing the nucleon's transversity via two-meson production in polarized nucleon nucleon collisions. 1998.

[31] Alessandro Bacchetta and Marco Radici. Dihadron interference fragmentation functions in proton proton collisions. *Phys. Rev.*, D70:094032, 2004.

[32] A. Bacchetta, C. J. Bomhof, P. J. Mulders, and F. Pijlman. Single spin asymmetries in hadron hadron collisions. *Phys. Rev.*, D72:034030, 2005.

[33] P. B. van der Nat. *Transversity in two-hadron fragmentation.* PhD thesis, Vrije Universiteit Amsterdam, 2007.

[34] Christian Schill. Transversity Signals in Two-Hadron Production at COMPASS. 2007.

[35] P. Estabrooks and A. D. Martin. $\pi\pi$ phase-shift analysis below the $k\bar{K}$ threshold. *Nucl. Phys.*, B 79:301, 1974.

[36] John C. Collins and Glenn A. Ladinsky. On pi - pi correlations in polarized quark fragmentation using the linear sigma model. 1994.

[37] Xavier Artru and John C. Collins. Measuring transverse spin correlations by 4 particle correlations in e+ e- $\rightarrow$ 2 jets. *Z. Phys.*, C69:277–286, 1996.

[38] Daniel Boer, Rainer Jakob, and Marco Radici. Interference fragmentation functions in electron positron annihilation. *Phys. Rev.*, D67:094003, 2003.

[39] M. Grosse Perdekamp et al. Future transversity measurements at rhic. *Nucl. Phys.*, 711:69, 2002.

[40] I. Alekseev, C. Allgower, M. Bai, Y. Batygin, L. Bozano, K. Brown, G. Bunce, P. Cameron, E. Courant, S. Erin, J. Escallier, W. Fischer, R. Gupta, K. Hatanaka, H. Huang, K. Imai, M. Ishihara, A. Jain, A. Lehrach, V. Kanavets, T. Katayama, T. Kawaguchi, E. Kelly, K. Kurita, S. Y. Lee, A. Luccio, W. W. MacKay, G. Mahler, Y. Makdisi, F. Mariam, W. McGahern, G. Morgan, J. Muratore, M. Oka-

mura, S. Peggs, F. Pilat, V. Ptitsin, L. Ratner, T. Roser, N. Saito, H. Satoh, Y. Shatunov, H. Spinka, M. Syphers, S. Tepikian, T. Tominaka, N. Tsoupas, D. Underwood, A. Vasiliev, P. Wanderer, E. Willen, H. Wu, A. Yokosawa, and A. N. Zelenski. Polarized proton collider at rhic. *Nuclear Instruments and Methods in Physics Research Section A: Accelerators, Spectrometers, Detectors and Associated Equipment*, 499(2-3):392 – 414, 2003. The Relativistic Heavy Ion Collider Project: RHIC and its Detectors.

[41] K. Adcox et al. Phenix detector overview. *Nucl. Instrum. Methods Phys. Res.*, A 499:469, 2003.

[42] M. Allen et al. PHENIX inner detectors. *Nucl. Instrum. Meth.*, A499:549–559, 2003.

[43] L. Aphecetche et al. PHENIX calorimeter. *Nucl. Instrum. Meth.*, A499:521–536, 2003.

[44] K. Adcox et al. PHENIX central arm tracking detectors. *Nucl. Instrum. Meth.*, A499:489–507, 2003.

[45] Shigeki Misawa and Tony Chan. A guided tour of the racf. `https://www.racf.bnl.gov/about`.

[46] Robert Petkus. Bnl site report. In *HEPiX*, 2008.

[47] DESY and FNAL. dcache. `http://www.dcache.org/`.

[48] Takashi Ichihara. Current components of the cc-j. `http://ccjsun.riken.go.jp/ccj/Wako-Sys/`.

[49] Advanced Center for Computing and RIKEN Communication. Riken super combined cluster system. `http://w3cic.riken.go.jp/rscc/index_e.html`, 2009.

[50] Advanced Center for Computing and RIKEN Communication. Riken integrated cluster of clusters. http://w3cic.riken.go.jp/ricc/index_e.html, 2009.

[51] Hannelore Hmmerle and Nicole Crmel. Phenix experiment uses grid to transfer 270 tb of data to japan. http://cerncourier.com/cws/article/cern/29401.

[52] Gilles Farrache. bbftp. http://doc.in2p3.fr/bbftp/, 2005.

[53] Globus. Globus toolkit 4.0. http://www.globus.org/toolkit/docs/4.0/data/gridftp/.

[54] Kenichi Nakano. Emcal energy calibration for run8. https://www.phenix.bnl.gov/WWW/p/draft/kenichi/emcal/energy_calib_run8, 2008.

[55] J. Jia. *High-p_T Charged Hadron Suppression in Au-Au Collisions at $\sqrt{NN}$=200 GeV*. PhD thesis, State University of New York at Stony Brook, Stony Brook, NY, 2003.

[56] K. Adcox et al. PHENIX central arm tracking detectors. *Nucl. Instrum. Meth.*, A499:489–507, 2003.

[57] Stephen C. Johnson, John W. No, Federica Ceretto, Axel Drees, Thomas K. Hemmick, and Barbara Jacak. Three-dimensional track finding in the phenix drift chamber by a combinatorial hough transform method. Proceedings for Computing in High Energy and Nuclear Physics, 1998.

[58] A. Morreale. Run6 pp 200gev/c cnt beam shift and momentum scale corrections (an622). In *PHENIX Analysis Notes*, 2007.

[59] Mike Leitch. Run8 milestones. https://www.phenix.bnl.gov/WWW/run/08/run8_history.pdf, 2008.

[60] Eitaro Hamada. Run7 tof east calibration. `https://www.phenix.bnl.gov/WWW/publish/hamada/tof_calibration/homepage/run7_AuAu200GeV.html`, 2008.

[61] Janet M. Conrad, Michael H. Shaevitz, and Tim Bolton. Precision measurements with high-energy neutrino beams. *Rev. Mod. Phys.*, 70:1341–1392, 1998.

[62] Anthony William Thomas. A Limit on the Pionic Component of the Nucleon Through SU(3) Flavor Breaking in the Sea. *Phys. Lett.*, B126:97, 1983.

[63] Kurt Gottfried. Sum rule for high-energy electron - proton scattering. *Phys. Rev. Lett.*, 18:1174, 1967.

[64] P. Amaudruz et al. The Gottfried sum from the ratio F2(n) / F2(p). *Phys. Rev. Lett.*, 66:2712–2715, 1991.

[65] S. D. Ellis and W. James Stirling. Constraints on isospin breaking in the light quark sea from the Drell-Yan process. *Phys. Lett.*, B256:258–264, 1991.

[66] A. Baldit et al. Study of the isospin symmetry breaking the in the light quark sea of the nucleon from the Drell-Yan process. *Phys. Lett.*, B332:244–250, 1994.

[67] E. A. Hawker et al. Measurement of the light antiquark flavor asymmetry in the nucleon sea. *Phys. Rev. Lett.*, 80:3715–3718, 1998.

[68] J. C. Peng et al. anti-d/anti-u asymmetry and the origin of the nucleon sea. *Phys. Rev.*, D58:092004, 1998.

[69] R. S. Towell et al. Improved measurement of the anti-d/anti-u asymmetry in the nucleon sea. *Phys. Rev.*, D64:052002, 2001.

[70] K. Ackerstaff et al. The flavor asymmetry of the light quark sea from semi- inclusive deep inelastic scattering. *Phys. Rev. Lett.*, 81:5519–5523, 1998.

[71] S. Kumano. Flavor asymmetry of anti-quark distributions in the nucleon. *Phys. Rept.*, 303:183–257, 1998.

[72] Gerald T. Garvey and Jen-Chieh Peng. Flavor asymmetry of light quarks in the nucleon sea. *Prog. Part. Nucl. Phys.*, 47:203–243, 2001.

[73] W. Melnitchouk, J. Speth, and Anthony William Thomas. Dynamics of light antiquarks in the proton. *Phys. Rev.*, D59:014033, 1998.

[74] P. Reimer *et al.* D. Geesaman. Fermilab proposal p906. `http://www.phy.anl.gov/mep/drell-yan/`, 1999.

[75] M. A. Doncheski, F. Halzen, C. S. Kim, and M. L. Stong. Hadronic W production and the Gottfried Sum Rule. *Phys. Rev.*, D49:3261–3269, 1994.

[76] J. C. Peng and D. M. Jansen. Probing $\bar{u}/\bar{d}$ asymmetry in the proton via W and Z production. *Phys. Lett.*, B354:460–464, 1995.

[77] Claude Bourrely and Jacques Soffer. Parton distributions from W+- and Z production in polarized p p and p n collisions at RHIC. *Nucl. Phys.*, B423:329–348, 1994.

[78] Bo-Qiang Ma. Sea quark content of nucleons: Flavor distribution asymmetry or isospin symmetry breaking? *Phys. Lett.*, B274:111–115, 1992.

[79] Bo-Qiang Ma, Andreas Schafer, and Walter Greiner. Flavor distributions in the nucleons: SU(2) sea asymmetry or isospin symmetry breaking? *Phys. Rev.*, D47:51–55, 1993.

[80] Eric Sather. Isospin violating quark distributions in the nucleon. *Phys. Lett.*, B274:433–438, 1992.

[81] A.W. Thomas E.N. Rodionov and J.T. Londergan. *Int. J. Mod. Phys. Lett.*, A9:1799, 1994.

[82] C. J. Benesh and J. Terrance Goldman. Charge symmetry breaking in the valence quark distributions of the nucleon. *Phys. Rev.*, C55:441–447, 1997.

[83] J. T. Londergan and Anthony William Thomas. The validity of charge symmetry for parton distributions. *Prog. Part. Nucl. Phys.*, 41:49–124, 1998.

[84] Fernanda Monti Steffens and Anthony William Thomas. On the interpretation of the NA51 experiment. *Phys. Lett.*, B389:217–220, 1996.

[85] W. Melnitchouk and Anthony William Thomas. Shadowing in deuterium. *Phys. Rev.*, D47:3783–3793, 1993.

[86] M. A. Braun and M. V. Tokarev. Deuteron and neutron structure functions and effect of relativistic Fermi motion. *Phys. Lett.*, B320:381–387, 1994.

[87] Mikolaj Sawicki and James P. Vary. Off-shell partons, Gottfried sum rule and dilepton suppression. *Phys. Rev. Lett.*, 71:1320–1323, 1993.

[88] Ivan Schmidt and Jian-Jun Yang. Nuclear effects on the extraction of neutron structure functions. *Eur. Phys. J.*, C20:63–70, 2001.

[89] V.D. Barger and R.J.N. Phillips. *Collider Physics*. Addison - Wesley Publishing Company, 1987.

[90] Alan D. Martin, W. James Stirling, and R. G. Roberts. Parton distributions updated. *Phys. Lett.*, B306:145–150, 1993.

[91] J. Pumplin et al. New generation of parton distributions with uncertainties from global QCD analysis. *JHEP*, 07:012, 2002.

[92] M. Gluck, P. Jimenez-Delgado, and E. Reya. Dynamical parton distributions of the nucleon and very small-x physics. *Eur. Phys. J.*, C53:355–366, 2008.

[93] A. D. Martin, W. J. Stirling, R. S. Thorne, and G. Watt. Parton distributions for the LHC. *Eur. Phys. J.*, C63:189–285, 2009.

[94] G. Bunce *et al.* Plans for the rhic spin physics program. `http://spin.riken.bnl.gov/rsc/report/spinplan_2008/spinplan08.pdf`, 2008.

[95] K. Adcox et al. PHENIX detector overview. *Nucl. Instrum. Meth.*, A499:469–479, 2003.

[96] CMS Collaboration. Physics technical design report volume i: Detector performance and software. CERN/LHCC 2006-001, 2006.